

## **Distribution Agreement**

In presenting this dissertation as a partial fulfillment of the requirements for an advanced degree from Emory University, I agree that the Library of the University shall make it available for inspection and circulation in accordance with its regulations governing materials of this type. I agree that permission to copy from, or to publish, this dissertation may be granted by the professor under whose direction it was written, or in his absence, by the Dean of the Graduate School when such copying or publication is solely for scholarly purposes and does not involve financial gain. It is understood, that any copying from, or publication of, this dissertation which involves potential financial gain will not be allowed without written permission.

Signature

---

Miao Wang

---

Date

**Entropic Origin for Catalysis of Cobalt-Carbon Bond  
Cleavage in Coenzyme B<sub>12</sub> (Adenosylcobalamin) in  
Ethanolamine Ammonia-Lyase**

By

Miao Wang  
Doctor of Philosophy  
Physics

Advisor: Dr. Kurt Warncke

Approved for the Department by:

---

Advisor

---

Dr. Boi Hanh (Vincent) Huynh  
Committee Member

---

Dr. Laura Finzi  
Committee Member

---

Dr. Ivan Rasnik  
Committee Member

---

Dr. Michael Heaven  
Committee Member

Accepted:

---

Lisa A. Tedesco, Ph.D. Dean of the Graduate School

---

Date

**Entropic Origin for Catalysis of Cobalt-Carbon Bond  
Cleavage in Coenzyme B<sub>12</sub> (Adenosylcobalamin) in  
Ethanolamine Ammonia-Lyase**

By

Miao Wang  
B.S., Tsinghua University, China 2001

Advisor  
Kurt Warncke, Ph.D.

An Abstract of a Dissertation Submitted to  
the Faculty of the Graduate School  
of Emory University in Partial Fulfillment  
of the Requirements for the Degree of  
Doctor of Philosophy  
in  
Physics  
2009

## Abstract

Entropic Origin for Catalysis of Cobalt-Carbon Bond Cleavage in Coenzyme B<sub>12</sub>

(Adenosylcobalamin) in Ethanolamine Ammonia-Lyase

By Miao Wang

The formation of the Co<sup>II</sup>-substrate radical pair catalytic intermediate in coenzyme B<sub>12</sub> (adenosylcobalamin)-dependent ethanolamine ammonia-lyase (EAL) from *Salmonella typhimurium* has been studied in a 41% (v:v) DMSO/water cryosolvent system in the temperature range of 230-250 K by using X-band electron paramagnetic resonance (EPR) spectroscopy. For the first time, a stable (>4 hr at 230 K) ternary complex of enzyme, coenzyme and substrate is formed in a coenzyme B<sub>12</sub>-dependent enzyme, which allows temperature-step initiation of the reaction to form the Co<sup>II</sup>-substrate radical pair, and monitoring by time-resolved, full-spectrum EPR spectroscopy. A three-state (intact AdoCbl, substrate bound initial state; Co<sup>II</sup>-5'-deoxyadenosyl radical pair intermediate state; Co<sup>II</sup>-substrate radical pair state), two-step mechanism is used to treat the Co<sup>II</sup>-substrate radical pair formation reaction kinetics and equilibria with explicit consideration of the intermediate radical pair state. By using this model, the absence of an EPR-detectable intermediate yields a limit of >3.3 kcal/mol for the free energy of the Co<sup>II</sup>-5'-deoxyadenosyl radical pair relative to the ternary complex. The free energy difference between the Co<sup>II</sup>-substrate radical pair state and the initial state is approximately 0 kcal/mol for 230-250 K, and has an extrapolated value of -2.6 kcal/mol at 298 K. The absence of a substrate hydrogen isotope effect on the rate of Co<sup>II</sup>-substrate radical pair formation indicates that the Co-C bond cleavage is rate determining at 230-250 K. This allows the first-time determination, by using Eyring analysis, of the Co-C

bond cleavage activation enthalpy and entropy in a coenzyme B<sub>12</sub>-dependent enzyme. The large, 16 kcal/mol decrease in the activation free energy for Co-C bond cleavage in EAL relative to solution is contributed almost entirely by a large, positive activation entropy. The activation parameters offer a quantitative description for the coupling between the Co-C bond cleavage and hydrogen transfer steps in EAL. The UV-visible spectroscopy is used to obtain optical spectrum from the ternary complex. The result indicates that the ground state destabilization (enthalpic strain) is not a significant catalysis contribution, and supports the findings from the EPR studies. These results provide a new paradigm for catalysis of Co-C bond cleavage in coenzyme B<sub>12</sub>-dependent enzymes.

**Entropic Origin for Catalysis of Cobalt-Carbon Bond  
Cleavage in Coenzyme B<sub>12</sub> (Adenosylcobalamin) in  
Ethanolamine Ammonia-Lyase**

By

Miao Wang  
B.S., Tsinghua University, China 2001

Advisor  
Kurt Warncke, Ph.D.

A Dissertation Submitted to  
the Faculty of the Graduate School  
of Emory University in Partial Fulfillment  
of the Requirements for the Degree of  
Doctor of Philosophy  
in  
Physics  
2009

## **Acknowledgments**

I am sincerely grateful to my Ph.D. advisor Dr. Kurt Warncke for his constant support, encouragement and guidance in my education and research. This work wouldn't be possible without his supervision. I would also like to thank Dr. Boi Hanh (Vincent) Huynh for furnishing helpful suggestions and advices on various occasions. I sincerely thank Dr. Laura Finzi, Dr. Ivan Rasnik, Dr. Michael Heaven for providing critical comments on my dissertation.

I am appreciative of the friendship from the faculty, staff, and fellow students in the Physics Department. They made my five and half year stay at Emory a cherishable memory. I especially thank my graduate-student colleague Wesley Robertson for sharing the excitement and frustration on the photolysis project.

I would like to take this opportunity to thank my family members, Dad Wensheng Wang, Mom Xiurong Jin and lovely Wife Chen Li. Their unselfish love and support provides the indispensable energy in striving to accomplish my Ph.D. degree. This dissertation is dedicated to them.

## Table of Contents

	<b>Page</b>
<b>Chapter One: Introduction</b>	<b>1</b>
1.1 Problem Statement	2
1.2 Literature Review	6
1.2.1 Cofactor B <sub>12</sub> Dependent Enzymes.....	6
1.2.2 Electron Paramagnetic Resonance.....	13
1.2.3 Photochemistry of coenzyme B <sub>12</sub> .....	22
1.3 Outline of Dissertation	25
<b>Chapter Two: Development of Low Temperature Cryosolvent System</b>	<b>28</b>
2.1 Survey of Cryosolvents	29
2.1.1 Cryoenzymology at Subzero Temperatures .....	29
2.1.2 VS41A and VS41A-G .....	32
2.1.3 41% DMSO/water .....	34
2.1.4 Concluding Remarks .....	36
2.2 Kinetic Arrest of Ternary Complex at 230 K	37
2.2.1 Physical Property of 41% DMSO/water .....	38
2.2.2 pH-balancing at Subzero Temperature .....	41
2.2.3 Procedure to Introduce Substrate at 230 K .....	43
2.2.4 Spectroscopic Evidence for Ternary Complex .....	45
2.2.5 Concluding Remarks .....	46
2.3 Substrate Radical Pair Formation at Subzero Temperatures	46
2.3.1 EPR Study for the Free Radical Formed at 242K .....	47

2.3.2 Characterization of the Substrate Radical Reaction to Form the Product Radical .....	50
2.3.3 Viscosity Dependence on EAL's Kinetics .....	52
2.3.4 Concluding Remarks .....	54
2.4 Instrument Preparation .....	54
2.4.1 Capillary Tube Packaging .....	55
2.4.2 Instrument Setup .....	56
2.4.3 Concluding Remarks .....	56
<b>Chapter Three: Kinetic and Thermodynamic Studies of Co<sup>II</sup>-substrate Radical Pair in Cryosolvent System</b> .....	<b>57</b>
3.1 Temperature Dependence of Substrate Radical Pair Formation .....	59
3.1.1 Time-resolved, Full Spectrum Continuous Wave Electron Paramagnetic Resonance .....	59
3.1.2 Time-dependence of Co <sup>II</sup> -substrate radical pair formation .....	60
3.1.3 Temperature-dependence of Co <sup>II</sup> -substrate Radical Pair Formation between 234 – 248 K .....	62
3.1.4 Attempted Detection of Paramagnetic Intermediate States .....	65
3.1.5 Concluding Remarks .....	66
3.2 Kinetic Evidence for the Formation of Ternary Complex .....	67
3.2.1 Substrate Concentration Variation Experiment .....	68
3.2.2 Concluding Remarks .....	71
3.3 Three-state, Two-step Reaction Model .....	71
3.3.1 Kinetic Model Setup .....	71

3.3.2 Temperature-dependence of the first-order rate and equilibrium constants .....	75
3.4 Retrieving Thermodynamic Parameters for Co <sup>II</sup> -substrate Radical Pair Formation	76
3.4.1 Equilibrium Perturbation Experiments .....	76
3.4.2 Relations among Experimental Observables and Microscopic Rate Constants .....	80
3.4.3 Thermodynamics of Co <sup>II</sup> -substrate Radical Pair Formation .....	82
3.4.4 Concluding Remarks .....	89
<b>Chapter Four: Activation Parameters of Cobalt-Carbon Bond Cleavage</b>	<b>90</b>
4.1 Synthesis of Deuterated Substrate	92
4.1.1 Synthesis Protocol .....	93
4.1.2 Product Analysis .....	93
4.2 Substrate Radical Formation with <sup>2</sup> H <sub>2</sub> -Substrate	98
4.2.1 EPR lineshape of Co <sup>II</sup> -substrate Radical Pair in Aqueous and Cryosolvent Systems with <sup>2</sup> H <sub>2</sub> -Substrate .....	98
4.2.2 Time-dependence of Co <sup>II</sup> -substrate radical Pair Formation with <sup>2</sup> H <sub>2</sub> -Substrate .....	100
4.2.3 Temperature-dependence of <i>k<sub>obs</sub></i> with <sup>2</sup> H-Substrate.....	101
4.2.4 Temperature-dependence of <i>v</i> with <sup>2</sup> H-Substrate .....	102
4.3 Revisiting the Three-step, Two-state Reaction Model	107
4.4 Retrieving Co-C Bond Cleavage Activation Parameters	110
4.5 Other Possible Reaction Scheme	114

4.6 Solvent Effect Study	121
4.7 Concluding Remarks	122
<b>Chapter Five: Optical Absorption Studies of the Ternary Complex</b>	<b>127</b>
5.1 Instrument Design and Setup	128
5.2 Temperature-dependence of Cofactor B <sub>12</sub> UV-visible Spectrum	130
5.3 Ternary Complex Preparation Protocol	133
5.4 UV-visible spectrum of the Ternary Complex and Holoenzyme	134
5.5 Concluding Remarks	140
<b>Chapter Six: Investigation of Photo-induced Co<sup>II</sup>-substrate Radical Pair Formation</b>	<b>141</b>
6.1 Instrument Setup	144
6.2 Photolysis of Cofactor B <sub>12</sub>	146
6.3 Photolysis of the Holoenzyme and Ternary Complex	147
6.4 Application of Spin Trap in Photolysis	150
6.5 Concluding Remarks	151
<b>Appendix: Manuals and Protocols</b>	<b>152</b>
A: Instruction for Oxford Cryostat System with Bruker E560 Console	153
B: Ternary Complex Preparation Procedure for EPR Studies	158
C: Synthesis of [1,1- <sup>2</sup> H <sub>2</sub> ]-aminopropanol	161
D: Ternary Complex Sample Preparation for UV-Visible Abs	163
E: Cary 100 Basic Operation Manual	165
F: List of Coded Programs	167
<b>Bibliography</b>	<b>168</b>

## List of Figures

### Chapter One: Introduction

Figure 1.1: Structure of coenzyme B <sub>12</sub> .....	7
Figure 1.2: Proposed minimum mechanism of EAL .....	11
Figure 1.3: Model for the active site geometry of reactant centers: Co <sup>II</sup> -substrate radical pair state of EAL .....	12
Figure 1.4: Structures of the <i>EutB</i> protein of EAL with six subunits .....	13
Figure 1.5: The activity of EAL as a function of <i>pH</i> .....	14
Figure 1.6: Energy diagram for electron Zeeman splitting in an external magnetic field .....	15
Figure 1.7: Shape of five <i>3d</i> wave functions .....	19
Figure 1.8: Energy level of cobalamin .....	20
Figure 1.9: Different stages for the substrate molecule in EAL catalytic cycle .....	21
Figure 1.10. The <i>xyz</i> coordinate system used to define the orientation of the magnetic field vector relative to the active site in EPR .....	22
Figure 1.11: UV-visible absorption spectrum for CNCbl and AdoCbl .....	24

### Chapter Two: Development of Low Temperature Cryosolvent System

Figure 2.1: The heat of ice crystallization ( <i>q</i> , unit in gram) as a function of sample cooling rate for different DMSO/water concentrations .....	31
Figure 2.2: EPR spectra of samples prepared in VS41A .....	33
Figure 2.3: EPR spectra of samples prepared in VS41A-G .....	34
Figure 2.4: EPR spectra of samples prepared in 41% DMSO/water .....	35
Figure 2.5: The 3D structure of DMSO .....	37
Figure 2.6: Temperature dependence of the density of DMSO/water cryosolvent .....	39
Figure 2.7: Temperature dependence of the viscosity of DMSO/water cryosolvent .....	40
Figure 2.8: Temperature dependence of the dielectric constant of DMSO/water cryosolvent ....	41

Figure 2.9: Temperature dependence of the $pH$ for 41% DMSO/water cryosolvent with different 5.3 mM buffer .....	43
Figure 2.10: Minimum sample preparation scheme .....	44
Figure 2.11: EPR spectrum of the cryotrapped $Co^{II}$ -substrate radical pair in 41% DMSO/water cryosolvent after equilibration at $T=242$ K .....	48
Figure 2.12: EPR line shape variation from changes on radical pair distance ( $\pm 1$ Å) .....	50
Figure 2.13. Time-dependence of the decay of the substrate radical EPR amplitude at 270 K in the cryosolvent system under conditions of approximately stoichiometric substrate:active sites ...	52
Figure 2.14: Time-dependence of the growth of the substrate radical EPR amplitude at 246 K in 41% and 50% DMSO/water cryosolvent systems .....	53

### **Chapter Three: Kinetic and Thermodynamic Studies of $Co^{II}$ -substrate Radical Pair in Cryosolvent System**

Figure 3.1: Time-dependence of the EPR spectrum of the substrate radical pair state in EAL in the cryosolvent system at $T=242$ K, following temperature-step initiation of reaction .....	61
Figure 3.2: Time-dependence of the EPR amplitude of the substrate radical pair state in EAL in the cryosolvent system at $T=242$ K, following temperature-step initiation of reaction .....	61
Figure 3.3. Dependence of the natural logarithm of the observed first-order rate constant for growth of the substrate radical EPR signal vs. $1/T$ from $T=234$ - $248$ K .....	64
Figure 3.4: Block-averaged EPR spectra of the substrate radical obtained during reaction at $T=242$ K .....	67
Figure 3.5. Dependence of the observed first-order rate constant for the growth of the substrate radical pair EPR signal, $k_{obs}$ , on the substrate:active sites ratio at $T=240$ and $246$ K in the cryosolvent system .....	69
Figure 3.6: Dependence of the normalized constant (long-time) amplitude of the substrate radical EPR signal on the substrate:active sites ratio at $T=240$ and $246$ K in the cryosolvent system	69

Figure 3.7: Normalized equilibrium saturation of the substrate radical EPR amplitude as a function of absolute temperature for three experiments .....	80
Figure 3.8. Van't Hoff plot of the equilibrium constant, $K_{13}$ , representing the equilibrium between the ternary complex (state $A_1$ ) and the $\text{Co}^{\text{II}}$ -substrate radical pair (state $A_3$ ), over the temperature range of 238-250 K .....	85
Figure 3.9: Schematic free energy diagram of the relative free energy levels of the ternary complex (state $A_1$ ), $\text{Co}^{\text{II}}$ -5'-deoxyadenosyl radical pair (state $A_2$ ), and $\text{Co}^{\text{II}}$ -substrate radical pair (state $A_3$ ) in EAL .....	88
<b>Chapter Four: Activation Parameters of Co-C Bond Cleavage</b>	
Figure 4.1: ESI spectrum for commercially obtained $[1,1\text{-}^1\text{H}_2]\text{-(S)-2-aminopropanol}$ and home-synthesized $[1,1\text{-}^2\text{H}_2]\text{-(S)-2-aminopropanol}$ .....	94
Figure 4.2: MS/MS spectrum for commercially obtained $[1,1\text{-}^1\text{H}_2]\text{-(S)-2-aminopropanol}$ and home-synthesized $[1,1\text{-}^2\text{H}_2]\text{-(S)-2-aminopropanol}$ .....	95
Figure 4.3: The chemical structure of $[1,1\text{-}^1\text{H}_2]\text{-(S)-2-aminopropanol}$ and $[1,1\text{-}^2\text{H}_2]\text{-(S)-2-aminopropanol}$ .....	97
Figure 4.4: Comparison of $^1\text{H}$ NMR spectra between $[1,1\text{-}^1\text{H}_2]\text{-(S)-2-aminopropanol}$ and $[1,1\text{-}^2\text{H}_2]\text{-(S)-2-aminopropanol}$ .....	97
Figure 4.5: X-band continuous-wave EPR spectra of cryotrapped holo-EAL and substrate $[1,1\text{-}^2\text{H}_2]\text{-(S)-2-aminopropanol}$ mixtures under different conditions of solvent and temperature .....	99
Figure 4.6: Time-dependence of the EPR spectrum of the $^2\text{H}$ -substrate radical pair state in EAL in the cryosolvent system at $T=242$ K, following temperature-step initiation of reaction .....	100
Figure 4.7: Time-dependence of the EPR amplitude of the $^2\text{H}$ -substrate radical pair state in EAL in the cryosolvent system at $T=242$ K, following temperature-jump initiation of reaction .....	101
Figure 4.8: Dependence of the natural logarithm of the observed first-order rate constant for growth of the $^2\text{H}$ -substrate radical EPR signal on the inverse absolute temperature from $T=234\text{-}246$ K .....	102

Figure 4.9: Normalized equilibrium saturation of the substrate radical EPR amplitude as a function of absolute temperature for two runs with different samples .....	104
Figure 4.10: Van't Hoff plot of the equilibrium constant, $K_{I3}$ , representing the equilibrium between the ternary complex (state $A_1$ ) and the $\text{Co}^{\text{II}}$ -substrate radical pair (state $A_3$ ), over the temperature range of 238-246 K from the data shown in Figure 4.9 .....	106
Figure 4.11: Eyring plot of the calculated Co-C bond cleavage rate constant .....	111
Figure 4.12: Schematic free energy diagram of the reaction curve of the ternary complex (state $A_1$ ), $\text{Co}^{\text{II}}$ -5'-deoxyadenosyl radical pair (state $A_2$ ), and $\text{Co}^{\text{II}}$ -substrate radical pair (state $A_3$ ) in EAL.....	114
Figure 4.13: UV-visible absorption spectrum for the solvent effect studies with methyl-p-benzoquinone .....	121
Figure 4.14: Schematic diagram of the enthalpic and entropic contribution to the Co-C bond cleavage in aqueous solution and in EAL at $T=298$ K .....	126

### **Chapter Five: Optical Absorption Studies of Ternary Complex**

Figure 5.1: UV-visible Abs spectrum of AdoCbl in 41% DMSO/water cryosolvent at different temperatures .....	131
Figure 5.2: Temperature dependence of the $\alpha/\beta$ band peak of AdoCbl from ambient temperature to 231 K .....	132
Figure 5.3: UV-visible Abs spectra comparison between ternary complex, holoenzyme and free AdoCbl .....	135
Figure 5.4: Bar plot for the $\alpha/\beta$ band peak position for the UV-visible Abs spectrum on ternary complex, holoenzyme and AdoCbl at 230 K .....	136

### **Chapter Six: Probe Photo Chemistry in Enzyme Activity**

Figure 6.1: EPR spectra following photolysis of AdoCbl in 41% DMSO/water cryosolvent...	147
Figure 6.2: EPR spectra following photolysis of holoenzyme and ternary complex at 230 K .	149

Figure 6.3: Chemical structure of DMPO .....151

## List of Tables

### Chapter One: Introduction

Table 1.1: Kinetic Constants for the substrates of EAL from <i>S. typhimurium</i> .....	9
---	---

### Chapter Two: Development of Low Temperature Cryosolvent System

Table 2.1: DMSO/water (v:v) ratio vs. freezing temperature in <i>K</i> .....	31
--	----

Table 2.2: EPR simulation parameters for the $\text{Co}^{\text{II}}$ -substrate radical pair formed in low temperature 41% DMSO/water cryosolvent at 242 K and in aqueous solution at 295 K .....	48
---	----

### Chapter Three: Kinetic and Thermodynamic Studies of $\text{Co}^{\text{II}}$ -substrate Radical Pair in Cryosolvent System

Table 3.1: Values of the observed rate constant for $\text{Co}^{\text{II}}$ -substrate radical pair formation at different absolute temperatures .....	64
--	----

Table 3.2: Calculated values of the normalized enzyme-substrate complex concentration at different substrate:active site ratios, for three $K_D$ values .....	70
---	----

Table 3.3: Values of experimentally determined thermodynamic parameters for the $A_1$ (ternary complex) – $A_3$ ( $\text{Co}^{\text{II}}$ -substrate radical pair) equilibrium in the cryosolvent system, and estimated EAL protein-associated contributions .....	87
--	----

### Chapter Four: Activation Parameters of Co-C Bond Cleavage

Table 4.1: Values of the observed rate constant for $\text{Co}^{\text{II}}$ -substrate radical pair formation at different absolute temperatures for $^1\text{H}$ -substrate ( $k_{obs}^H$ ) and $^2\text{H}$ -substrate ( $k_{obs}^D$ ) .....	102
--	-----

Table 4.2: Values of experimentally determined population ratio for the equilibrated $A_3$ (ternary complex) and the initial $A_1$ ( $\text{Co}^{\text{II}}$ -substrate radical pair) in the cryosolvent system .....	105
---	-----

Table 4.3: Values of experimentally determined thermodynamic parameters for the $A_1$ (ternary complex) – $A_3$ ( $\text{Co}^{\text{II}}$ -substrate radical pair) equilibrium in the cryosolvent system .....	107
--	-----

### Chapter Five: Optical Absorption Studies of Ternary Complex

Table 5.1: Values of $\alpha/\beta$ band peak position for AdoCbl Abs spectrum at different absolute temperatures .....	131
Table 5.2: Values of $\alpha/\beta$ band peak position for the UV-visible Abs spectrum on ternary complex, holoenzyme and AdoCbl at 230 K .....	136

# **Chapter One**

## **Introduction**

## 1.1 Problem Statement

Coenzyme B<sub>12</sub>-dependent enzymes are highlighted by their unique ability to accelerate the cleavage of the cobalt-carbon (Co-C) bond by  $>10^{11}$  fold<sup>1-3</sup>. The homolytic bond dissociation energy of the carbon-cobalt bond is reduced to below 15 kcal/mol from 30 kcal/mol by the enzyme under physiological conditions<sup>4,5</sup>. In the proposed mechanism, the catalytic cycle begins with Co-C bond cleavage after substrate binding, which directly leads to the formation of the Co<sup>II</sup>-5'-deoxyadenosyl radical pair<sup>6</sup>. In the subsequent radical pair separation, the C5'-methylene radical center migrates from the  $\beta$ -face of cobalamin to the substrate binding site, where it abstracts a hydrogen atom (the hydrogen transfer step, HT1) from the substrate to form the Co<sup>II</sup>-substrate radical pair. A more detailed description of the minimum mechanism is presented in the Literature Review.

The most central mechanistic question, which has received extensive debates over the past five decades<sup>4-7</sup>, is how the enzymes achieve this extraordinary rate enhancement. Several hypothesis, including destabilization of the Co-C bond through (1) *trans*-axial ligand (5,6-dimethylbenzimidazole) effect<sup>8-10</sup>, (2) *cis*-axial ligand (5'-deoxyadenosyl) effects<sup>9</sup>, (3) corrin ring flexure<sup>1,11,12</sup>, and (4) stabilization of the intermediate states after homolysis<sup>13</sup> have been proposed.

Intuitively, the best ways to test these hypotheses would be to measure the Co-C bond cleavage rate, and retrieve thermodynamic parameters for the enzyme, and compare their values for free AdoCbl in aqueous solution. To achieve this goal, a few transient experiments have been performed on the coenzyme B<sub>12</sub>-dependent enzyme superfamily members, methylmalonyl-CoA mutase (MCM)<sup>14</sup>, glutamate mutase<sup>15</sup>, ribonucleotide

triphosphate reductase (RTPR)<sup>16</sup>, and ethanolamine ammonia-lyase (EAL)<sup>17,18</sup> to obtain the kinetics related to the Co-C bond cleavage step. These experiments employed visible absorption change from adenosylcob(III)alamin ( $\lambda_{\max}=525$  nm) to cob(II)alamin ( $\lambda_{\max}=470$  nm), coupled with stopped-flow method, to monitor the accumulation rate for Co<sup>II</sup> state ( $k_{obs}$ ). However, due to the limitation of optical detection in distinguishing different intermediate Co<sup>II</sup> states in the catalytic process, it is ambiguous to relate this experimental observable to the microscopic Co-C bond cleavage rate in the enzyme catalytic cycle.

To unravel the Co-C bond cleavage rate from  $k_{obs}$ , the hydrogen isotope (both transient and steady-state) effects have been measured by the same optical method.<sup>15,18,19</sup> The hydrogen isotope effects were all greater than unity at ambient temperature, but far less than the intrinsic hydrogen transfer isotope effect. This result qualitatively unveiled the coupling between the Co-C bond cleavage and the hydrogen atom transfer step (HT1), but made the quantitative interpretation of Co-C bond cleavage rate from  $k_{obs}$  a challenge.

Another huge obstacle in resolving the Co-C bond cleavage rate from the experimental observable is placed by the mysterious 5'-deoxyadenosyl radical. Despite more than four decades of active research, no one has successfully trapped this intermediate state, owing to its high free energy<sup>20,21</sup>. Surrendering to these difficulties, a couple of research groups<sup>14,22</sup> proposed the concerted reaction mechanism for the mutase class of coenzyme B<sub>12</sub>-dependent enzymes. In their mechanism, the Co-C bond cleavage and HT1 step are treated to share the same transition state (i.e. removing the 5'-dexoymadenosyl radical intermediate state), to calculate the Co-C bond cleavage rate. The accuracy of the thermodynamic parameters obtained from such a model, and the general

application to all coenzyme B<sub>12</sub>-dependent enzymes, are questionable, because the following experimental facts suggest that a discrete 5'-deoxyadenosyl radical exists: (1) the observed substrate hydrogen isotope effect at ambient temperature is less than the intrinsic the large separation (8-11 Å) distance<sup>16,23,24</sup> between cobalt and radical centers in the first meta-stable radical pair state in the eliminase class of coenzyme B<sub>12</sub>-dependent enzymes; (2) the small value (<10<sup>-3</sup> kcal/mol)<sup>25</sup> of the electronic interaction (electron spin-spin coupling constant, J) between Co<sup>II</sup> and substrate radicals in the eliminase enzymes.

To overcome the disadvantages in previous kinetic studies and better answer the mechanism for Co-C bond cleavage in the coenzyme B<sub>12</sub>-dependent enzymes, we have developed a cryoenzymology technique<sup>26</sup> to study the radical pair formation reactions in ethanolamine ammonia-lyase (EAL; EC 4.3.1.7; see Literature Review) from *Salmonella typhimurium*<sup>4-6</sup> at low temperatures (234 K to 248 K) with time-resolved, full-spectrum electron paramagnetic resonance (EPR; see Literature Review) spectroscopy. The results indicate a dominant entropy contribution to the catalysis of Co-C bond cleavage, instead of the previously proposed enthalpy dominant contribution to the reduction of the Co-C activation energy.

Many efforts, including FT-Raman<sup>27</sup>, Resonance Raman<sup>28</sup>, Magnetic Circular Dichroism<sup>29</sup> and X-ray crystallography<sup>30</sup>, which were targeted on either the cofactor derivative or the cofactor inside holoenzyme, or holoenzyme with substrate analogs, have been performed over the past decades. To our best knowledge, these experiments were carried out without functional substrate, because of the fast turn-over rate at ambient

temperature. Therefore, the results obtained in these experiments maybe inspiring but not convincing.

During the course of our cryoenzymology studies, we realized the lifetime for the EAL·AdoCbl-substrate ternary complex to as long as  $>6.0 \times 10^3 \text{ s} = 1.0 \times 10^2 \text{ min}^{26}$  at 230 K. This lifetime is sufficiently long to allow direct spectroscopy studies. The UV-visible absorption technique was chosen, and subtle shifts in the UV/visible absorbance spectra were observed upon AdoCbl bounding to EAL, and upon binding of substrate to holoenzyme to form the ternary complex, over 233-300 K. This indicates that the protein does not affect Co-C bond cleavage catalysis through direct energetic contributions to AdoCbl destabilization.

The third type of kinetic experiment that was used to investigate the Co-C bond cleavage process was the photolysis method,<sup>13,31-33</sup> which has been employed as a substitute for the Co-C bond thermal homolysis in free solution as well as in holoenzyme without substrate or with substrate analog. The kinetically arrested EAL·AdoCbl-substrate ternary complex at cryotemperature allowed the photo-induced enzyme activity study to be performed, for the first time, with functional substrate bounded coenzyme B<sub>12</sub>-dependent enzymes. These results do not only enhance our knowledge on B<sub>12</sub> photolysis but also provides insights into the EAL catalytic mechanism.

In summary, we investigated the course of Co-C bond cleavage with the presence of EAL by using 41% (v:v) DMSO/water crysolvent system. Multiple experimental approaches, including time-resolved EPR, substrate hydrogen isotope effect, UV-visible spectroscopy and photolysis techniques, were adopted. All the results consistently pointed to a dominant entropic contribution to catalysis of the Co-C bond cleavage in

EAL. This conclusion is very counterintuitive to the previously proposed enthalpic contributions and establishes a new paradigm for the catalysis effect in the cofactor B<sub>12</sub> dependent enzyme superfamily. It also broadens our general knowledge in enzyme catalysis from structural (enthalpic) interactions to solvent coupled protein conformational (entropic) changes.

## 1.2 Literature Review

### 1.2.1 Cofactor B<sub>12</sub> Dependent Enzymes

Vitamin B<sub>12</sub> (Figure 1.1) is the only known biomolecule with a stable carbon-metal bond.<sup>1,6</sup> Extensive researches into its structure and biological functions has led to four Nobel prizes, three in chemistry and one in medicine.<sup>1,6</sup> The core of the molecule is a corrin ring with various attached side-groups. The ring comprises four pyrrole subunits, each of which is joined on opposite sides by a C-CH<sub>3</sub> methylene link, except for one link, in which the two of the pyrroles joined directly. The axial nitrogen of each pyrrole is coordinated to the central cobalt atom. The ligand below the ring is a nitrogen of a 5,6-dimethylbenzimidazole. The other nitrogen is linked to a five-carbon sugar, which in turn connects to a phosphate group that links back onto the corrin ring via one of the amide groups attached to the periphery of the corrin ring.

The importance of the coenzyme B<sub>12</sub> molecule in biology is that it serves as the cofactor in the coenzyme B<sub>12</sub>-dependent enzyme superfamily, which is divided into two major categories, the mutases and eliminases.

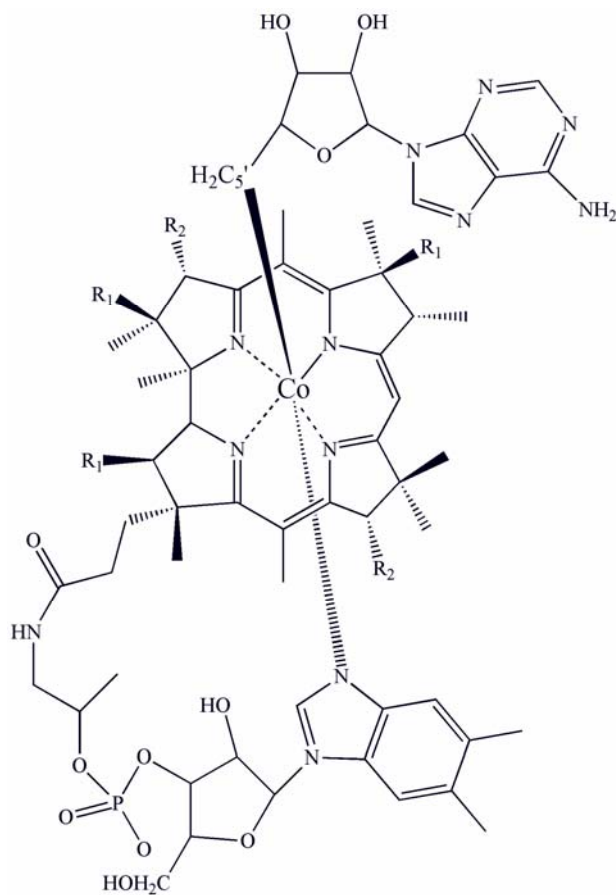


Figure 1.1: Structure of coenzyme B<sub>12</sub>.<sup>1</sup>

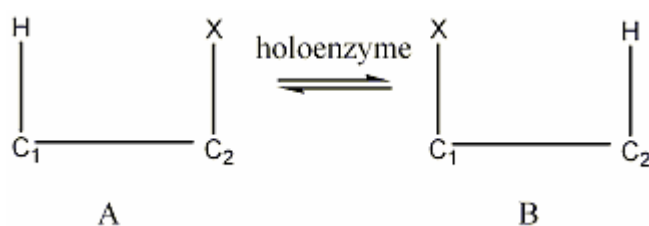
The mutases category can be further divided into the following two classes of enzymes: Class I coenzyme B<sub>12</sub>-dependent enzymes, which catalyze the carbon skeleton rearrangement reaction and Class III coenzyme B<sub>12</sub>-dependent enzymes, which catalyze the amino migration reaction. The Class I enzymes includes glutamate mutase<sup>34</sup>, isobutyryl-CoA mutase<sup>35</sup>, 2-methylene-glutarate mutase<sup>36</sup> and methyl-malonyl-CoA mutase<sup>37</sup>. The Class III enzymes includes lysine 2,3-aminomutase<sup>38</sup> and ornithine 4,5-aminomutase<sup>39</sup>.

The eliminases (Class II) utilize either hydroxyl or amino as the migrating group, but they differ from the Class III mutases by eliminating a water or ammonia molecule in

the observed product. These Class II enzymes include ethanolamine ammonia lyase<sup>40</sup>, glycerol dehydratase<sup>41</sup>, propane-1,2-diol dehydratase<sup>42</sup> and ribonucleotide reductase<sup>43</sup>. The ribonucleotide reductase distinguishes itself in the Class II enzymes by catalyzing a redox process that is associated with a functional group rearrangement.

The whole coenzyme B<sub>12</sub>-dependent enzyme superfamily is considered as a distinctive class of enzymes because they function via highly reactive free radicals, which is often an unpaired electron. These free radicals endow the cofactor B<sub>12</sub>-dependent enzymes a unique property from the most common enzyme functionality, which is enhancing the reaction rate, as guiding the “hot” intermediate radicals within native pathway to prevent side reactions. The existence of these free radicals also made the coenzyme B<sub>12</sub>-dependent enzyme superfamily a perfect target for EPR study.

In this dissertation, we focus on one member from the class II coenzyme B<sub>12</sub>-dependent enzymes: ethanolamine ammonia lyase (EAL, formerly known as ethanolamine deaminase<sup>44</sup>), which converts ethanolamine to acetaldehyde and ammonia. This process is fundamentally an isomerization process, with the amino group migrating from its original position (C<sub>2</sub>) to the adjacent carbon (C<sub>1</sub>) in exchange for a hydrogen atom, which migrates in the opposite direction, as shown in Scheme 1.1.



Scheme 1.1: Simplest scheme of EAL enzyme catalysis. X represents the amino group.

EAL was discovered to act on other types of substrate, as follows: (1) (S)-2-aminopropanol<sup>45,46</sup>, (2) (R)-2-aminopropanol<sup>47</sup>. EAL also converts 1-amino-2-propanol to acetone and ammonia<sup>48</sup>, but at an exceptionally slow rate and the enzyme lost activity after a few turnovers. Therefore, it is not considered as a free substrate. Table 1.1 summarizes the kinetic parameters with different substrates for EAL from *Salmonella typhimurium*.

Table 1.1: Kinetic Constants for the substrates of EAL from *S. typhimurium*.<sup>49,50</sup>

Substrate	$K_m$ ( $\mu\text{M}$ )	$k_{cat}$ ( $\text{s}^{-1}$ )
Ethanolamine	$13.6 \pm 2.9$	$52.2 \pm 3.7$
(S)-2-aminopropanol	$0.80 \pm 0.06$	$0.12 \pm 0.01$
(R)-2-aminopropanol	$9 \pm 2$	$0.067 \pm 0.001$

The minimum mechanism<sup>51-53</sup> of EAL is shown in Figure 1.2. A full cycle proceeds through the following 6 steps: (1) With the presence of coenzyme B<sub>12</sub> in the B<sub>12</sub> binding pocket of EAL (holoenzyme complex), the substrate molecule binds to the substrate binding site to form the ternary complex. (2) The Co-C bond of B<sub>12</sub> breaks homolytically to generate a 5'-deoxyadenosyl radical on the  $\beta$  face of the corrin ring and the cobalt in the corrin ring is reduced from Co<sup>III</sup> to Co<sup>II</sup> state. (3): The 5'-deoxyadenosyl radical migrates to the substrate binding site and a hydrogen atom is abstracted (HT1) from the substrate by the 5'-deoxyadenosyl radical, forming a substrate radical (S•) and a 5'-deoxyadenosine. (4): The radical rearranges to form a product radical (R•). (5) A hydrogen atom transfers (HT2) from the 5'-methyl moiety of 5'-deoxyadenosine, which leads to the formation of the 5'-deoxyadenosyl radical the second time. (6) The produce is

released and the 5'-deoxyadenosyl radical recombines with cobalt and oxidizes it from  $\text{Co}^{\text{II}}$  to  $\text{Co}^{\text{III}}$ , which returns the enzyme to the original condition so that the enzyme can pick up another substrate molecule for the next catalytic cycle.

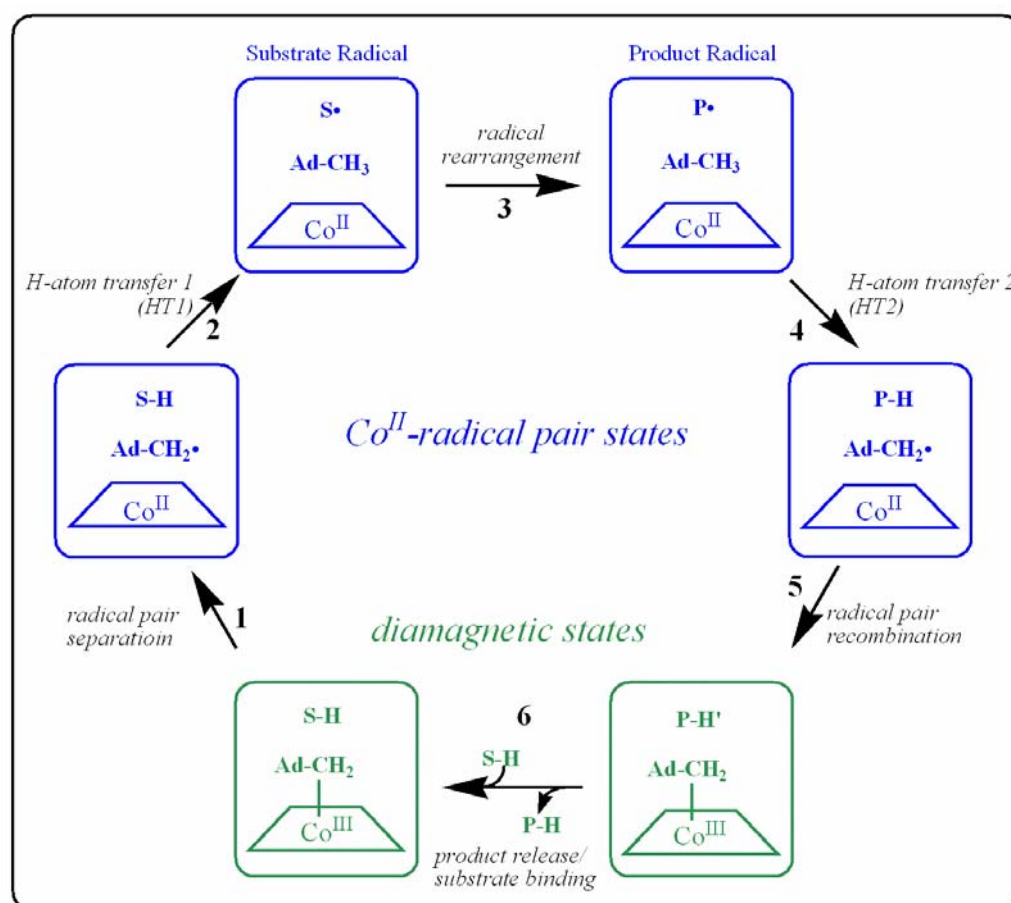


Figure 1.2: Proposed minimum mechanism of EAL. In the figure, substrate-derived species are designated S-H (bound substrate, **1**), S• (substrate radical, **2**), P• (product radical, **3**), and PH (diamagnetic products, aldehyde **4** and ammonia). The 5'-deoxyadenosyl  $\beta$ -axial ligand is represented as Ad-CH<sub>2</sub>- in the intact coenzyme, and as Ad-CH<sub>2</sub>• (5'-deoxyadenosyl radical) or Ad-CH<sub>3</sub> (5'-deoxyadenosine) following cobalt-carbon bond cleavage. The cobalt ion and its formal oxidation states are depicted, but the corrin ring and dimethylbenzimidazole  $\alpha$ -axial ligand of the coenzyme<sup>54</sup>, are not shown, for clarity.

The EAL enzyme used in the dissertation is purified from the *Escherichia coli* overexpression strain incorporating the cloned *Salmonella typhimurium* EAL coding

sequences essentially as described by Babior's group<sup>55</sup>. The apo-enzyme obtained from this method is composed of a 453-residue, 49.4 kDa EutB protein subunit and a 286-residue, 32.1 kDa EutC protein subunit, which are coded by the *eutb* and *eutc* genes, respectively<sup>56</sup>. EutB is the subunit which hosts the binding site for the substrate and cofactor. The EAL molecular contains two subunits are present in a EutB<sub>6</sub>EutC<sub>6</sub> structure with a molecular mass around 500 kDa<sup>55</sup>. Though the structures of several coenzyme B<sub>12</sub>-dependent enzymes in cofactor-bound, diamagnetic states have been solved by X-ray crystallography<sup>30,54,57,58</sup>, the structure of complete EAL from *Salmonella typhimurium* remains unsolved. However, electron paramagnetic resonance (EPR) spectroscopy supplies us with high-resolution (0.1-1.0 Å) structures of the reactant center geometries<sup>25,59</sup> in the paramagnetic, Co<sup>II</sup>-radical pair catalytic intermediate states in EAL (Figure 1.3). The 3D structure of EutB from *Salmonella typhimurium* has been proposed by comparative modeling method.<sup>60</sup> Recently the X-ray crystallographic structure of EutB from *Listeria monocytogenes* (Figure 1.4) was reported.<sup>61</sup> These results lead to better understanding of the protein's structure, and provide insight into the enzyme's function.

The most eye-catching character of EutB is the TIM barrel, which comprises a  $\alpha_8\beta_8$  secondary structure. This sturdy structure endows the EAL protein with a broad pH optimum, with essentially constant activity between pH 6.6 and 8.2 (Figure 1.5).<sup>40</sup> This robust  $\alpha_8\beta_8$ -Tim barrel structure ensures the EAL's activity at subzero temperatures in the cryosolvent for our EPR study.

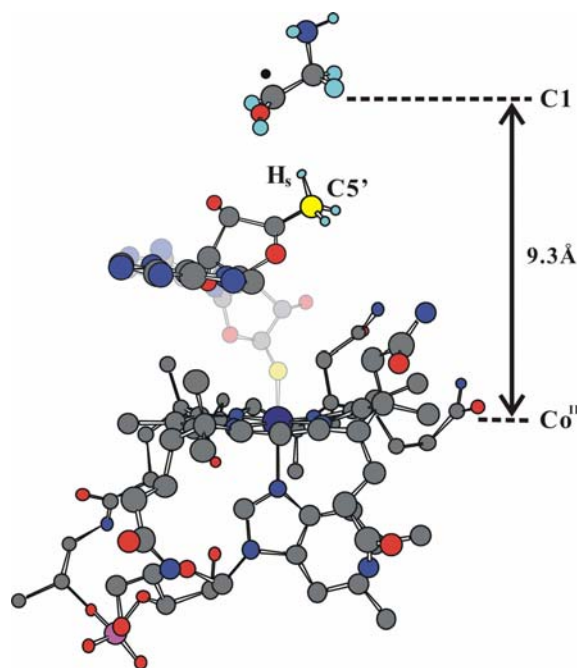


Figure 1.3: Model for the active site geometry of reactant centers: Co<sup>II</sup>-substrate radical pair state of ethanolamine ammonia-lyase.

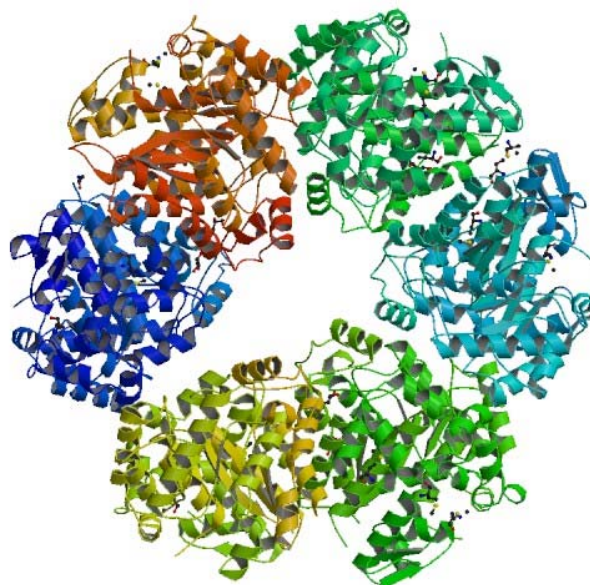


Figure 1.4: Structures of the EutB protein of ethanolamine ammonia-lyase with six subunits.<sup>61</sup>

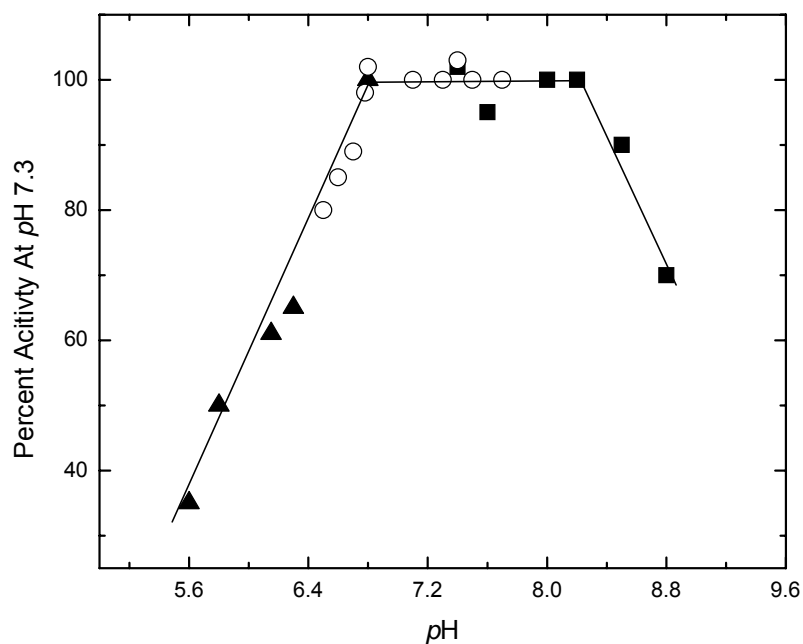


Figure 1.5: The activity of EAL as a function of  $pH$ . The solid triangle represents data in Citrate buffer, the open circle represents Phosphate buffer and the solid square represents Tris buffer.<sup>6</sup>

### 1.2.2 Electron Paramagnetic Resonance

Electron paramagnetic resonance (EPR), also known as electron spin resonance (ESR) or electron magnetic resonance (EMR), is the process of resonant absorption of microwave radiation by paramagnetic ions or molecules with at least one unpaired electron spin and in the presence of a static magnetic field.<sup>62,63</sup> It has become an essential experimental technique in a wide range of research fields, such as chemistry, physics, biology, and medicine.<sup>64</sup> Major milestones of EPR are listed below:

- 1921: Stern and Gerlach - electron magnetic moment quantized
- 1925: Uhlenbeck and Goudsmidt - linked electron magnetic moment with spin of electron

- 1931: Breit and Rabi described energy level for H• atom, linking nuclear and electron spin angular momentum
- 1938: Rabi, Zacharias, Millman, Kusch studied transitions between levels induced by an oscillation magnetic field
- 1945: Zavoisky observed first EPR absorption peak on CuCl<sub>2</sub>·2H<sub>2</sub>O
- 1956: ENDOR spectra measured by Feher
- 1972: Pulsed EPR designed by Mims

In EPR, the spin-flip transitions of unpaired electrons in an applied magnetic field are detected, which makes this technique ideal for detecting and characterizing free radicals. However, EPR is not limited to radical static geometry determination. It also has been widely used in kinetics studies.

The simplest way to explain the origin of the EPR signal is from a free electron with half spin. Electron possesses a magnetic moment and spin quantum number  $S = 1/2$ . In the presence of an external magnetic field, the orientation of the electron's magnetic moment is quantized to be either parallel ( $m_s = -1/2$ ) or antiparallel ( $m_s = +1/2$ ) to the direction of the field. Its Hamiltonian could be expressed as:

$$H = g\mu_B \vec{B} \cdot \vec{S} = g\mu_B B_0 m_s \quad (1.1)$$

where  $g$  is the electron's so-called  $g$ -factor and  $\mu_B$  is the Bohr magneton.

Therefore, the energy degeneracy between the two electron states is lifted under the external field and this state splitting is called Zeeman effect. The parallel alignment corresponds to a lower energy state, and the separation between the two states is:

$$\Delta E = g\mu_B B_0 \quad (1.2)$$

Eq. 1.2 shows that the splitting of the energy levels is directly proportional to the magnetic field's strength  $B_0$ , as depicted in the diagram (Figure 1.6) below.

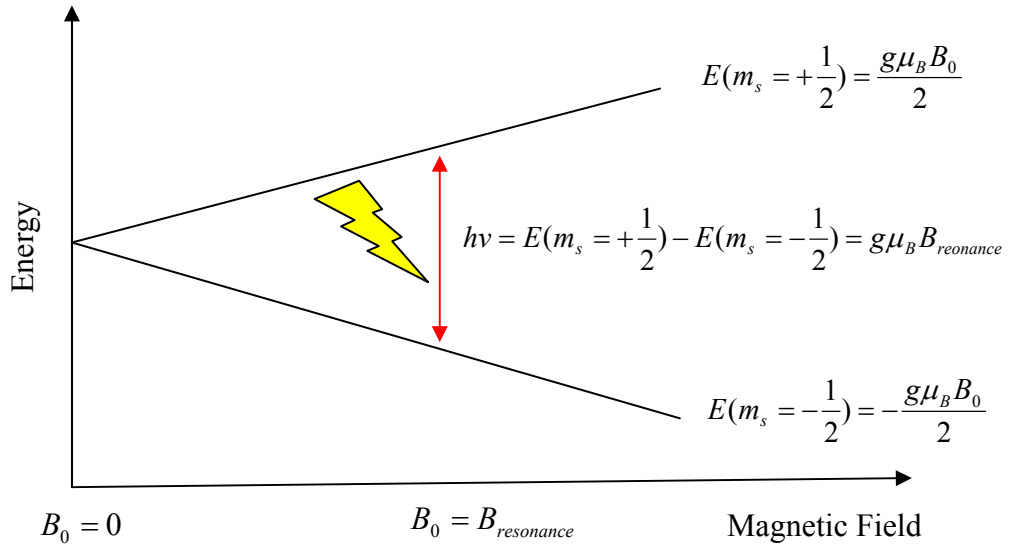


Figure 1.6: Energy diagram for electron Zeeman splitting in an external magnetic field.

If the population of radicals reaches thermodynamic equilibrium, its statistical distribution is described by the Maxwell-Boltzmann equation as:

$$\frac{N^{upper}}{N^{lower}} = \exp\left(-\frac{\Delta E}{RT}\right) = \exp\left(-\frac{g\mu_B B_0}{RT}\right) \quad (1.3)$$

Eq. 1.3 clearly demonstrates that the electron state in the lower energy level has more population than the higher energy state under equilibrium in Zeeman splitting.

If electromagnetic radiation of energy  $\varepsilon = h\nu$  is introduced at certain time  $t$  under Zeeman splitting equilibrium and its energy matches the resonance condition as follows:

$$\varepsilon = \Delta E \quad (1.4)$$

An electron could be excited from the lower energy state to the higher energy state after the absorption of the radiation. Substituting the radiation energy in Equation 1.4 leads to the fundamental equation of EPR spectroscopy:

$$h\nu = g\mu_B B_o \quad (1.5)$$

In principle, Eq. 1.5 permits a large set of frequency and magnetic field values, but the great majority of EPR measurements are made with microwaves in the 8200 – 12400 MHz (8.2 – 12.4 GHz) region, which is known as X-band.

In the EPR experiment, the radiation frequency is fixed and the magnetic field is varied to achieve resonance. From Eq. 1.2, the energy gap between the  $m_s = +1/2$  and  $m_s = -1/2$  energy states is proportional to  $B_o$ . At resonance, the unpaired electrons can be excited to another spin state. Since more electrons occupies the lower state as shown in Eq. 1.3, there will be a net absorption of energy, which is monitored as a function of magnetic field to generate the EPR spectrum.

The EPR technique was first invented by Zavoisky in 1945 and is called continuous wave-EPR (cw-EPR) because of the continuous microwave irradiation of the sample. This technique still remains as a widely-used technique in detecting the paramagnetic centers, though several improvements have been accomplished over the past six decades. For example, in modern cw-EPR instruments, to minimize the background noise such as the microwave diode current noise, a magnetic field modulation scheme with phase sensitive detection is employed. As a result, the detected signal appears as a first-order derivative. The instrument limitation on the modulation frequency is usual within 12.5 kHz and 100 kHz. The amplitude applied in the modulation can be set up to 40 G. The optimized modulation frequency and amplitude is

carefully chosen in individual experiments to maximize the EPR signal amplitude without distortion of the signal.

So far, we have only shown a single absorption line, which corresponds to the isotropic g-factor situation. In EPR, the g-factor line can only tell us limited information, such as the system spin state, without any molecular structure information. Fortunately, the eigen energy of the unpaired electron is affected by the chemical surroundings, especially by its nearby nuclei under the condition that the nuclei possesses a magnetic moment. This is because the magnetic moment from the nuclei produces a magnetic field at the electron, which adds vectorially to the external field in Eq. 1.2. This interaction between the electron and the nuclei is called the hyperfine interaction. The Hamiltonian with the hyperfine interaction is written as:

$$H = g\mu_B B_0 m_s + \vec{S} \cdot \tilde{A} \cdot \vec{I} \quad (1.6)$$

where the  $\vec{S}$  and  $\vec{I}$  are the electron and nuclear spin operators, respectively,  $B_0$  is the applied magnetic field, and  $\tilde{A}$  is the hyperfine tensor.

The paramagnetic states in our study are the Co<sup>II</sup>-5'-deoxyadenosyl radical pair, Co<sup>II</sup>- substrate radical pair and Co<sup>II</sup>-product radical pair. We will show that the Hamiltonians of these radicals are more complicated than the simple systems explored above, owing to the electron-electron interaction.

As shown in Figure 1.1, cobalt in the Co<sup>III</sup> oxidation state is generally coordinated to six ligands: the four equatorial nitrogens from the corrin ring, one carbon from the upper  $\beta$ -axial ligand and one nitrogen from the lower  $\alpha$ -axial ligand.

The redox property of cobalt is determined by the outer  $3d$  electron. The hydrogen-like wave functions of a free ion are eigen functions of the Hamiltonian operator:

$$H_0 = -\frac{\hbar^2}{2m} \nabla^2 - \frac{Z_{\text{eff}} e^2}{4\pi\epsilon_0 r} \quad (1.7)$$

Referred to a set of spherical polar coordinates, the wave functions are given by:

$$\psi_{nlm} = R_{nl} Y_l^m \quad (1.8)$$

where  $R_{nl}$  is the radial and  $Y_l^m$  the angular component of the wave function. It is convenient to express them in alternative forms that are explicit expressions of the Cartesian coordinates. In these alternative forms, the wave functions for the orbitals do not contain  $e^{im\phi}$  and consequently may be said to be the real orbitals. The real orbitals are simple linear combinations of the wavefunctions above from the spherical coordinate solutions of the Schrödinger equation.

For  $d$  electrons, the solution is  $R_{n2} Y_2^m$ . If we use  $(m)$  as an abbreviation for  $Y_2^m$ , we can write out (2) and (-2) explicitly as:

$$(2) = R_{n2} \left(\frac{15}{16}\right)^{\frac{1}{2}} (2\pi)^{-\frac{1}{2}} \sin^2 \theta (\cos 2\phi + i \sin 2\phi) \quad (1.9)$$

$$(-2) = R_{n2} \left(\frac{15}{16}\right)^{\frac{1}{2}} (2\pi)^{-\frac{1}{2}} \sin^2 \theta (\cos 2\phi - i \sin 2\phi) \quad (1.10)$$

So, the summation of (2) + (-2) is:

$$\begin{aligned} (2) + (-2) &= 2R_{n2} \left(\frac{15}{16}\right)^{\frac{1}{2}} (2\pi)^{-\frac{1}{2}} \sin^2 \theta (\cos^2 \phi - \sin^2 \phi) \\ &= R_{n2} \left(\frac{15}{16}\right)^{\frac{1}{2}} (2\pi)^{-\frac{1}{2}} \frac{x^2 - y^2}{r^2} \propto x^2 - y^2 \end{aligned} \quad (1.11)$$

Through this combination, we define a new orbital as:

$$d_{x^2-y^2} = 2^{-\frac{1}{2}}[(2) + (-2)] \quad (1.12)$$

Following this definition, the other four  $d$  wave functions in their real forms are obtained as:

$$d_{z^2} = (0) \quad (1.13)$$

$$d_{yz} = -i2^{-\frac{1}{2}}[(1) + (-1)] \quad (1.14)$$

$$d_{xz} = 2^{-\frac{1}{2}}[(1) - (-1)] \quad (1.15)$$

$$d_{xy} = -i2^{-\frac{1}{2}}[(2) - (-2)] \quad (1.16)$$

Figure 1.7 depicts the electron phase density distribution for  $3d$  electrons with combination of the radius functions.

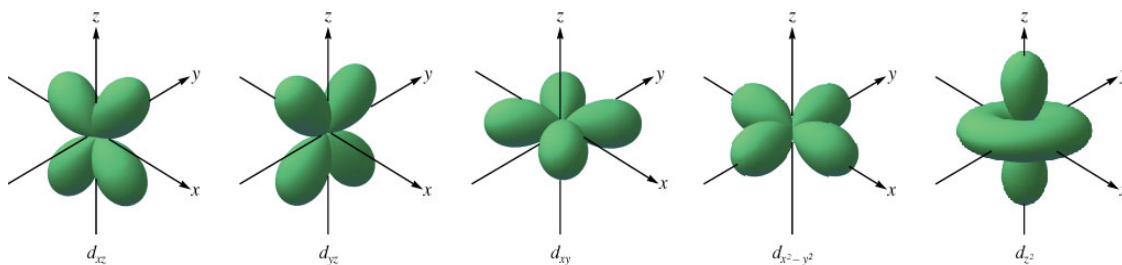


Figure 1.7: Shape of five  $3d$  wave functions. From left,  $d_{zx}, d_{zy}, d_{xy}, d_{x^2-y^2}, d_{z^2}$ .

The five  $3d$  wave functions in Eq. 1.13 to Eq. 1.16 in their real forms allow a qualitative assessment of the effect of various distributions ligand atoms around the central cobalt to its eigen energy. A simple octahedral geometry, i.e.  $O_h$  point group (Figure 1.8a), is assigned below to depict the ligand field of the coenzyme adenosylcobalamin. The six ligands are placed on the axes of a Cartesian coordinate system with the origin at the central cobalt ion. The negative charges of the ligand electrons repel the electrons of the central cobalt.

Based on this octahedral configuration, the  $d_z^2$  and  $d_{x^2-y^2}$  orbitals have their electron density maxima directed along the  $z$  axes and the  $x$  and  $y$  axes respectively, and the  $d_{xy}$ ,  $d_{yz}$ , and  $d_{xz}$  orbitals have their maxima located in the regions between the Cartesian axes, we recognize the hierarchy of the eigen energy of the five  $3d$  orbital of cobalt as the one shown in Figure 8b. Further revision on the energy degeneracy model in Figure 8b was completed according to the X-ray crystallography and density function theory (*B3LYP*) calculation<sup>65</sup>, which suggested that the Co-N bond is 1.9 Å whereas the Co-C bond is 2.0 Å. Based on the experimental result, the degeneracy of  $d_z^2$  and  $d_{x^2-y^2}$  orbitals is lifted and a more accurate eigen energy level is given in Figure 1.8c.

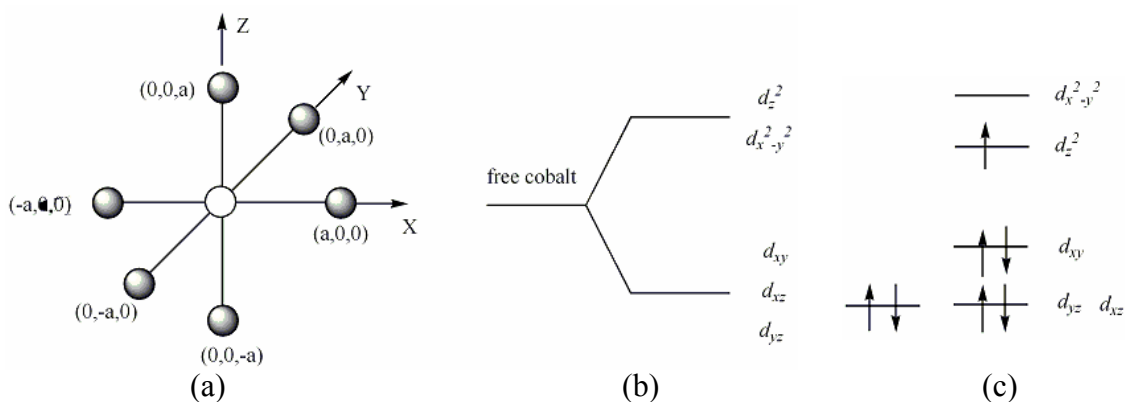


Figure 1.8: Energy level of cobalamin. (a): Simplest model ( $O_h$  symmetry) of the ligand environment of coenzyme adenosylcobalamin; (b): energy level of the five  $d$  electron orbitals based on  $O_h$  symmetry of the ligand field; (c): energy levels of  $3d$  electrons in the low spin  $\text{Co}^{\text{II}}$  oxidation state of cobalamin, assuming a distorted octahedral geometry. Oxidation to the  $\text{Co}^{\text{III}}$  state removes the electron from the  $d_z^2$  orbital, and reduction to the  $\text{Co}^{\text{I}}$  state adds a second electron to the  $d_z^2$  orbital.

In summary, we have shown that the  $\text{Co}^{\text{II}}$  state has an unpaired electron in the  $d_z^2$  orbital, which gives a half-spin EPR signal.

The other unpaired electrons involved in the EAL catalysis are all carbon based, either from the C5' in the deoxyadenosyl moiety, C<sub>1</sub> in the substrate or C<sub>2</sub> in the product

(2 and 3 in Figure 1.9). These unpaired electrons are all in the  $p$  orbital due to the hybridization change from  $sp^3$  to  $sp^2$  hybridization after the break of the  $\sigma$  bond. The details of the  $sp^3$  and  $sp^2$  hybridization are available in many introductory chemistry textbooks and will not be retyped here.

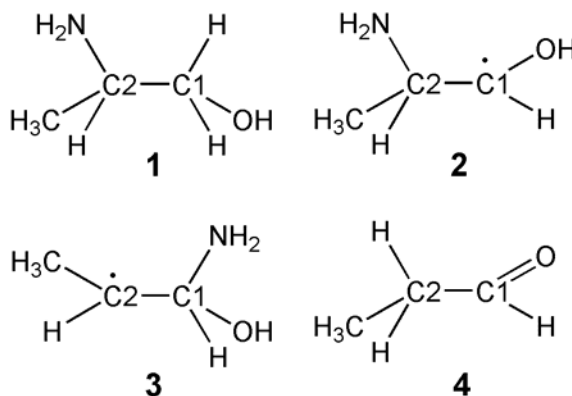


Figure 1.9: Different stages for the substrate molecule in EAL catalytic cycle.

Figure 1.9 shows 4 different stages of the substrate molecule in the catalytic cycle. Among them, only the 2 and 3 states have a free electron on  $C_1$  and  $C_2$ . All of these unpaired electrons are separated in EAL from the unpaired electron in  $\text{Co}^{\text{II}}$  by a distance as far as 11 Å. The electron spins interact with each other through a strong dipole-dipole interaction and a relatively weak isotropic spin-spin interaction. The radical pair Hamiltonian could be expressed as:

$$H = -J\vec{S}_1 \cdot \vec{S}_2 + A_{\perp}(S_{1x}I_{1x} + S_{1y}I_{1y}) + A_{\parallel}S_{1z}I_{1z} + (\vec{\mu}_1 + \vec{\mu}_2) \cdot \vec{B}_0 + \frac{\bar{\mu}_0}{4\pi} \left[ \frac{\vec{\mu}_1 \cdot \vec{\mu}_2}{R^3} - \frac{3(\vec{\mu}_1 \cdot \vec{R})(\vec{\mu}_2 \cdot \vec{R})}{R^5} \right] \quad (1.17)$$

where the  $S_{ij}$  and  $I_{ij}$  are electron and nuclear spin operators,  $B_0$  is the applied magnetic field strength,  $J$  is the isotropic electron-electron coupling constant, the tensor  $\vec{A}$  contains

principal components of the axial cobalt hyperfine tensor, and  $\vec{R}$  is the electron-electron distance vector. In Equation 1.18, the magnetic dipole moment is expressed as follows:

$$\vec{\mu}_i = \beta(g_{ix}S_{ix}\hat{x} + g_{iy}S_{iy}\hat{y} + g_{iz}S_{iz}\hat{z}) \quad (1.18)$$

where  $\vec{\mu}_1$  represents the dipole moment of the electron spin on  $\text{Co}^{\text{II}}$ , and  $\vec{\mu}_2$  corresponds to the dipole moment of the electron spin on the substrate radical. The principal values of the axially-symmetric  $g$  tensors for  $\text{Co}^{\text{II}}$  are  $g_{1x}=g_{1y}=g_{\perp}=2.27$ ,  $g_{1z}=g_{\parallel}=1.99$ . For the substrate radical,  $g_{2xyz}=2$ .<sup>23,25</sup> The nuclear spin of cobalt is  $I=7/2$ , and the cobalt hyperfine terms are  $A_{\perp}=30$  MHz and  $A_{\parallel}=308$  MHz. The electron-electron vector,  $\vec{R}$ , is along the  $z$  direction as defined below.

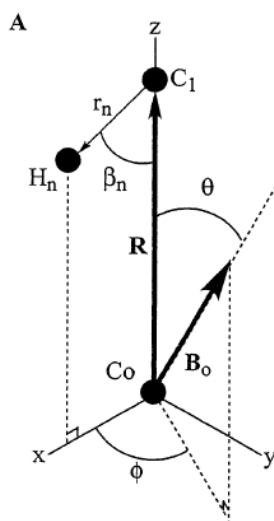


Figure 1.10. The  $xyz$  coordinate system used to define the orientation of the magnetic field vector relative to the active site in EPR.

### 1.2.3 Photochemistry of coenzyme $\text{B}_{12}$

Photochemistry is a branch of chemistry, which focuses on the study of atoms or molecules under electromagnetic radiation. Photochemistry comprises optical absorption

spectroscopy<sup>29,66,67</sup>, photochemical reactions<sup>68,69</sup>, photosynthesis<sup>70,71</sup> and photolysis<sup>72,73</sup>. We will take advantages of two of these subjects, which are the optical absorption [ultraviolet(UV)-visible] spectroscopy and the photolysis, to study coenzyme B<sub>12</sub> in ternary complex with the aim to unravel the mechanism in the Co-C bond cleavage.

A wide range of ligands can occupy the  $\beta$ -axial position, such as CN, OH and Me<sup>4</sup>, each of which bears different UV-visible Abs line shape. The top spectrum in Figure 1.11 shows a typical UV-visible spectrum of cyanocobalamin<sup>29</sup> (CNCbl). Two features are dominant in the spectrum as follows: (1) the so-called  $\alpha/\beta$  bands with an extinction coefficient  $\epsilon$  around 8000 to 10000 M<sup>-1</sup>cm<sup>-1</sup> in the visible spectral region, and (2) the  $\gamma$  band, with  $\epsilon$  around 25000 M<sup>-1</sup>cm<sup>-1</sup> in the UV. The  $\alpha$  band is slightly more intense than the  $\beta$  band. The  $\alpha/\beta$  band is caused by the HOMO  $\rightarrow$  LUMO transition polarized along the long in-plane corrin axis. The  $\gamma$  band is attributed to a corrin  $\pi \rightarrow \pi^*$  transition polarized along the short in-plane corrin axis. Besides these strong bands, two weaker features, termed D and E bands, are observed between the  $\alpha/\beta$  and  $\gamma$  bands.

The bottom spectrum in Figure 1.11 is a unique UV-visible spectrum of adenosylcobalamine<sup>29</sup> (AdoCbl). Comparing the absorption spectra between CNCbl and AdoCbl, we observe a considerable line shape change, especially the shift of  $\alpha/\beta$  bands and spread of  $\gamma$  band, within these two ligands. These differences are caused by the larger  $\sigma$ -donor strength from the alkyl  $\beta$ -axial ligand for CNCbl.

One postulation to explain the tremendous rate enhancement in the Co-C bond cleavage catalyzed by EAL is the corrin ring modulation through side chain interaction<sup>9</sup> (*cis*-effect) and protein-mediated conformational changes after substrate binding that leads to the Co-C bond tilting<sup>4</sup> (substrate-binding trigger effect). From the comparison

between the UV-visible absorption spectra between two different ligands, we propose that, if the dominant effect in the rate enhancement was an enthalpy-base distortion, then a large line shape change would occur. With the successful kinetic arrest of the ternary complex at 230 K, this experiment is straight forward.

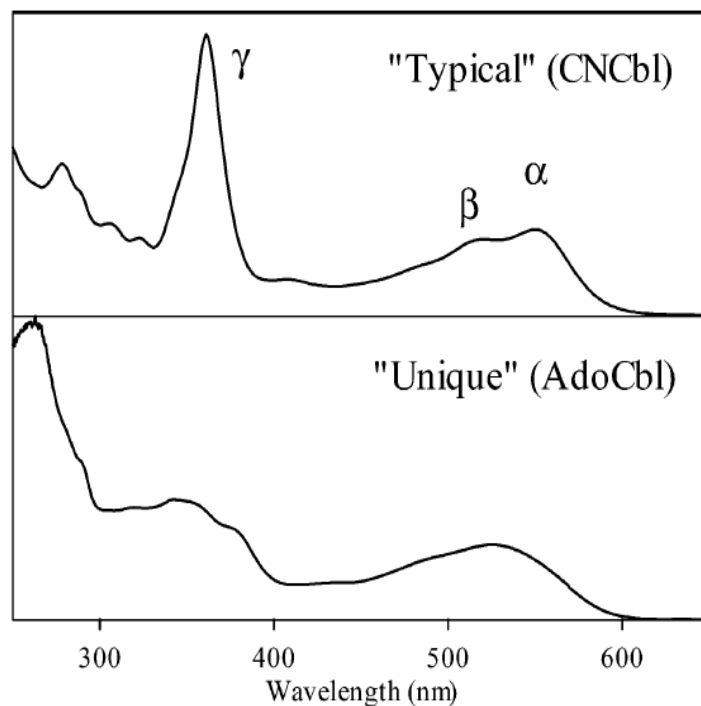


Figure 1.11: UV-visible absorption spectrum<sup>29</sup> for CNCbl and AdoCbl.

The other photochemistry method employed is the photo-induced reaction in enzymes. So far, to our best knowledge, only two photolysis methods have been reported to study isolated reaction steps in metalloproteins. The first method is the low temperature photodissociation of metal-ligand complexes, for which the archetype is the optically monitored carbon monoxide or dioxygen migration and rebinding to the heme iron in myoglobin (Mb) after photolysis of the carboxy or oxy-heme state in frozen solutions at temperatures from 10 to 270 K<sup>74,75</sup>. This method has been further developed

with Mb<sup>76,77</sup>, and has been applied to other heme proteins<sup>78,79</sup> and metalloproteins<sup>80</sup>. The second method is cryoreduction, in which  $\gamma$ -irradiation of a frozen solution sample at 77 K is used to elicit one-electron reduction of a previously redox-poised metal center in the protein. Graded temperature annealing of the kinetically trapped state is subsequently performed to relax the nonequilibrium, reduced metal center structure, and to thermally activate and step through a portion of the electron transfer or reaction sequence. This protocol has been applied to heme<sup>81-83</sup> and nonheme<sup>84,85</sup> iron proteins.

It has been observed that the Co-C bond in AdoCbl undergoes homolysis when exposed to light to generate Co<sup>II</sup> state and the 5'-doxyadenosyl radical.<sup>13</sup> These are the same products that are formed in the enzyme catalysis cycle. Combing this experimental fact with the availability of the ternary complex, we have, for the first time, the ability to investigate the photo-induced enzyme activity.

### 1.3 Outline of Dissertation

To overcome the disadvantages in all previous optical studies and better answer the mechanism for Co-C bond cleavage in the coenzyme B<sub>12</sub>-dependent enzymes, we developed a cryosolvent system to allow us to study the radical pair formation reactions in EAL from *Salmonella typhimurium* at low temperatures (234 K to 248 K) with real-time EPR spectroscopy.

Chapter Two presents the development of the cryosolvent system, which includes three aspects as follows: (1) survey of cryosolvents; (2) application of the optimized cryosolvent to kinetically arrest the EAL·B<sub>12</sub>·substrate ternary complex; (3) instrumental

setup for time-resolved, full spectrum continuous wave EPR in order to investigate the  $\text{Co}^{\text{II}}$ -substrate radical pair formation reaction at subzero temperatures.

After all the necessary preparations, we advance to Chapter Three, in which the temperature-dependence of substrate radical formation was examined from the original state (ternary complex) to the final state ( $\text{Co}^{\text{II}}$ -substrate radical pair). In this chapter, more evidence for the formation of ternary complex after the sample preparation is presented. Another major focus in this chapter is searching for the mysterious 5'-deoxydenasyle radical state and building the kinetic model for the  $\text{Co}^{\text{II}}$ -substrate radical pair formation based on the experimental result. This model is first, to our best knowledge, applied in the coenzyme  $\text{B}_{12}$ -depend enzyme superfamily to obtain the thermodynamic parameters.

Armed with time-resolved, full spectrum continuous wave EPR and 41% DMSO/water cryosolvent system and determined to obtain the microscopic rates for Co-C bond cleavage, we continued the hydrogen isotope effect study in Chapter Four. The experimental result demonstrates that the Co-C bond cleavage is the rate limiting step within the temperature range. A large positive entropy contribution in the Co-C bond cleavage is discovered, which provides insight into the mechanism of EAL. We also extrapolate the thermodynamics parameters to room temperature and show that the transition states of Co-C bond cleavage and HT1 possess similar free energy, which clarifies the role of HT1 in facilitating the Co-C bond cleavage under physiological conditions.

Inspired by the X-ray crystallographic studies on diol dehydrase and Ramman spectroscopic studies on  $\text{B}_{12}$ 's derivative, we desire to obtain the spectra of the ternary complex. The UV-visible optical method was chosen and a home-designed cryostat was

made to couple in a Shimadzu 1600 spectrometer. All the instrumental and experimental results are recorded in Chapter Five. The most valuable information from such study is that the EAL protein does not perturb the Co-C bond at all through direct enthalpic contributions, which is again counter-intuitive but in good agreement with the results from EPR studies.

Chapter Six is the chapter that explores possibility in the future research as photo-initiated enzyme activity. Though the preliminary result shows that photon induced Co-C bond cleavage would not trigger the enzyme's catalysis, it demonstrates the importance of the enzyme-solvent coupled motion in the catalysis and provides support to the previous results.

**Chapter Two**

**Development of Low**

**Temperature Cryosolvent**

**System**

## 2.1 Survey of Cryosolvents

The aim of our research is to study EAL catalysis at subzero temperatures (<273 K) by using EPR spectroscopy. A suitable cryosolvent, which ideally mimics the aqueous solution in terms of *pH*, viscosity, dielectric constant and density, should have the following properties: (1) Suppression of the freezing point of water, in order to allow the addition of substrate at low temperature to form the kinetically arrested ternary complex. (2) Maintenance of the enzyme's native reaction pathway with minimal perturbation, which might be brought by the different physical and chemical properties between the cryosolvent and aqueous solution. Several cryosolvents are screened for this purpose.

### 2.1.1 Cryoenzymology at Subzero Temperatures

One of the important aims of enzymology is to explore the enzyme's dynamics, which consists of a series of successive reaction steps that involves catalytic transformations. However, this goal is often veiled by the following features: (1) Individual catalytic step could occur on a very short time scale, which might vary from sub-nanosecond to milliseconds. (2) Intermediate states could accumulate very low concentration for detection, because of a high energy profile.

To better assist the enzymology study, two experimental approaches have been adapted. One approach is applying fast experimental techniques, such as stopped-flow<sup>86,87</sup>, rapid-flow-quench<sup>88,89</sup>, flash photolysis<sup>90-92</sup>, pressure jump<sup>93</sup> coupled with different transient spectroscopies (UV-visible<sup>86,87</sup>, IR<sup>94</sup>, time-resolve NMR<sup>92</sup>, time-resolved EPR<sup>86,95</sup>, time-resolved Resonance Raman<sup>96</sup>). The other approach is reducing the reaction

rate by lowering the temperature to achieve better time resolution and possible change in rate limiting step. The latter method is called cryoenzymology<sup>97,98</sup>.

Cryoenzymology is a branch of enzymology that comprises experiments in which an enzyme's catalysis is performed in the subzero temperature range. Besides the benefit as slowing down the reaction rate, low temperature condition may accumulate the intermediates along the catalysis pathway, which are undetectable at ambient temperature due to its low concentration, to a level that can be traced and characterized from their spectroscopic features. The information obtained in cryoenzymology studies often lead to Eyring or Arrhenius plots<sup>99</sup>, which yield the elementary activation constants of individual steps. The kinetics under physiological conditions can be obtained through temperature extrapolation from low to high temperature.

Since the early 1970s, cryoenzymology has been widely employed on a large selection of enzymes<sup>100-103</sup>. To prevent the solution from freezing and thereby allowing kinetic analysis at subzero temperatures, several organic solvents are commonly used, due to their low viscosity and similar dielectric constant to water<sup>104</sup>. Among them are ethylene glycol<sup>102,105,106</sup>, methanol<sup>103,106</sup>, dimethyl sulfoxide<sup>100,101</sup> (DMSO) and their ternary mixtures<sup>107</sup>. For the enzyme ethanolamine amino-lyase, because methanol and ethylene glycol inactivate the holoenzyme with an unknown mechanism<sup>108,109</sup>, we use DMSO as the main cryosolvent.

DMSO has a water-like density of 1.101 g/mL at 298 K and a molecular weight of 78.13. Table 2.1 lists the freezing points for different DMSO/water binary mixtures<sup>104</sup>. Figure 2.1 describes the supercooling behavior of DMSO with different DMSO/water (*volume/volume*) ratios<sup>110</sup>.

Table 2.1 DMSO/water (v:v) ratio vs. freezing temperature in K, SC = super cooling<sup>104</sup>

10%	20%	30%	40%	50%	60%	70%	80%	90%	100%
270	261	254	SC	SC	SC	SC	235	266	291.5

The cooling rate for the sample is determined by a home-made cooling system. The heart of this system is a 1/16 *Deutsches Institut für Normung* (DIN) standard MICROMEGA<sup>®</sup> autotune PID temperature/process controller (Omega part number CN77000), which controls a coil heater based on the setting temperature and the feedback voltage from an ultra-thin T-band thermocouple (Omega part number 5STRC-TT-T-30-36) inside a Wilmad Standard VT Dewar Insert. Dry nitrogen gas serves as the cooling mediator for the system by running through a heat exchanging coil (stainless steel) immersed inside liquid nitrogen. The dewar insert is made of *Suprasil*, which is a synthetic fused silica. The system can host 4 mm and 5 mm EPR tubes with the temperature accuracy =  $\pm 1.5$  K in the range from 200 K to 300 K. This home-made system provides a minimum cooling rate of 15 K/min.

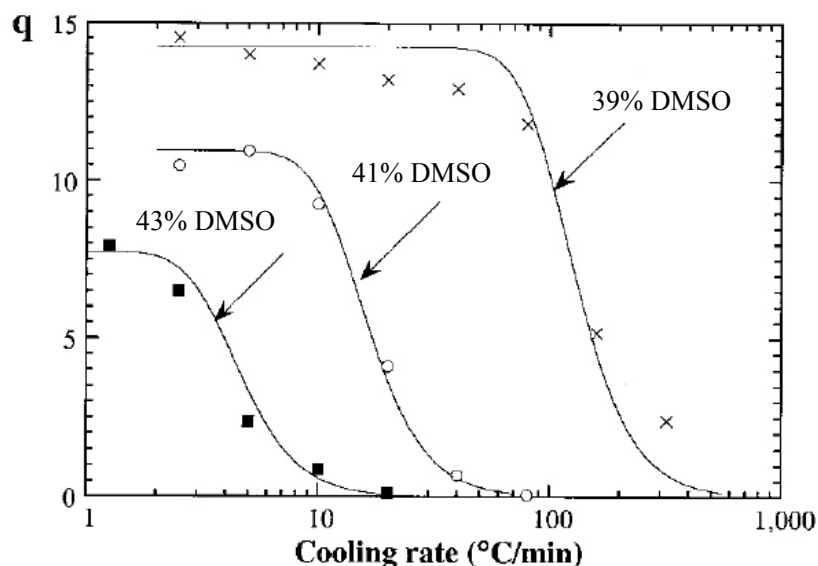


Figure 2.1: The heat of ice crystallization ( $q$ , unit in gram) as a function of sample cooling rate for different DMSO/water concentrations. Symbol  $q$  has a unit as grams of pure H<sub>2</sub>O, the solidification of which at 0°C would liberate the same amount of heat as that of 100 g of tested solution on crossing the corresponding peak. The heat in calories per 100 grams of solution is obtained by multiplying  $q$  by 79.78.

### 2.1.2 VS41A and VS41A-G

The cryoprotectant VS41A was designed by Fahy<sup>111,112</sup> to have a minimized toxicity for rabbit kidney. The ingredients of VS41A is 24.3% (w/w) DMSO, 16.8% (w/w) 1,2-propanediol, 13.9% (w/w) formamide<sup>112</sup>. With these ingredients, VS41A allows a perfusion-washing cycle at temperatures close to 273 K and guarantees a survival rate above 70% from cryoprotection<sup>112</sup>. In this cryosolvent, DMSO is the main cryoprotectant, formamide is assumed to act as a toxicity reducer of DMSO, and 1, 2-propanediol is the vitrification agent.

VS41A-G has similar recipe comparing to VS41A, except that the 1,2-propanediol is substituted by the same weight amount of glycerol. VS41A-G maintains comparable physical properties as VS41A.

The critical cooling rate for VS41A is  $< 1$  K/min and the melting temperature ( $T_m$ ) = 235 K<sup>112</sup>. The minimum cooling rate for our home-made cooling system is 15 K/min, which keeps the VS41A in liquid phase at 230 K.

An excess amount (100 fold more than the EAL active site) of substrate, (S)-2-aminopropanol, is introduced into the holoenzyme after the sample temperature reaches equilibrium at 230 K. Immediately following the substrate mixing step ( $t_{mix} < 2$  min), the sample is cryoquenched in liquid nitrogen at 77 K and an X-band cw EPR spectrum is collected at 120 K. One representative spectrum is shown on the top of Figure 2.2 as a flat background without single trace of paramagnetic state. Then the EAL·B<sub>12</sub>·substrate

ternary complex is annealed at 250 K for about 1 hour. The sample is again immersed into liquid nitrogen followed by another data collection by X-band cw EPR spectroscopy. A paramagnetic state is observed at this time and the spectrum (bottom of Figure 2.2) exhibits the same features as the spectrum<sup>25</sup> of the Co<sup>II</sup>-substrate radical pair, which is formed in the aqueous solution during the EAL catalysis cycle. Longer time incubation of up to another 30 minutes does not change either the line shape nor the amplitude, indicating that the system reaches an equilibrium state.

The time course of the paramagnetic state formation in VS41A-G is identical to VS41A under the same sample preparation and incubation procedure. The data is depicted in Figure 2.3.

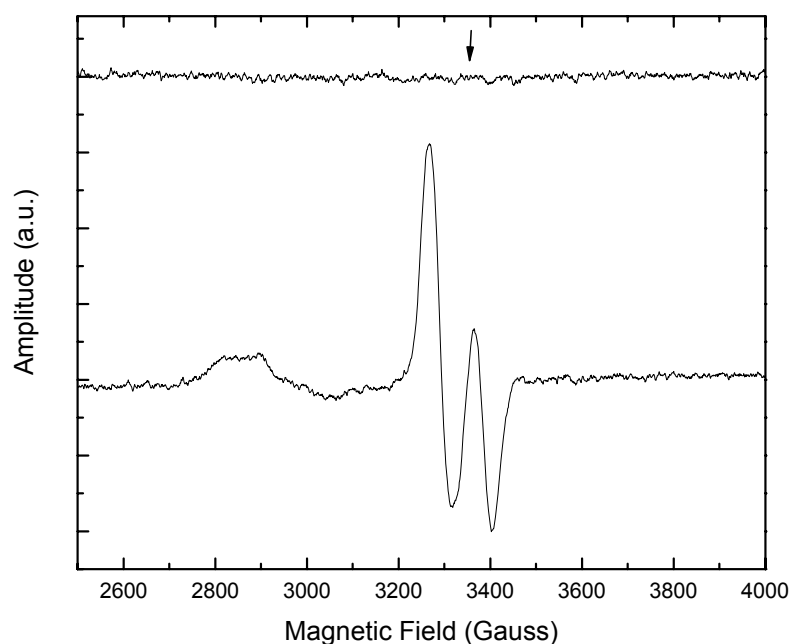


Figure 2.2: EPR spectra of samples prepared in VS41A. (top) EPR spectrum of one EAL holoenzyme sample after mixing with excessive substrate at 230 K in VS41A; (bottom) EPR spectrum of the same sample after 1 hour incubation at 250 K. All spectra are collected at 120 K with 2 scan average. The active site concentration is 120  $\mu$ M and the substrate concentration is 12 mM. The arrow shows  $g=2.0$ .

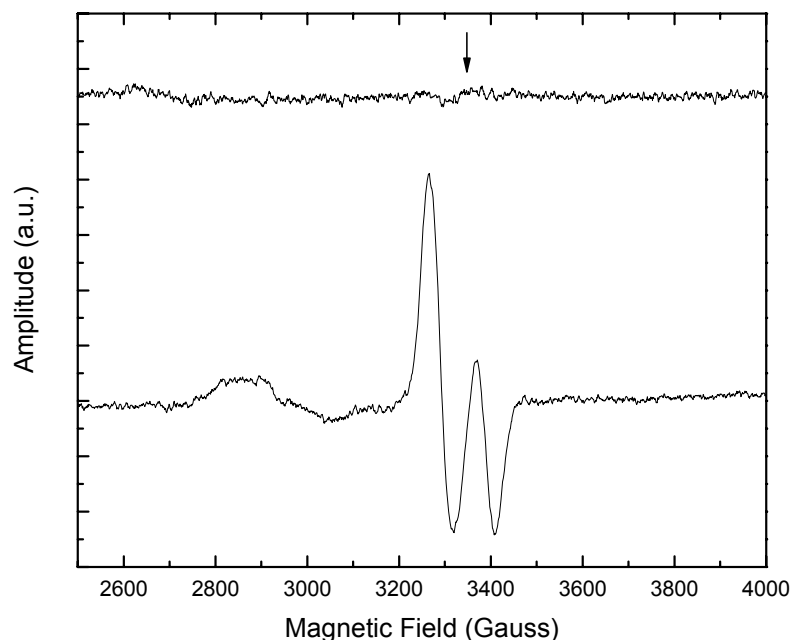


Figure 2.3: EPR spectra of samples prepared in VS41A-G. (top) EPR spectrum of one EAL holoenzyme sample after an introduction of excess substrate at 230 K in VS41A-G; (bottom) EPR spectrum of the same sample after 1 hour incubation at 250 K. All spectra are collected at 120 K with 2 scan average. The active site concentration is 120  $\mu$ M and the substrate concentration is 12 mM. The arrows shows  $g=2.0$ .

### 2.1.3 41% DMSO/water

A DMSO/water (41% *v:v*) cryosolvent was tried in the cryoenzymology studies. Though the recipe is simpler than VS41A and VS41A-G, 41% DMSO/water solution holds a very similar melting point. According to Figure 2.1, the critical cooling rate for 41% DMSO is 12 K/min, which is still less than the cooling rate provided by the home-made instrument. This feature, plus the low melting point, secure the liquid phase condition for this cryosolvent at 230 K, when the substrate is introduced to form the EAL·B<sub>12</sub>:substrate ternary complex.

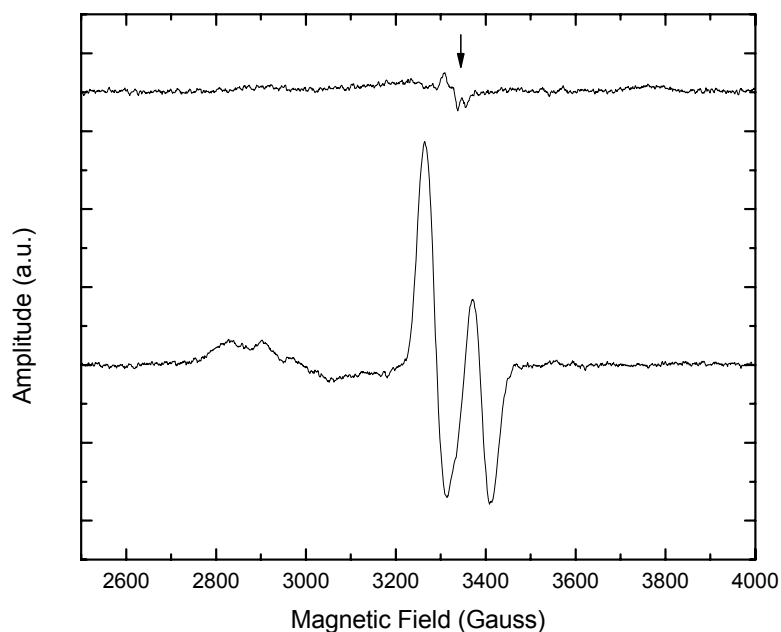


Figure 2.4: EPR spectra of samples prepared in 41% DMSO/water. (top) EPR spectrum of one EAL holoenzyme sample after an introduction of excess substrate at 230 K in 41% DMSO/water; (bottom) EPR spectrum of the same sample after 1 hour incubation at 250 K. All spectra are collected at 120 K with 2 scan average. The active site concentration is 120  $\mu$ M and substrate the concentration is 12 mM. The arrow shows  $g=2.0$ .

The X-band cw EPR scan is given on the top of Figure 2.4 after mixing of two-order-of-magnitude more (*S*)-2-aminopropanol substrate relative to EAL active sites with the holoenzyme at 230 K. Except for a weak narrow line-width free radical signal at  $g = 2.0$ , which is typically observed in  $\text{Co}^{\text{II}}$ -substrate radical pair sample preparations in aqueous solution, no other paramagnetic centers are detected. The bottom spectrum in Figure 2.4 shows the 120 K EPR spectrum of the paramagnetic state formed in EAL in 41% (*v:v*) DMSO/water cryosolvent after 1 hour incubation at 250 K. This spectrum has the same line shape as the bottom spectra in Figure 2.2 and 2.3 and exactly overlaps the spectrum of  $\text{Co}^{\text{II}}$ -substrate radical pair formed in aqueous solution from the EAL catalytic cycle.

Since all of the bottom spectra in Figure 2.2, 2.3 and 2.4 have the same line shape, the first-order derivative EPR signal amplitude, which is measured from the first peak to the second trough within 3200 G to 3450 G, would represent relative concentration of the paramagnetic centers, which are formed during the EAL catalytic cycle by functional EAL active sites. Considering the fact that the initial enzyme concentrations are identical in all the samples, measurement of the EPR amplitude in Figure 2.2, 2.3 and 2.4 yields the following relations:

$$\begin{aligned} [\text{functional EAL active sites}]_{\text{VS41A}} &\approx [\text{functional EAL active site}]_{\text{VS41A-G}} \\ &\approx \frac{1}{2} [\text{functional EAL active sites}]_{41\% \text{ DMSO/water}} \end{aligned} \quad (2.1)$$

at 250 K after the system reaches an equilibrium state.

#### 2.1.4 Concluding Remarks

All the cryosolvents tested have achieved the following goals: (1) the mixing of holoenzyme and substrate in liquid phase leads to an EPR-silent state; (2) after high temperature incubation, paramagnetic state(s) formed and exhibit an EPR spectrum identical to the  $\text{Co}^{\text{II}}$ -substrate radical pair state cryotrapped in aqueous solution.

Though all of them show similar melting point, the 41% DMSO/water binary cryosolvent best maintains the enzyme's ability for form the same intermediate state, which is almost doubled relative to the other two cryosolvent systems within the subzero temperature range. In all the samples prepared, the relative ratio of EAL active sites that remain catalytic abilities in the cryosolvent at subzero temperatures is on average 80%.

The reason for the decline within VS41A and VS41-G on the enzyme's ability to accumulate intermediate state possibly arises from the hydroxyl group in 1,2-propanediol molecule for VS41A and ethylene glycol molecule for VS41-G. Since it has been

demonstrated that ethylene glycol, which has two hydroxyl groups in each molecule, inactivates the holoenzyme with an unknown mechanism<sup>108,109</sup>.

## 2.2 Kinetic Arrest of Ternary Complex at 230 K

The 41% DMSO/water binary complex has been selected to serve as the cryosolvent for our cryoenzymology studies on EAL. The structure of DMSO is drawn in Figure 2.5 and it is clear that DMSO behaves only as a hydrogen bond acceptor.

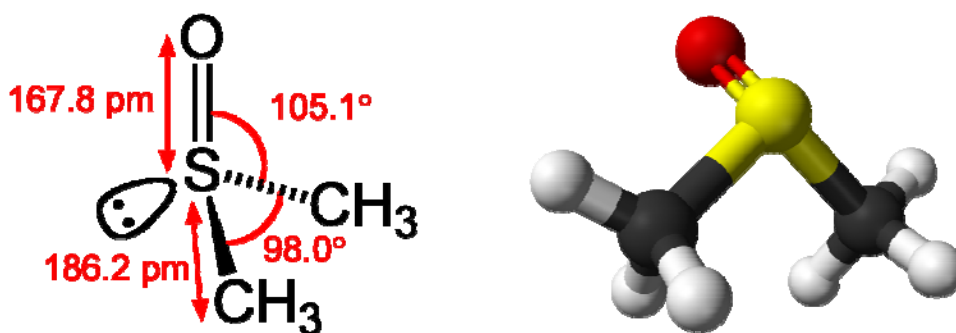


Figure 2.5: The 3D structure of DMSO.

In 41% (v:v) DMSO/water cryosolvent, the mole fraction of DMSO molecule is 0.15. It means that the number ratio between DMSO and H<sub>2</sub>O is roughly 1: 5. The physical properties of this cryosolvent, including density ( $\rho$ ), viscosity ( $\eta$ ) and dielectric constant ( $D$ ) closely mimics the aqueous solution properties, in order to maximize the enzyme's functionality. To realize the goal of enhanced enzyme yield, improvements on (1) the cryosolvent introducing procedure; (2) the *pH*-balancing protocol at subzero temperatures have been accomplished.

### 2.2.1 Physical Properties of 41% DMSO/water Cryosolvent

The three parameters, which are density ( $\rho$ ), viscosity ( $\eta$ ) and dielectric constant ( $D$ ), are often utilized to describe the properties of a liquid solution. All of these properties are related to the strength of the hydrogen bonds formed in the solution, and are thereby temperature dependent. For comparison, at 293 K, the density for H<sub>2</sub>O is 0.998 g/ml, the viscosity is 1.0020 cP and the dielectric constant is 80.4<sup>104</sup>. To evaluate the physical constants for 41% DMSO/water binary complex, a polynomial extrapolation is made from the available data on different DMSO/water binary complex with various concentrations<sup>104,113,114</sup>.

Figure 2.6 shows the density for 41% (v:v) DMSO/water complex. For the purpose of comparison, the data for 50% DMSO/water cryosolvent is also included. The temperature dependence on density could be fit with a straight line as:

$$\rho = 1.247 - 6.48 \times 10^{-4} T \quad (2.2)$$

in which  $\rho$  is the solvent density in the unit of g/cm<sup>3</sup> and  $T$  is temperature with unit K. At 240 K, around which the cryoenzymology study on EAL will be performed, the density of 41% DMSO/water cryosolvent is 1.09 g/cm<sup>3</sup>. When comparing with other solvents, the density of the 293 K aqueous solution is 8% less than this value and the density of 240 K 50% DMSO/water cryosolvents is 2% more than this number.

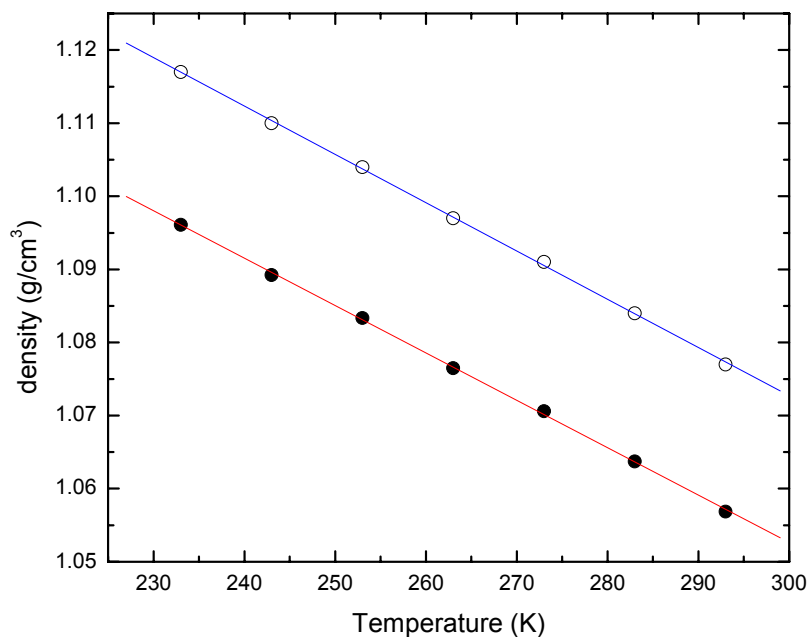


Figure 2.6: Temperature dependence of the density of DMSO/water cryosolvent. The solid circle is for 41% DMSO/water cryosolvent, hollow circle is for 50% DMSO/water cryosolvent.<sup>104,113,114</sup>

Figure 2.7 shows the data for the viscosity values of 41% (v:v) DMSO/water cryosolvent at different temperatures.<sup>104,113,114</sup> Again, for comparison purpose, the viscosity of 50% DMSO/water cryosolvent is added in the plot. The data points could be fit in an Arrhenius type plot as :

$$\log \eta = -5.3 + 1600/T \quad (2.3)$$

in which  $\eta$  is the viscosity of the cryosolvent in the unit of cP and  $T$  is the temperature in unit K. At 240 K, the viscosity of 41% DMSO/water cryosolvent is 23 cP. When comparing with other solvents, the viscosity of the 293 K aqueous solution is 96% less than this value and the viscosity of the 240 K 50% DMSO/water cryosolvents is 74% more than this number.

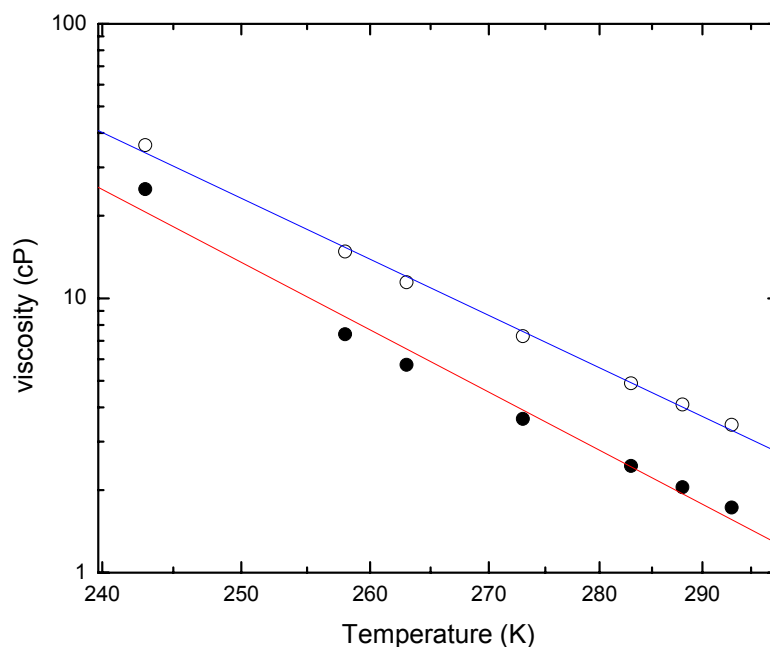


Figure 2.7: Temperature dependence of the viscosity of DMSO/water cryosolvent. The solid circle is for 41% DMSO/water cryosolvent, hollow circle is for 50% DMSO/water cryosolvent.

Figure 2.8 shows the dielectric constant for 41% (v:v) DMSO/water complex at various temperatures.<sup>104,113,114</sup> For comparison, the data for 50% DMSO/water cryosolvent is also depicted. It is obvious that all the data points lie along a straight line which could be expressed as:

$$D = 195.1 - 0.4T \quad (2.4)$$

in which  $D$  is the dielectric constant, which is unitless, and  $T$  is temperature with unit K. At 240 K, the dielectric constant of 41% DMSO/water cryosolvent is 99.1. When comparing with other solvents, the dielectric constant of the 293 K aqueous solution is 19% less than this value and the dielectric constant of 240 K 50% DMSO/water cryosolvent at 240 K is 3% less than this number.

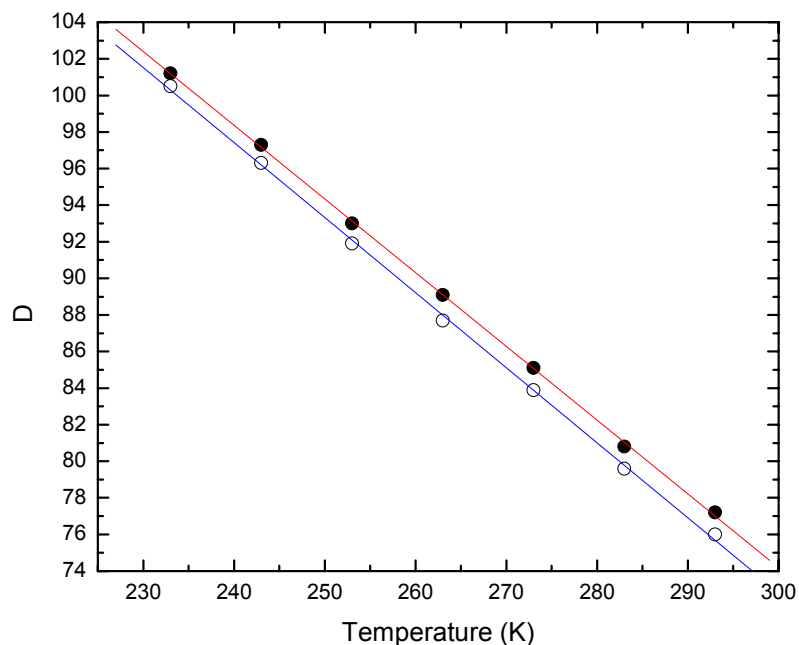


Figure 2.8: Temperature dependence of the dielectric constant of DMSO/water cryosolvent. The solid circle is for 41% DMSO/water cryosolvent, and the hollow circle is for 50% DMSO/water cryosolvent.

Based on the evaluation on density, viscosity and dielectric constant in Figures 2.6, 2.7, 2.8, the most dissimilar physical property between the low temperature 41% DMSO/water cryosolvent and the room temperature aqueous solution is the solvent viscosity. In the following chapter, the impact brought by this difference will be assessed on the EAL's ability to accumulate the intermediate and the experimental results will prove that the EAL catalysis is viscosity independent up to 40 cP.

### 2.2.2 pH-balancing at Subzero Temperature

It is well known that acid-base equilibria are altered by the addition of organic solvents, due to the change in dielectric constant and medium basicity<sup>104</sup>. The temperature dependence on  $pH$  for various buffers in different hydro-organic mixtures has been measured<sup>115,116</sup>. The results are commonly plotted in the form of  $pH$  as a

function of  $1/T$ . Under the low ionic strength condition<sup>117</sup> ( $< 100$  mM), all of the results are linear over the temperature range from 223 K to 293 K. Based on this linear behavior, we can obtain the temperature dependence at subzero temperature on the  $pH$  value of 41% DMSO/water cryosolvent with various buffers by extrapolating the data from 273 K to 298 K, which can be directly measured by a Corning  $pH$  glass electrode probe (Part number 476156).

As shown in Figure 1.5, EAL has a broad  $pH$  optimum range<sup>40</sup> from 6.6 to 8.2. This is primarily due to its robust TIM-barrel structure<sup>61</sup> of EutB, all the kinetic information (data in Table 1.1) are measured under biological condition, in which the  $pH$  of the solution is adjusted to 7.5 by potassium phosphate buffer. With this consideration, the  $pH$  value of the desired cryosolvent should fall into the range from 6.6 to 8.2 from 230 K, at which temperature the substrate is introduced, to 298 K, at which temperature the holoenzyme is prepared.

For the traditional potassium phosphate buffer, if a buffered aqueous solution is adjusted to  $pH$  7.0 before introducing DMSO, after adding the DMSO to achieve 41% (v:v) DMSO/water concentration, the temperature dependence on  $pH$  is determined to satisfy the following equation:

$$pH = 3.2 + 1470/T \quad (2.5)$$

From Figure 2.9, the  $pH$  variance for the phosphate buffer from 230 K to 298 K is so large that it could not secure the solvent to maintain a  $pH$  range from 6.6 to 8.2.

After a survey of the temperature dependence for various buffers on  $pH$  by following the same procedure, the potassium cacodylate buffer<sup>118</sup> (structure shown in Figure 2.9) stands out due to its low temperature dependence. The  $pH$  temperature

dependence for a 5.3 mM potassium cacodylate buffer in 41% DMSO/water solvents could be fit by the function:

$$pH = 3.98 + 1010/T \quad (2.6)$$

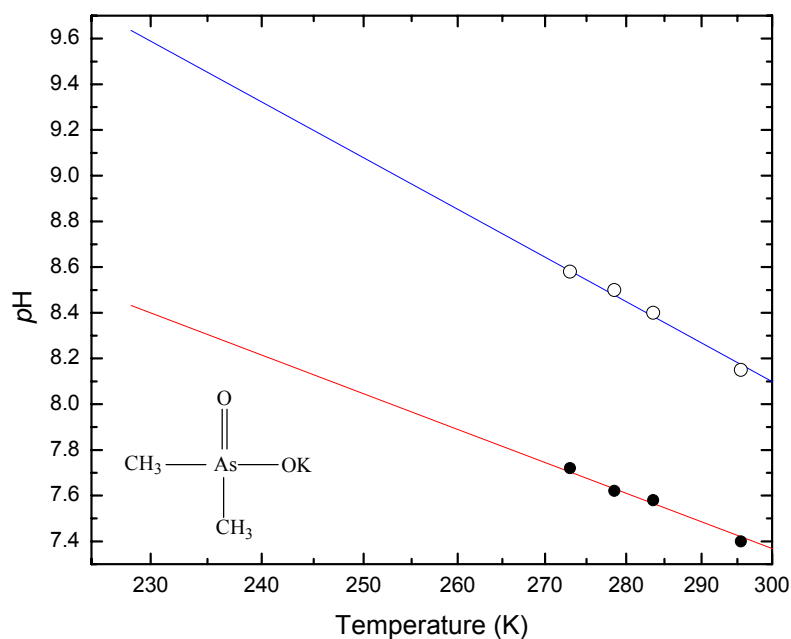


Figure 2.9: Temperature dependence of the  $pH$  for 41% DMSO/water cryosolvent with different 5.3 mM buffer. The solid circle is for potassium cacodylate buffer, hollow circle is for potassium phosphate buffer. The initial  $pH$  values for the buffered aqueous solution before adding the DMSO are both 7.0 at 293 K.

As observed from the right panel in Figure 2.9, the following  $pH$  conditions are secured by using the potassium cacodylate buffer: (1) The buffered aqueous solution, in which the EAL protein is stored and the holoenzyme is prepared, has a  $pH$  of 7.0 at ambient temperature; (2) The  $pH$  value from 230 K to 270 K after introduction of the DMSO is from 8.4 to 7.8, which is within the desired  $pH$  range to maximize the EAL activity.

### 2.2.3 Procedure to Introduce Substrate at 230 K

To achieve the EAL·B<sub>12</sub>·substrate ternary complex, the first step is the preparation of the holoenzyme by adding 1.5-fold excess of adenosylcobalamin relative to EAL active sites into buffered (10 mM potassium cacodylate) aqueous EAL apoenzyme solution at 295 K. Then the DMSO is introduced into the solvent to suppress the freezing point. To avoid pH and dielectric constant shock, small volumes of 70% (v/v) DMSO/water solvent (less than 15% of the volume of the holoenzyme-containing solution) are added with continuous slow mixing in four steps at decreasing temperatures over the range from 273 to 240 K, to achieve a final 41% (v/v) DMSO/water solution with holoenzyme. In the last step, the substrate, (*S*)-2-aminopropanol, in 41% (v:v) DMSO/water cryosolvent is mixed with holoenzyme at 230 K. At this temperature, the system still maintains the liquid phase. The whole EAL·B<sub>12</sub>·substrate ternary complex is incubated for 2-3 min at 230 K to allow the substrate molecules to bind to the active site. All the procedures, as depicted in Figure 2.10 and described in the Appendix, are performed under a dim red safe light in the home-made cryostat.

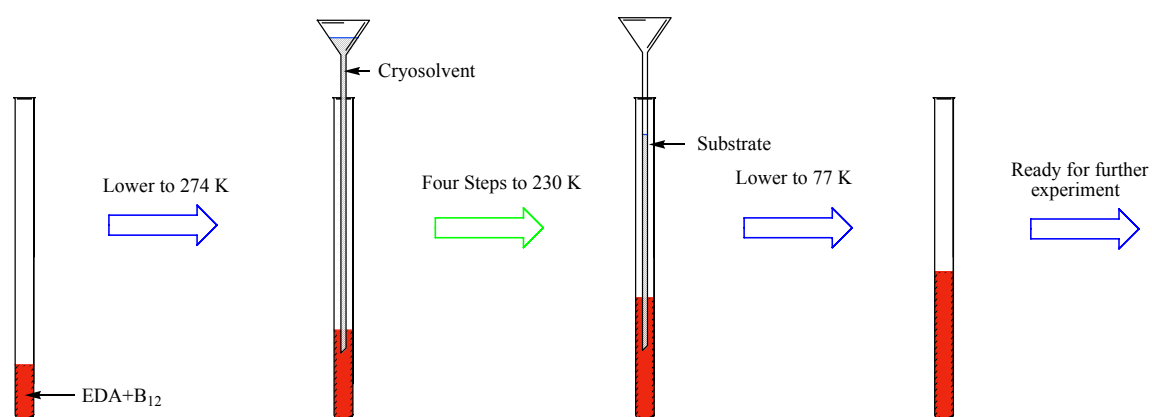


Figure 2.10: Minimum sample preparation scheme.

### 2.2.4 Spectroscopic Evidence for Ternary Complex

To confirm that the enzyme does not start the catalysis cycle after substrate binding at 230 K. The EPR spectrum at 6 K has been employed as a tool with higher sensitivity relative to  $T=230-249$  K in detecting any paramagnetic intermediate state. This is owing to the higher Signal to Noise Ratio (*SNR*) for EPR signal at low temperature, which is generated by more population in the ground state according to Eq. 1.3, and longer spin-spin relaxation time.

In such an experiment, an  $EAL \cdot B_{12}$ ·substrate ternary complex sample is prepared as described in the Appendix. The sample is then made anaerobic by using three cycles of freeze-vacuum-thaw sequence and backfilled with argon gas at 230 K. The whole process is finished within 5 minutes. Then the sample temperature was rapidly lowered to 77 K by immersion in liquid nitrogen.

X-band CW-EPR spectroscopy at 6 K is sequentially acquired on this sample in the Bruker ELEXSYS E500 spectrometer with an ER 4123SHQE X-band resonator. The 6 K temperature is achieved with an Oxford Instruments ESR-900 continuous-flow liquid helium cryostat and Oxford 3120 temperature controller. To increase *SNR*, the field sweep rate is set to 3.7 G/s and 8 scans are accumulated.

The collected spectrum shows no EPR signal, except the background and a weak signal around  $g = 2.0$ . Expanding the range of the magnetic field sweep to 50-5000 G, which would include the region of the “half-field transition” for strongly coupled radical pairs<sup>23,62</sup>, also did not reveal any EPR signal. Parallel EPR in a dual mode resonator has also been applied in search for the integer spin system, but the result is also null.

The results show that the Co-C bond cleavage has not been trigger to form any radical state after completing the substrate mixing procedure at 230 K, and the addition of the DMSO does not generate any protein-associated radical.

### 2.2.5 Concluding Remarks

This section described the careful design of a sample preparation procedure to introduce the substrate into EAL holoenzyme at 230 K with minimum shock to the enzyme. Multiple EPR spectroscopy methods, which include EPR at 6 K, EPR at half-field and parallel-mode EPR, have been performed to confirm that the enzyme is under kinetic arrest with absence of paramagnetic signals before the initial Co-C bond cleavage step.

## 2.3 Substrate Radical Pair Formation at Subzero Temperatures

After preparing the ternary complex by following the previously described procedure, the sample is annealed at a higher temperature  $T$  ( $234 \text{ K} \leq T \leq 248 \text{ K}$ ) for a certain time of period  $t_i$ . Then a cw-EPR spectrum is collected on this sample at 120 K and the amplitude of peak to trough ( $A_{\text{pt}}$ ) is obtained. By measuring the  $A_{\text{pt}}$  for a series of spectra (each associated with an incubation time period  $t_i$ ), the time course of the paramagnetic intermediate state could be obtained. The important conclusions obtained from this  $A_{\text{pt}}$  time course study are: (1) the  $A_{\text{pt}}$  reaches an equilibrium after certain amount of time within the temperature range from 234 K to 248 K; (2) spectrum line shape does not change at different incubation time point. To set up a reaction model, it is

necessary to determine the nature of the paramagnetic state(s) formed during the time course of the high temperature incubation.

### 2.3.1 EPR Study for the Free Radical Formed at 242 K

An anaerobic EAL·B<sub>12</sub>·substrate ternary complex sample is incubated at 242 K for 90 minutes before cryotrapping in liquid nitrogen. X-band cw-EPR spectrum at 6 K is acquired on this sample. To increase the *SNR*, the field sweep rate is set to as slow as 3.7 G/s and 8 scans are accumulated.

An EPR signal, which precisely overlaps with the Co<sup>II</sup>-substrate radical pair spectrum in aqueous solution, is observed in Figure 2.11A. Except for this line shape, no other EPR signals are detected. To confirm that the detected EPR signal, which is formed during the high temperature incubation, represents the Co<sup>II</sup>-substrate radical pair state, an EPR simulation (Figure 2.11B) was carried out by using the program, MENO<sup>119,120</sup> coded in Matlab, with the inclusion of a simplex direct search optimization algorithm, as described previously,<sup>25</sup> according to the Hamiltonian described in the Introduction for the Co<sup>II</sup>-substrate radical pair. To optimize the fit, *J*, *R* (defined in Eq. 1.17) and Gaussian line width parameters for Co<sup>II</sup> and the substrate radical are varied. The fitting results are presented in Table 2.2, which also shows the parameters reported for the Co<sup>II</sup>-radical pair state formed in EAL in aqueous solution at ambient temperature.<sup>25</sup> Table 2.2 shows that the *J* and *R* values are comparable for the Co<sup>II</sup>-substrate radical pair states formed in cryosolvent at 242 K and in aqueous solution at ambient temperature (295 K). The *J* and *R* values are also in agreement with those obtained for the (*S*)-2-aminopropanol-generated Co<sup>II</sup>-substrate radical pair in EAL by other groups.<sup>23,121</sup>

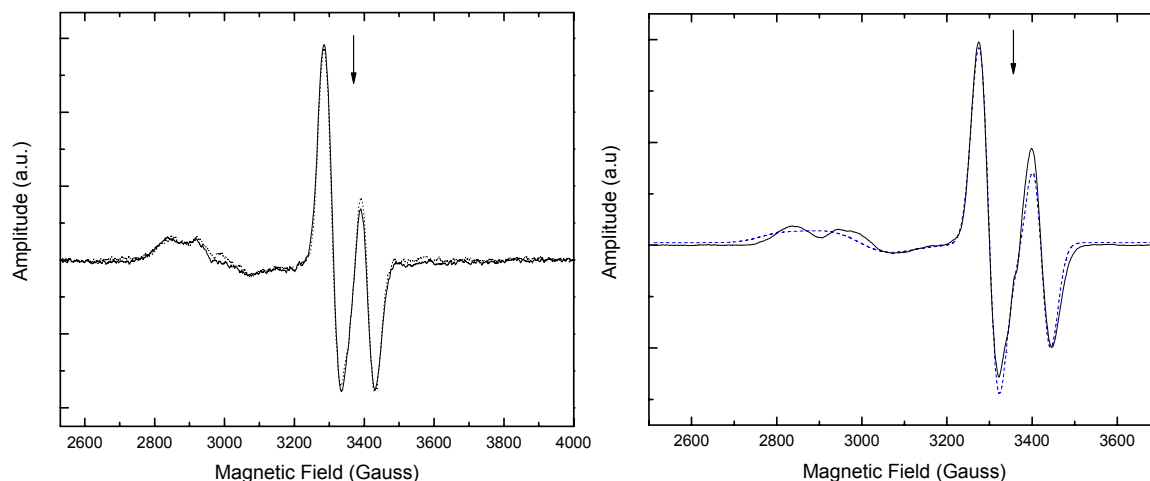


Figure 2.11: EPR spectrum of the cryotrapped  $\text{Co}^{\text{II}}$ -substrate radical pair in 41% DMSO/water cryosolvent after equilibration at  $T=242$  K. Left figure: (A) overlaid with the  $\text{Co}^{\text{II}}$ -substrate radical pair in aqueous solution. The spectrum was collected at 120 K. Right figure: (B) overlaid with EPR simulation (blue dashed line). The spectrum was collected at 6 K. The free electron resonance position at  $g=2.0$  is shown by the arrow. The substrate and EAL active site concentrations were 7.5 mM and 150 M, respectively. In the simulation, the principal values of the  $g$  tensors are fixed, as follows: For  $\text{Co}^{\text{II}}$ ,  $g_{1x}=g_{1y}=g_{\perp}=2.27$ ,  $g_{1z}=g_{\parallel}=1.99$  and for the substrate radical,  $g_{2xyz}=2$ .<sup>23,25</sup> The nuclear spin of cobalt is  $I=7/2$ , and the cobalt hyperfine terms are  $A_{\perp}=30$  MHz and  $A_{\parallel}=308$  MHz<sup>25</sup>. The electron-electron vector,  $\vec{R}$ , is along the  $z$  direction. *Conditions for the 6 K EPR*: microwave frequency, 9.378 GHz; microwave power, 30 dB (0.2 mW); magnetic field modulation, 10 Gauss peak-peak; modulation frequency, 100 kHz; field sweep rate, 3.7 Gauss  $\text{s}^{-1}$ ; time constant, 164 ms; average of 8 spectra, minus baseline. Simulation parameters are given in Table 2.2.

Table 2.2: EPR simulation parameters for the  $\text{Co}^{\text{II}}$ -substrate radical pair formed in low temperature 41% DMSO/water cryosolvent at 242 K and in aqueous solution at 295 K.

<i>Fitting parameters</i>	<i>Best-fit values in cryosolvent</i>	<i>Best-fit values in water</i>
<b><math>J/\text{MHz}</math></b>	-330	-324
<b><math>R/\text{\AA}</math></b>	10.9	11.1
<b>Radical line width/Gauss</b>	44.4	48.7
<b><math>\text{Co}^{\text{II}}</math> line width/Gauss</b>	90.3	13.9 <sup>a</sup>

<sup>a</sup> The reported aqueous solution EPR spectrum was obtained as the ESE-EPR absorption spectrum, in which the Co<sup>II</sup> amplitude was a factor of 0.27 relative to the substrate radical amplitude.<sup>25</sup> The line width parameter was not comparable between the two simulations.

Since it is critical to confirm that the paramagnetic state, formed during the high temperature incubation, is the Co<sup>II</sup>-substrate radical pair, we examine the sensitivity of the EPR spectrum toward the parameters  $J$  and  $R$ . Varying the radical pair separation by only  $\pm 1$  Å leads to a significant line shape change on the EPR spectrum that the position of the low field peak is shifted at least by 50 G. Varying the  $J$  couple strength while holding the radical pair separation distance constant also leads to an observable line shape change. All the simulation results are given in Figure 2.12.

The variation of the simulation parameters in Figure 2.12 demonstrates that the cw EPR line shape is very sensitive to the radical pair geometry. Other experimental results, which include orientation-selection pulsed-EPR studies in EAL and X-ray crystallographic studies of the coenzyme B<sub>12</sub>-dependent diol dehydratase enzyme<sup>54</sup>, which is mechanistically<sup>4</sup> and structurally<sup>60</sup> similar to EAL, show that the Co<sup>II</sup>-C1 and Co<sup>II</sup>-C2 distances are not equal. Therefore, the line shape match does indicate that the radical species in the cryosolvent corresponds to the Co<sup>II</sup>-substrate radical, and not the product radical.

In search for other radical states, the “half-field transition” for strongly coupled radical pairs is again performed from 50-5000 G on the sample. This effort did not reveal any EPR signal. Parallel mode EPR has also been applied with a result that does not show any integer spin systems.

Therefore, the paramagnetic state, which is present after the incubation at 242 K, is the Co<sup>II</sup>-substrate radical pair. If there were any other radicals, the 6 K EPR spectrum

determines that the upper limit for their concentration is less than  $10^{-3}$  of the  $\text{Co}^{\text{II}}$ -substrate radical pair.

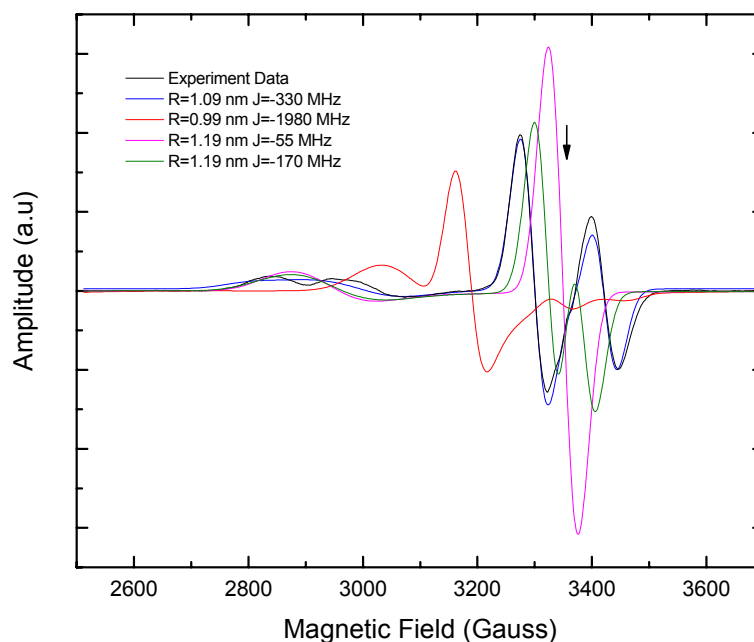


Figure 2.12: EPR line shape variation from changes on radical pair distance ( $\pm 1 \text{ \AA}$ ).

### 2.3.2 Characterization of the Substrate Radical Reaction to Form the Product Radical

As described in the beginning of this chapter 2.3, the  $A_{\text{pt}}$  for  $\text{Co}^{\text{II}}$ -substrate radical pair reaches equilibrium after certain time of high temperature incubation. To retrieve the exact life time of the equilibrated  $\text{Co}^{\text{II}}$ -substrate radical pair state, the substrate radical pair decay time course is studied.

Besides the situation for excess substrate in the ternary complex sample, it has been observed that the  $\text{Co}^{\text{II}}$ -substrate radical pair state formed under the condition:  $[\text{substrate}]/[\text{active site}] \leq 1$ , is also stable on the time scale of the kinetic measurements at each temperature. This suggests that the rate constant for the rearrangement of the

substrate radical to the product radical (step 3 in Figure 1.2) is significantly smaller than the inverse of the kinetic measurement time.

To test this conclusion, the rate constant for decay of the  $\text{Co}^{\text{II}}$ -substrate radical pair at a higher temperature under the condition:  $[\text{substrate}]/[\text{active site}] \leq 1$ , is measured. The corresponding Arrhenius activation energy is calculated and then used to estimate the rate constant at lower temperatures. The reason for measurements at a higher temperature, which is greater than 250 K, is that a complete decay curve can be obtained within a reasonable time scale.

Figure 2.13 shows one substrate radical decay experiment at  $T=270$  K. The data in Figure 13 is collected by using the temperature step method<sup>122</sup> of alternately holding the sample at  $T=270$  K for a time interval, and then lowering to  $T=120$  K for EPR spectrum acquisition. The first-order rate constant for the decay ( $k_{\text{dec}}$ ) is  $1.5 \times 10^{-3} \text{ s}^{-1}$ , which corresponds to an Arrhenius activation energy of 19.3 kcal/mol (from Eq. 12, with  $A=kT/h$ ). This  $E_a$  value is consistent with rates reported previously for the optically-monitored decay of cob(II)alamin to adenosylcob(III)alamin following substrate depletion at room temperature.<sup>17,18,123</sup> Extrapolation of the  $\text{Co}^{\text{II}}$ -substrate radical decay rate constant to 234-248 K by using the Arrhenius relation with  $E_a=19.3$  kcal/mol gives corresponding values for  $k_{\text{dec}}$  of  $4.6 \times 10^{-6} \text{ s}^{-1} - 5.1 \times 10^{-5} \text{ s}^{-1}$ , respectively. This corresponds to  $\tau_{\text{dec}}=2.2 \times 10^5 \text{ s}=6.0 \times 10^1 \text{ h}$  at 234 K and  $\tau_{\text{dec}}=2.0 \times 10^4 \text{ s}=5.5 \text{ h}$  at 248 K. The value of  $\tau_{\text{dec}}/\tau_{\text{obs}}$  is therefore  $\sim 10^2$  over the temperature range, which indicates that the rate of rearrangement of substrate radical to product radical is negligible on the time scale of  $\text{Co}^{\text{II}}$ -substrate radical formation. Therefore, we can approximate the reaction of the ternary complex to form the  $\text{Co}^{\text{II}}$ -substrate radical pair as a relaxation to equilibrium.

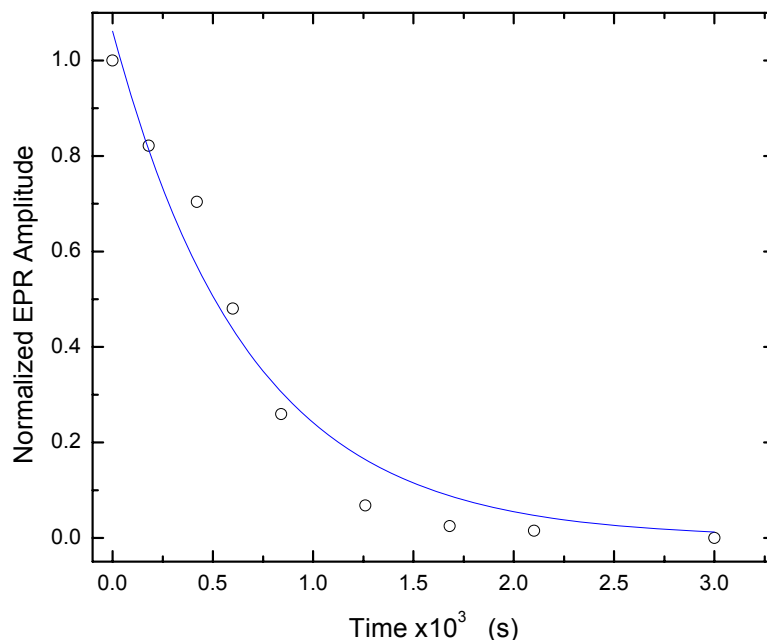


Figure 2.13. Time-dependence of the decay of the substrate radical EPR amplitude at 270 K in the cryosolvent system under conditions of approximately stoichiometric substrate:active sites. The sample was prepared at 230 K and temperature-stepped to 270 K, to initiate the reaction. The sample temperature was then alternately held at 270 K for the indicated time intervals and lowered to 120 K for EPR spectrum acquisition. The sample contained 160  $\mu\text{M}$  substrate and 180  $\mu\text{M}$  active sites. The amplitude is normalized to the initial amplitude following the temperature jump to 270 K. The dashed curve shows the fit of a mono-exponential decay function to the data ( $k_{\text{dec}}=1.49\times 10^{-3} \text{ s}^{-1}$ ).

### 2.3.3 Viscosity Dependence on EAL's Kinetics

As mentioned earlier, the physical property that differs most between the 41% DMSO/water and the aqueous solution is viscosity. Therefore, it is vital to probe the impact on the EAL's kinetics by viscosity variation, in order to show any correlation between the solvent viscosity and the kinetic information obtained from experiments. From the physical property comparison between the 41% and 50% DMSO/water cryosolvents in Figure 2.6, 2.7 and 2.8, the density and dielectric constant differences are both within 5% at 246 K but the viscosity difference is significant. According to the fitting result, viscosity for the 41% DMSO/water solvent at 246 K is 16 cP, whereas

viscosity for the 50% DMSO/water solvent at 246 K rises up to 28 cP. By substituting the cryosolvent from 41% DMSO/water to 50% DMSO/water solution, we could assess the impact on the EAL's activity due to the viscosity change at subzero temperatures.

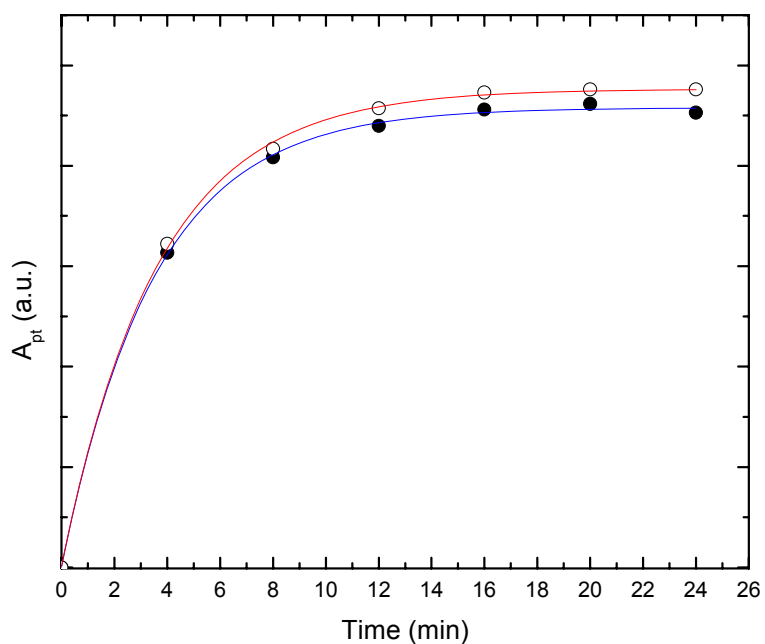


Figure 2.14: Time-dependence of the growth of the substrate radical EPR amplitude at 246 K in 41% and 50% DMSO/water cryosolvent systems. The sample was prepared at 230 K and temperature-stepped to 246 K to initiate the reaction. The sample contained 18 mM substrate and 180  $\mu$ M active sites. The curve shows the fit of a mono-exponential growth function to the data. The solid circle is for 50% DMSO/water cryosolvent, hollow circle is for 41% DMSO/water cryosolvent.

Figure 2.14 shows the  $A_{pt}$  time course at  $T=246$  K for 50% and 41% DMSO/water cryosolvents. The data in Figure 14 are collected by using the same temperature step method of alternately holding the sample at  $T=246$  K for a time interval, and then lowering to  $T=120$  K for EPR spectrum acquisition. The first-order rate constant for the growth ( $k_{\text{growth}}$ ) is  $0.28 \text{ min}^{-1}$  for 50% DMSO/water cryosolvent and  $0.27 \text{ min}^{-1}$  for 41% DMSO/water cryosolvent. This results show that the EAL's ability to form the  $\text{Co}^{\text{II}}$ -

substrate radical pair is viscosity insensitive within the subzero temperature range up to viscosity of 30 cP. Since the viscosity of the 41% DMSO/water is less than this value from 234 K to 250 K, no viscosity correlation will be made.

### 2.3.4 Concluding Remarks

This section is dedicated to the investigation of the paramagnetic state formed during the temperature step from 230 K to a higher incubation temperature. Multiple EPR spectroscopic methods plus spectrum simulation have been carried out. All the results support that the  $\text{Co}^{\text{II}}$ -substrate radical pair is the only EPR-detectable species during the reaction time course of the ternary complex. The population of any possible paramagnetic states that are present along with the  $\text{Co}^{\text{II}}$ -substrate radical pair is less than 0.1% of the total population for all the paramagnetic centers. This conclusion makes a critical contribution to the reaction models that are mentioned in the following chapters.

## 2.4 Instrument Preparation

Incubation experiments in Figures 2.13, 2.14 have apparent deficiencies because the number of data points collected during the time course of the  $\text{Co}^{\text{II}}$ -substrate radical formation, especially along the rising curve, is usually less than 10. This limitation is imposed by the experimental design, in which a sample will experience slow warming (about 40 seconds) → incubation → cooling (about 15 seconds) → EPR detection cycle.

Since the kinetic data is retrieved from the data fitting of the kinetic curve, it is important to design an experimental method that can offer more data points along the reaction time course, and provide an improved environment for EAL, in which the data

collection will not perturb the enzyme's reaction. To meet with these experimental expectations, a novel time-resolved, full spectrum continuous wave electron paramagnetic resonance spectroscopy is employed to investigate the EAL catalysis. The following paragraphs will cover the instrument preparation for this technique.

#### **2.4.1 Capillary Tube Packaging**

The presence of a large volume of liquid sample in EPR resonator significantly increases the energy loss of the microwaves and thereby reduces the cavity quality factor (Q) to such a low value that the tuning of the microwave bridge is not practical. The simple way to solve this problem is to reduce the volume of the sample by packaging the sample in a capillary (less than 1.5 mm inner diameter) tube. A low temperature protocol is correspondingly developed to seal the EAL·B<sub>12</sub>·substrate ternary complex in 41% DMSO/water cryosolvent into a 2 mm O.D. capillary tube (Wilmad/Lab Glass, part number 712-SQ-250 M) at 230 K. This capillary package is robust enough to survive in a temperature jump by 70 K interval. The text description of the protocol is enclosed in the Appendix.

#### **2.4.2 Instrument Setup**

X-band time-resolved cw-EPR experiments are carried out on a Bruker ELEXSYS E500 EPR spectrometer with an ER 4123SHQE X-band cavity resonator. The temperature is controlled by a Bruker ER 4131VT system.

Since the sample is in liquid phase, a homogeneous temperature is demanded over the length of the whole sample ( $\approx 4.0$  cm). The cooling system is reconstructed in such a way that a 1 m N<sub>2</sub> cold gas transfer line is ordered and a 15 cm heating coil is installed at the rear end of the transfer line, which is roughly 60 cm away from the EPR resonator.

The temperature gradient inside the sample in this cryostat/controller system is measured by translating an ultra-thin T-band thermocouple probe along the EPR tube axis to achieve different heights within a solution sample. The result is  $\pm 0.2$  K over the length of the EPR sample cavity. The temperature readout in the Bruker ELEXSYS E500 spectrometer is calibrated by an Oxford Instruments ITC503 temperature controller with a calibrated model 19180 4-wire RTD probe, which has  $\pm 0.3$  K accuracy in the 230 K to 273 K region. ON the basis of above results, the total temperature uncertainty (including temperature gradient and instrumental uncertainty) of the EPR measurements is thus estimated to be  $\pm 0.4$  K.

The PID parameters, heater power and N<sub>2</sub> gas flow rate of the Bruker ER 4131VT temperature control are also carefully adjusted to minimize the following factors: (1) the rising time of the temperature from 230 K to the desired higher temperature; (2) The overshoot of during the temperature rising; (3) the temperature settling time.

After the adjustments, a set of parameters are selected, which guarantee that the temperature rising and settling process from 230 K to a higher temperature point (less than 250 K) takes less than 10 s with a small overshoot  $\leq 1.5$  K. Considering the microwave bridge auto-calibration (“auto-tune” mode) at the high temperature set point ( $\approx 10$  s), the total dead time of the instrument is  $\leq 20$  seconds.

### **2.4.3 Concluding Remarks**

With the accomplishments of the biological sample preparation and the instrument adjustment, we are ready to embark on the investigation of EAL catalysis at subzero temperatures.

**Chapter Three**

**Kinetic and Thermodynamic**

**Studies of Co<sup>II</sup>-substrate**

**Radical Pair in Cryosolvent**

**System**

The cryoenzymology method has been chosen as the primary experimental approach to study the catalytic intermediates and corresponding inter-conversion rates for Co-C bond cleavage in coenzyme B<sub>12</sub>-dependent ethanolamine ammonia-lyase from *Salmonella typhimurium*. The potassium cacodylate buffered 41% v/v DMSO/water cryosolvent provides a solution to allow mixing of EAL holoenzyme and substrate, (S)-2-aminopropanol, at 230 K in an environment that mimics the aqueous solution. Temperature step from 230 K to 234-250 K initiates the EAL's catalytic activity. The only EPR-active intermediate state, subsequently accumulated following the temperature step, has been confirmed to be the Co<sup>II</sup>-substrate radical pair state by multiple EPR spectroscopic methods. Higher temperature decay experiments at 270 K demonstrate that the population of the Co<sup>II</sup>-substrate radical pair state will reach an equilibrium with the ternary complex in the temperature range of 234 -250 K, due to the extremely slow reaction rate (at least 10<sup>2</sup> fold slower than the Co<sup>II</sup>-substrate radical pair formation rate) on the substrate radical rearrangement step.

In this chapter, we will employ a novel EPR spectroscopy method, which is time-resolved, full-spectrum continuous-wave EPR spectroscopy, to further explore the radical pair formation process after the temperature step. Reaction initiation in this system has significantly shorten deadtime (20 s) than previous manual mixing methods (2-3 for incubation → cryoquench → data collection). Another advantage of this novel EPR method is that it does not perturb or interrupt the EAL catalytic activity, which allows continuous acquisition of spectra during progress of the reaction.

### **3.1 Temperature Dependence of Substrate Radical Pair Formation**

The time-resolved, full-spectrum continuous-wave EPR spectroscopy will show its first application in the study of the temperature dependence of the  $\text{Co}^{\text{II}}$ -substrate radical pair formation reaction. The goal of this study is to determine the kinetic mechanism, especially the rate limiting step, by measuring the reaction rate and converting to the Arrhenius plot over a certain subzero temperature range. The results will also provide critical information in the reaction model setup in order to extract microscopic rates and corresponding thermodynamic parameters.

#### **3.1.1 Time-resolved, Full Spectrum Continuous Wave Electron Paramagnetic Resonance**

A 2-D EPR experiment is set up via a user interface program *Xepr* on a Linux workstation, which controls a Bruker ELEXSYS E500 EPR spectrometer, by setting both Time and Field as separate axis in the Experiment Setup Dialog. One Bruker Super High QE (SHQE) cavity (model number 4123SHQE) is employed as the resonator, which provides a high Q (unloaded  $Q_u > 25000$ ) with a large filling factor. The cavity can be autotuned through the *Xepr* program.

The low temperature is achieved by a Bruker ER 4131VT, which is a digital temperature control system. It provides an accessible temperature range above 100 K by using liquid nitrogen as coolant. The whole system consists of (1) quartz dewar; (2) ER 169DIS dewar insert holder; (3) digital temperature and gas flow control unit; (4) PTD temperature probe; (5) custom-made 1 m transfer line; (6) liquid nitrogen storage dewar;

(7) nitrogen evaporator heater assembly; (8) cavity purge gas unit. The target temperature is reached and stabilized via PID temperature control (proportional, integral and derivative) and the temperature reading via a PTD temperature probe, which is placed close to the sample's position. The ER 4131VT unit is fully remotely accessible via the *Xepr* interface.

The temperature control system is carefully tuned to optimize the performance for the temperature step from 230 K to 234 – 248 K. The final performance of the whole system achieves the following: (1) less than 20 s dead time, which includes the temperature increase and equilibrating process ( $\leq 10$  s), plus the microwave bridge auto-calibration (“auto-tune” mode) time at the high temperature set point ( $\approx 10$  s); (2)  $\pm 0.4$  K temperature error, which is estimated through the method described in the previous chapter.

By following the capillary sample preparation protocol in the Appendix, a 50  $\mu$ l volume of substrate-bound holoenzyme is sealed into a 2 mm outer diameter capillary tube and placed into the cavity at 230 K with the protection of pre-cooled isopentane. The enzyme reaction is then triggered by a temperature step and monitored through the EPR hardware.

### **3.1.2 Time-dependence of Co<sup>II</sup>-substrate Radical Pair Formation**

The EAL·B<sub>12</sub>-substrate mixture prepared at 230 K reacts to form the Co<sup>II</sup>-substrate radical pair state following a temperature step to higher temperatures. The rise of the Co<sup>II</sup>-substrate radical pair EPR signal is measured by the continuous acquisition of the Co<sup>II</sup>-radical pair spectrum. In order to achieve shorter sweep times, only the substrate radical portion of the lineshape is acquired. Figure 3.1 shows a representative data set that

is acquired at  $T=242$  K. The peak-to-trough amplitude of the substrate radical signal in Figure 3.1 is plotted as a function of time in Figure 3.2. Note that the data in Figure 3.2 are truncated at  $3.90 \times 10^3$  s, relative to the full time scale of  $6.43 \times 10^3$  s presented in Figure 3.1, in order to more clearly display the rise phase of the data. The curve in Figure 3.2 is well-fit by using a single exponential growth function, as follows:

$$A_{pt}(t) = A_{pt}(\infty)[1 - e^{-k_{obs}t}] \quad (3.1)$$

where  $A_{pt}(t)$  and  $A_{pt}(\infty)$  are the time-dependent amplitude and equilibrium amplitude, respectively, measured from the lowest field peak to the highest field trough of the substrate radical EPR signal, and  $k_{obs}$  is the observed first-order rate constant for the growth of the substrate radical EPR signal. The curve fitting is performed by using the program OriginPro 7.5 (OriginLab Corporation, Northampton, MA), with the least-squares fitting method.

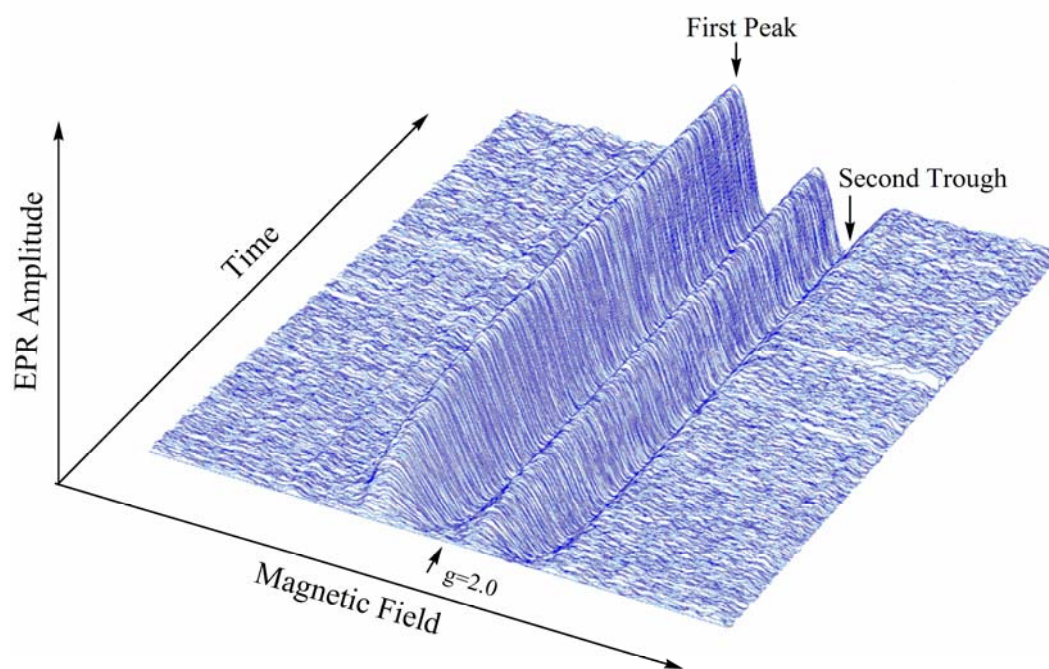


Figure 3.1: Time-dependence of the EPR spectrum of the substrate radical pair state in EAL in the cryosolvent system at  $T=242$  K, following temperature-step initiation of reaction. The time interval between each single-sweep spectrum is 15 s. The free electron resonance position at  $g=2.0$  is shown by the arrow. The first peak and second trough are positioned at 3284 and 3415 Gauss, respectively. The full extents of the magnetic field sweep and time course are 560 Gauss and  $6.43 \times 10^3$  s, respectively. The concentrations of EAL active sites and coenzyme  $B_{12}$  are 150  $\mu\text{M}$  and 15 mM, respectively. *EPR Conditions:* microwave frequency, 9.365 GHz; microwave power, 10 dB (20 mW); magnetic field modulation, 12 Gauss; modulation frequency, 100 kHz; scan rate: 53 Gauss  $\text{s}^{-1}$ ; time constant, 164 ms. The  $t=0$  spectrum (baseline) has been subtracted from each spectrum.

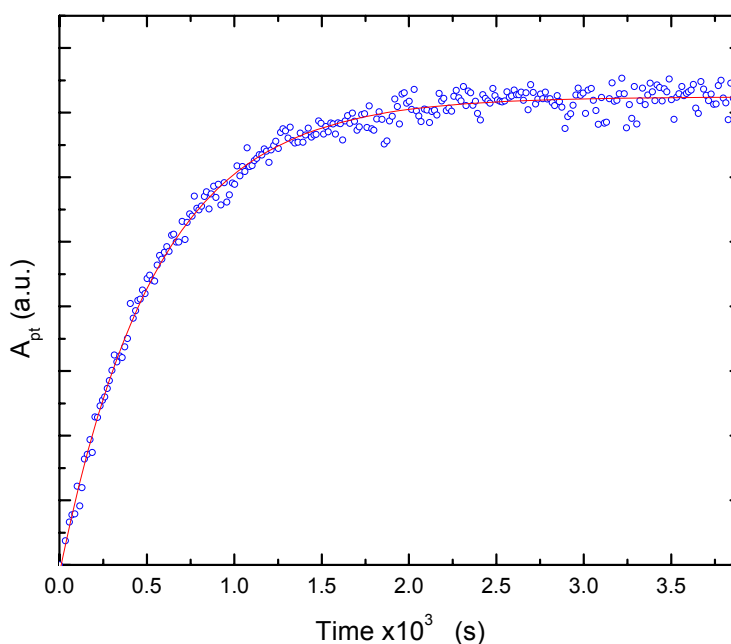


Figure 3.2: Time-dependence of the EPR amplitude of the substrate radical pair state in EAL in the cryosolvent system at  $T=242$  K, following temperature-jump initiation of reaction. The amplitude is given by the difference between the first peak (3284 Gauss) and second trough (3415 Gauss) amplitudes, as defined in Figure 3.1. Note that the data are truncated at  $3.90 \times 10^3$  s, relative to the full time scale of  $6.43 \times 10^3$  s presented in Figure 3.1. The experimental data points are overlaid with the best-fit exponential growth function (solid curve;  $k_{\text{obs}} = 1.82 \times 10^{-3} \text{ s}^{-1}$ ). EPR conditions are as described in legend to Figure 3.1.

### 3.1.3 Temperature-dependence of $\text{Co}^{\text{II}}$ -substrate Radical Pair Formation between 234 – 248 K

The choice of the temperature point, at which the time-resolved, full-spectrum continuous-wave EPR spectroscopy is applied on the reaction of  $\text{Co}^{\text{II}}$ -substrate radical

pair formation, is confined by the following limitations: (1) At  $T > 248$  K,  $\tau_{\text{obs}} < 10^2$  s, which is comparable to or less than the instrument deadtime of  $2.0 \times 10^1$  s, and the reaction cannot be monitored by the full spectrum acquisition; (2) At  $T < 234$  K, the absolute amplitude of  $A_{\text{pt}}$  after equilibrium is so small that a poor *SNR*, especially during early time points, limits certainty in the data; (3) The temperature uncertainty of the system is  $\pm 0.4$  K. With all these considerations, 234 K, 236 K, 238 K, 240 K, 242 K, 244 K, 246 K and 248 K are selected as the data collecting temperatures. Similar to the data shown in Figure 3.2 at 242 K, the growth of the EPR signal at all temperatures within 234 – 248 K is well-fit by the single exponential function in Eq. 3.1. The curve fittings are all performed by using the program OriginPro 7.5 (OriginLab Corporation, Northampton, MA), with the least-squares fitting method.

Figure 3.3 shows the natural logarithm of  $k_{\text{obs}}$  plotted as a function of inverse absolute temperature, in the Arrhenius plot form. The average values of  $k_{\text{obs}}$  for the different temperatures, and standard deviations that represent at least three separate determinations, are collected in Table 3.1. The Arrhenius plot is linear, which suggests that the kinetic mechanism and the rate limiting step for  $\text{Co}^{\text{II}}$ -substrate radical pair formation are maintained over the temperature range of 234-248 K. As shown below,  $k_{\text{obs}}$  is a function of at least four microscopic rate constants, and therefore, cannot be used directly to extract  $A$  and  $E_a$  parameters (or  $\Delta G^\ddagger$ ,  $\Delta H^\ddagger$ , and  $\Delta S^\ddagger$  parameters) that correspond to a single first-order rate constant.

The linear dependence of  $\ln k_{\text{obs}}$  on inverse absolute temperature that is shown in Figure 3.3 can be extrapolated to obtain an estimated value for  $k_{\text{obs}}$  at 298 K of  $54 \text{ s}^{-1}$ . This value is in good agreement with the value of  $74 \text{ s}^{-1}$  reported for the rate constant for

the appearance of cob(II)alamin in the reaction of holo-EAL with (*S*)-2-aminopropanol by using stopped-flow mixing and visible absorption detection.<sup>18</sup> This is evidence that the kinetics results obtained at low temperature in the cryosolvent system represent the native enzyme function.

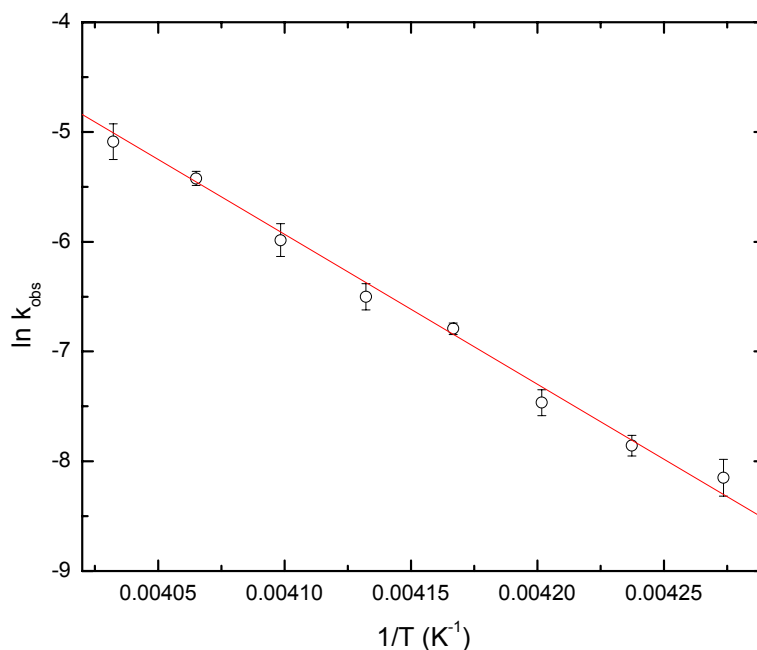


Figure 3.3. Dependence of the natural logarithm of the observed first-order rate constant for growth of the substrate radical EPR signal on the inverse absolute temperature from  $T=234$ - $248$  K. The substrate:active sites ratio was 100, and the concentration of active sites was  $150 \mu\text{M}$ . The error bars represent the standard deviation obtained by combining three separate measurements at each temperature, which used EAL from three different preparations. Best linear fit (solid line) parameters: slope= $-1.37 \times 10^4$ , ordinate intercept= $5.00 \times 10^1$ ,  $R^2=0.993$ .

Table 3.1. Values of the observed rate constant for  $\text{Co}^{\text{II}}$ -substrate radical pair formation at different absolute temperatures. Values represent the average of at least three separate experiments, and the corresponding standard deviation.

$T$ (K)	$k_{\text{obs}} (\times 10^{-3} \text{ s}^{-1})$	
<b>234</b>	0.29	$\pm 0.06$
<b>236</b>	0.39	$\pm 0.04$
<b>238</b>	0.58	$\pm 0.08$

<b>240</b>	1.12	±0.07
<b>242</b>	1.5	±0.2
<b>244</b>	2.5	±0.5
<b>246</b>	4.4	±0.3
<b>248</b>	6.2	±0.9

### 3.1.4 Attempted Detection of Paramagnetic Intermediate States

The presence of any possible paramagnetic intermediate states other than the  $\text{Co}^{\text{II}}$ -substrate radical pair, in particular, the  $\text{Co}^{\text{II}}$ -5'-deoxyadenosyl radical pair, is addressed by analyzing the spectra from time-resolved, full-spectrum continuous-wave electron paramagnetic resonance spectroscopy at 234-248 K. Figure 3.4 shows normalized EPR spectra for  $T=242$  K that represent the average of blocks (sets) of spectra that are obtained at the midpoint of the rise of the  $\text{Co}^{\text{II}}$ -substrate radical pair signal (Figure 3.4A), and in the equilibrium state following the rise (Figure 3.4B). The block averaging improves the *SNR* of individual spectra obtained from the small volume, 2 mm outer diameter capillary tubes used in the liquid state experiments. The two spectra in Figure 3.4 are identical, and they do not differ significantly from  $\text{Co}^{\text{II}}$ -substrate radical pair spectrum shown in Figure 2.11. The results presented in Figure 3.4, and those of similar experiments performed at different temperatures over the range of 234-248 K, show that no paramagnetic species, other than the  $\text{Co}^{\text{II}}$ -substrate radical pair, are detectable in spectra obtained under pre-equilibrium or equilibrium conditions in the cryosolvent system at  $\text{SNR} \leq 50$ .

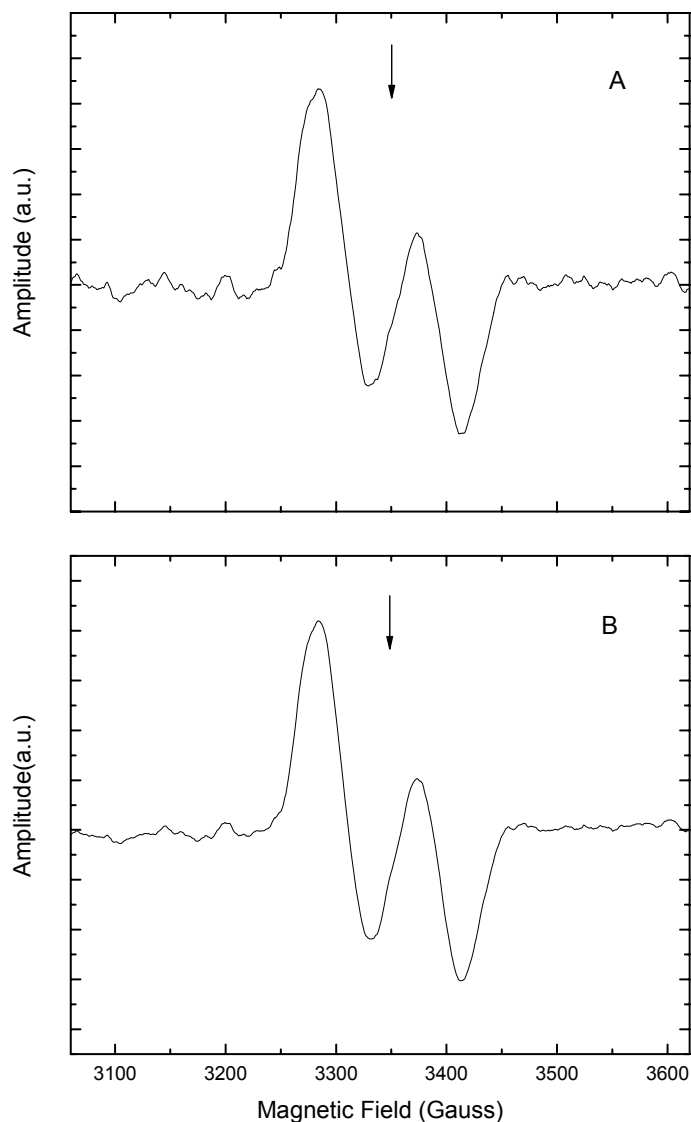


Figure 3.4: Block-averaged EPR spectra of the substrate radical obtained during reaction at  $T=242$  K. The free electron resonance position at  $g=2.0$  is shown by the arrow. (A) Spectrum representing the midpoint of the rise of the substrate radical EPR signal, obtained over 40-80% of the final amplitude (18 spectra averaged). (B) Spectrum representing the equilibrium state (constant amplitude) of the substrate radical EPR signal (100 spectra averaged). The substrate and EAL active site concentrations were  $150 \mu\text{M}$  and  $15 \text{ mM}$ , respectively. *EPR conditions*: microwave frequency,  $9.365 \text{ GHz}$ ; microwave power,  $10 \text{ dB}$  ( $20 \text{ mW}$ ); magnetic field modulation,  $12 \text{ Gauss}$  peak-peak; modulation frequency,  $100 \text{ kHz}$ ; field sweep rate,  $53 \text{ Gauss s}^{-1}$ ; time constant,  $164 \text{ ms}$ .

### 3.1.5 Concluding Remarks

Time-resolved, full-spectrum continuous-wave electron paramagnetic resonance spectroscopy significantly enhances the time resolution in the study of  $\text{Co}^{\text{II}}$ -substrate radical pair formation at subzero temperature range. The detection deadtime:  $\tau_{\text{obs}}$  ratio in the experiment within 234 – 248 K is less than 20 s:  $160 \text{ s} = 0.125$ , which is two orders-of-magnitude less than the corresponding value from millisecond rapid mixing experiments at ambient temperatures.

The experimental result on temperature-dependence of  $k_{\text{obs}}$ , which is plotted by using the Arrhenius form in Figure 3.3, delivers an important message that the rate limiting step for  $\text{Co}^{\text{II}}$ -substrate radical pair formation is maintained over the temperature range of 234-248 K. This information ensures that the later three-state, two-step model can be applied to describe the reaction of  $\text{Co}^{\text{II}}$ -substrate radical pair formation within this subzero temperature range.

We also obtain an estimated value for  $k_{\text{obs}}$  at 298 K of  $54 \text{ s}^{-1}$  from data extrapolation. This value is consistent with the value of  $74 \text{ s}^{-1}$ , obtained by using stopped-flow mixing and visible absorption detection from independent research groups.<sup>17,18</sup> This result demonstrates that the kinetics results obtained at low temperature in the cryosolvent system represent the native enzyme function.

Figure 3.4 shows no tracing of  $\text{Co}^{\text{II}}$ -5'-deoxyadenosyl radical pair signal. It implies that this intermediate state has a much higher energy profile than the  $\text{Co}^{\text{II}}$ -substrate radical pair state, which is consistent with the high resolution 6 K EPR studies.

### **3.2 Kinetic Evidence for the Formation of Ternary Complex**

Though the high resolution EPR spectrum at 6 K, performed on the sample after mixing of EAL holoenzyme and substrate, comprises neither the  $\text{Co}^{\text{II}}$ -substrate radical pair nor the  $\text{Co}^{\text{II}}$ -5'-deoxyadenosyl radical pair and suggests the kinetic arrest of the  $\text{EAL}\cdot\text{B}_{12}$ -substrate ternary complex, the direct proof of substrate binding in the EAL active site is still lacking. Time-resolved, full-spectrum continuous-wave electron paramagnetic resonance spectroscopy provides us another experimental approach to investigate the existence of this  $\text{EAL}\cdot\text{B}_{12}$ -substrate ternary complex by following a similar experimental procedure as for the temperature dependence studies on the  $\text{Co}^{\text{II}}$ -substrate radical pair formation. The variation is changing the axis from temperature to substrate concentration.

### 3.2.1 Substrate Concentration Variation Experiment

To study the substrate concentration dependence on the formation rate ( $k_{obs}$ ) of the  $\text{Co}^{\text{II}}$ -substrate radical pair, the substrate:active site ratio is varied over a large range, from 1.0 to 100. The same experiments have been completed on two temperature points at 240 and 246 K.

Figure 3.5 shows that  $k_{obs}$  is independent of substrate concentration at both 240 and 246 K. Figure 3.6 shows that the concentration of  $\text{Co}^{\text{II}}$ -substrate radical pair formed at the substrate:active site ratios in Figure 3.5 is constant, to within  $\pm 15\%$ .

To explore the binding affinity of the substrate with holoenzyme from these results at 230 K, a reaction scheme (Scheme 3.1) has been employed to describe the equilibrium between enzyme ( $E$ ) and substrate ( $S$ ). The equilibrium is characterized by the dissociation constant,  $K_D = \frac{[E][S]}{[ES]}$ , where  $[E]$  and  $[S]$  represent the free concentrations of enzyme and substrate, and  $[ES]$  is the concentration of enzyme-substrate complex. The

free concentrations are related to the total concentrations of enzyme and substrate as

$$[E] = [E_{tot}] - [ES] \text{ and } [S] = [S_{tot}] - [ES].$$

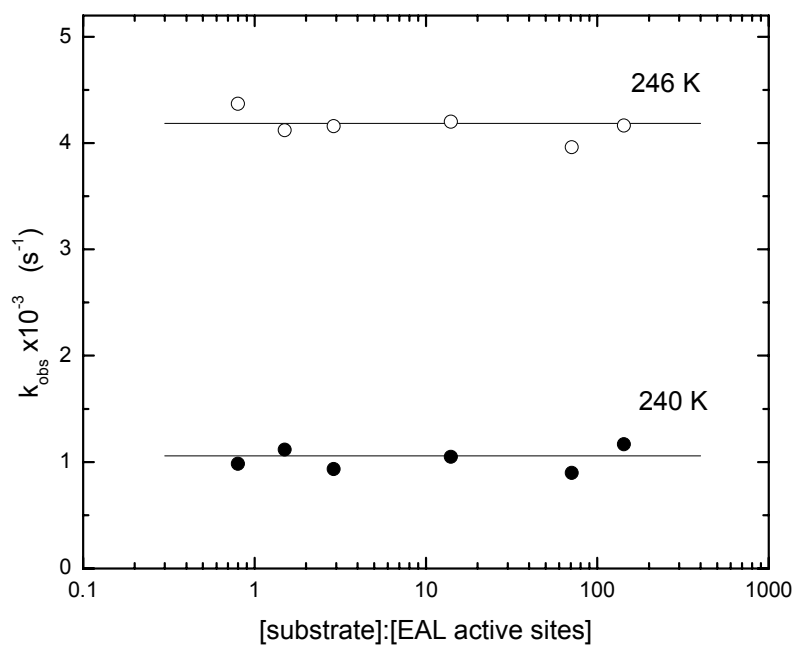


Figure 3.5. Dependence of the observed first-order rate constant for the growth of the substrate radical pair EPR signal,  $k_{obs}$ , on the substrate:active sites ratio at  $T=240$  and  $246$  K in the cryosolvent system. The lines represent the best zero-slope linear fit to the data. The concentration of EAL active sites is  $150 \mu\text{M}$ .

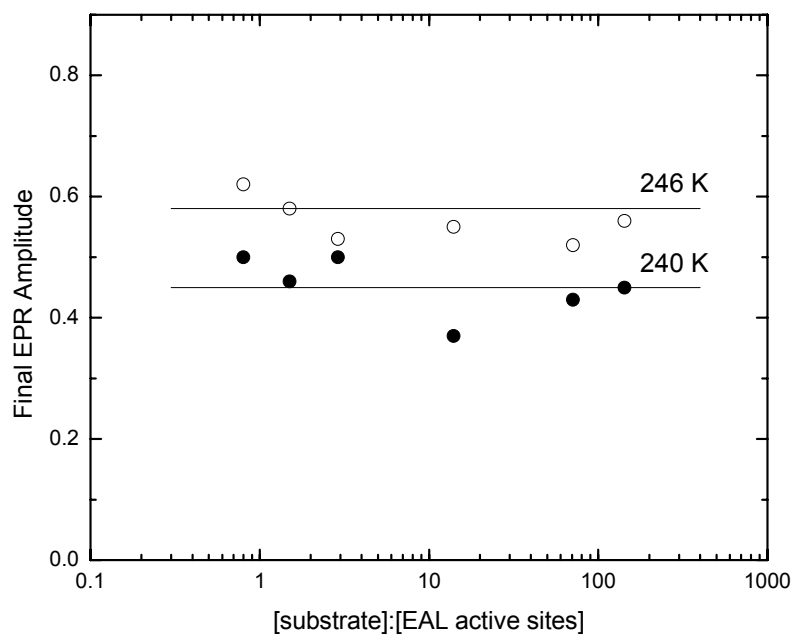
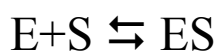


Figure 3.6: Dependence of the normalized constant (long-time) amplitude of the substrate radical EPR signal on the substrate:active sites ratio at  $T=240$  and  $246$  K in the cryosolvent system. The amplitude is normalized as described in the text. The lines represent the best zero-slope linear fit to the data. The concentration of EAL active sites is  $150 \mu\text{M}$ .

Substitution of these expressions for  $[E]$  and  $[S]$  into the expression for  $K_D$  and rearranging the variables lead to the expression for the concentration of the enzyme-substrate complex given by Eq. 3.2. Eq. 3.2 possesses the quadratic form of the expression for  $[ES]$ , which is appropriate only when the  $K_D \leq [E_{tot}]$  condition is met. The positive root of Eq. 3.2 gives the physically plausible result. Eq. 3.2 is used to calculate the normalized enzyme-substrate complex populations,  $[ES]/[E_{tot}]$  as a function of  $[S]$  for three different  $K_D$  values. The calculated values are presented in Table 3.2.



Scheme 3.1

$$[ES] = \frac{1}{2} \{ ([S_{tot}] + [E_{tot}] + K_D) \pm \sqrt{([S_{tot}] + [E_{tot}] + K_D)^2 - 4[S_{tot}][E_{tot}]} \} \quad (3.2)$$

Table 3.2: Calculated values of the normalized enzyme-substrate complex concentration at different substrate:active site ratios, for three  $K_D$  values. The  $[E_{tot}] = 150 \mu\text{M}$ .

		$K_D=117 \mu\text{M}$	$K_D=10 \mu\text{M}$	$K_D=1.0 \mu\text{M}$
$[S_{tot}] (\mu\text{M})$	$[S_{tot}]/[E_{tot}]$	$[ES]/[E_{tot}]$	$[ES]/[E_{tot}]$	$[ES]/[E_{tot}]$
150	1	0.42	0.77	0.92
300	2	0.64	0.94	0.99
1500	10	0.92	0.99	0.99
7500	50	0.98	0.99	0.99
15000	100	0.99	0.99	0.99

Comparing with the experimental results in Figure 3.6, an upper limit on  $K_D$  is obtained as  $10 \mu\text{M}$  within the subzero temperature range. For buffered aqueous solution at  $298$  K,  $K_D=117 \pm 6 \mu\text{M}$  for binding of (S)-2-aminopropanol to apo-EAL has been

obtained (L. E. Anderson and K. Warncke, unpublished). The reported  $K_M$  values of 15.5  $\mu\text{M}$  for *Clostridium SP*<sup>40</sup> and 0.80  $\mu\text{M}$  for *S. typhimurium*<sup>49</sup> also suggest a relatively high affinity of (S)-2-aminopropanol for EAL at room temperature in aqueous solution.

The significantly lowered temperature in the cryosolvent system would, in principle, decrease the solubility of the positively-charged ammonium form of the substrate, and decrease the translational entropy contribution to the reactant solution free energy. Both effects would promote tighter binding of substrate to enzyme.

### 3.2.2 Concluding Remarks

Figures 3.5 and 3.6 provide evidence that the formation of the  $\text{Co}^{\text{II}}$ -substrate radical pair state proceeds from an initial state that is the EAL·B<sub>12</sub>·substrate ternary complex. We propose, on the basis of these results, that the mixing of holoenzyme and substrate at 230 K leads to the formation of the ternary complex, and that this state reacts directly to form the  $\text{Co}^{\text{II}}$ -substrate radical pair when the temperature is stepped to higher values.

## 3.3 Three-state, Two-step Reaction Model

For the  $\text{Co}^{\text{II}}$ -substrate radical pair formation reaction after a temperature step from 230 K to 234 – 248 K, we have obtained the following experimental facts:

- (1) A: The initial state is the ternary complex of EAL holoenzyme and substrate radical. Results from high resolution 6 K EPR, EPR half-field transition investigation and parallel mode EPR provide evidence that this state does not contain free radical. It implies that the Co-C bond cleavage has not occurred.

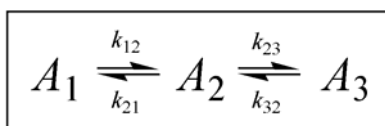
B: Concentration variation studies from time-resolved, full spectrum, continuous wave EPR offers an upper limit on  $K_D$  as an order-of-magnitude less than the EAL active sites concentration. This demonstrates that the substrate tightly binds holoenzyme after the low temperature mixing. Based on experimental facts (1A) and (1B), the initial state is confirmed to be the EAL·B<sub>12</sub>·substrate ternary complex before the Co-C bond cleavage in the temperature step experiment.

- (2) The 250 K decay experiment and the  $A_{pt}$  time course from time-resolved, full spectrum continuous wave EPR demonstrate that a population of paramagnetic centers are accumulated to an equilibrium state after the temperature step from 230 K to 234 - 248 K. The decay rate of these paramagnetic states is  $\sim 10^2$ -fold less than  $k_{obs}$  over the temperature range, which is 234-248 K. This demonstrates that the final state of the reaction in the temperature step experiments is a stable equilibrium state.
- (3) The EPR line shape simulation based on high resolution 6 K EPR proves that the paramagnetic centers detected after the temperature step are the Co<sup>II</sup>-substrate radical pair.
- (4) Results from high resolution 6 K EPR, half-field transition, parallel mode EPR and block average of time-resolved, full spectrum continuous wave EPR spectra yield that only the Co<sup>II</sup>-substrate radical pair is accumulated to a concentration level that is high enough to be detected by EPR at  $SNR = 1300$  after the temperature step. A population upper limit is thereby imposed on the Co<sup>II</sup>-5'-deoxyadenosyl radical pair.

These results have unraveled substantial information about the initial, intermediate and final states formed during the temperature step experiments. A kinetic model will be built upon this information in order to explore the relations among experimental observables and microscopic rate constants.

### 3.3.1 Kinetic Model Setup

Scheme 2 depicts a linear two-step, three-state kinetic mechanism that we propose for the observed reaction of the EAL·B<sub>12</sub>·substrate ternary complex to form the Co<sup>II</sup>-substrate radical pair within 234 – 248 K. The mechanism corresponds to steps 1 and 2 in the catalytic cycle presented in Figure 1.2. The states,  $A_1$ ,  $A_2$  and  $A_3$ , in Scheme 3.2 represent, in compact notation, the ternary complex, the Co<sup>II</sup>-5'-deoxyadenosyl radical pair, and the Co<sup>II</sup>-substrate radical pair, respectively. The identification of  $A_1$  and  $A_3$  is from results summary (1) and (3) separately. A third step, which represents the conversion of substrate radical to product radical (step 3 in Figure 1.2) is not included in the mechanism, because of the results summary (2). Results summary (4) will serve as a constraint on the microscopic rates to meet the condition that the  $A_2$  concentration stays low.



Scheme 3.2

The coupled differential equations that describe the time dependence of the states in the linear two-step model presented in Scheme 3.2 can be solved to give analytical expressions for the normalized amplitudes of the states  $A_i$  and the relaxation rate parameters  $\lambda_i$ , for the initial state (at  $t=0$ ),  $\frac{[A_1]_0}{[A_1]_0} = 1$ ,  $\frac{[A_2]_0}{[A_1]_0} = \frac{[A_3]_0}{[A_1]_0} = 0$ ,<sup>99</sup> which are confirmed

by the experimental results as stated above. The following expressions give the time-dependence of the normalized amplitudes of the states  $A_i$ :<sup>99</sup>

$$\frac{[A_1]_t}{[A_1]_0} = \frac{k_{21}k_{32}}{\lambda_2\lambda_3} + \frac{k_{12}(\lambda_2 - k_{23} - k_{32})}{\lambda_2(\lambda_2 - \lambda_3)} e^{-\lambda_2 t} + \frac{k_{12}(k_{23} + k_{32} - \lambda_3)}{\lambda_3(\lambda_2 - \lambda_3)} e^{-\lambda_3 t} \quad (3.3)$$

$$\frac{[A_2]_t}{[A_1]_0} = \frac{k_{12}k_{32}}{\lambda_2\lambda_3} + \frac{k_{12}(k_{32} - \lambda_2)}{\lambda_2(\lambda_2 - \lambda_3)} e^{-\lambda_2 t} + \frac{k_{12}(\lambda_3 - k_{32})}{\lambda_3(\lambda_2 - \lambda_3)} e^{-\lambda_3 t} \quad (3.4)$$

$$\frac{[A_3]_t}{[A_1]_0} = \frac{k_{12}k_{23}}{\lambda_2\lambda_3} + \frac{k_{12}k_{23}}{\lambda_2(\lambda_2 - \lambda_3)} e^{-\lambda_2 t} - \frac{k_{12}k_{23}}{\lambda_3(\lambda_2 - \lambda_3)} e^{-\lambda_3 t} \quad (3.5)$$

The  $k_{ij}$  are defined in Scheme 3.2. The relaxation rate parameters,  $\lambda_i$ , are related to the microscopic rate constants by the following expressions:

$$\lambda_2 = \frac{1}{2} \{k_{12} + k_{21} + k_{23} + k_{32} + [(k_{12} + k_{21} + k_{23} + k_{32})^2 - 4(k_{12}k_{23} + k_{21}k_{32} + k_{12}k_{32})]^{\frac{1}{2}}\} \quad (3.6)$$

$$\lambda_3 = \frac{1}{2} \{k_{12} + k_{21} + k_{23} + k_{32} - [(k_{12} + k_{21} + k_{23} + k_{32})^2 - 4(k_{12}k_{23} + k_{21}k_{32} + k_{12}k_{32})]^{\frac{1}{2}}\} \quad (3.7)$$

and  $\lambda_1=0$ .<sup>99</sup>

Certain relations among the  $A_i$  are used in the analysis of the experimental data. The conservation condition is expressed in terms of the equilibrium ( $t \rightarrow \infty$ ) concentrations of the  $A_i$ , as follows:

$$[A_1]_0 = [A_1]_\infty + [A_2]_\infty + [A_3]_\infty \quad (3.8)$$

The concentration of the intermediate,  $A_2$ , relative to the experimentally observed state,  $A_3$ , at equilibrium is obtained from Eqs. 3.4 and 3.5 for the condition,  $t \rightarrow \infty$ , as follows:

$$\frac{[A_2]_{\infty}}{[A_3]_{\infty}} = \frac{k_{32}}{k_{23}} = K_{23}^{-1} \quad (3.9)$$

where  $K_{23}$  is the equilibrium constant for step 2 in Scheme 3.2. The relative concentration of  $A_1$  and  $A_3$  at equilibrium is obtained from Eqs. 3 and 5, as follows:

$$\frac{[A_3]_{\infty}}{[A_1]_{\infty}} = \frac{k_{12}k_{23}}{k_{21}k_{32}} = K_{12}K_{23} = K_{13} \quad (3.10)$$

where  $K_{12} = \frac{k_{12}}{k_{21}}$  is the equilibrium constant for step 1 in Scheme 3.2. The ratio of the concentration of the observed state at equilibrium,  $[A_3]_{\infty}$  to the total concentration of  $A_i$  states ( $[A_{tot}] = [A_1]_0$ , from Eq. 3.8) is denoted as  $v$ , and is given by Eq. 3.5 in the limit  $t \rightarrow \infty$ , as follows:

$$v = \frac{[A_3]_{\infty}}{[A_1]_0} = \frac{k_{12}k_{23}}{\lambda_2\lambda_3} \quad (3.11)$$

### 3.3.2 Temperature-dependence of the First-order Rate and Equilibrium Constants

The temperature dependence of the first order rate constant,  $k$ , is given by the Arrhenius expression:<sup>99</sup>

$$k(T) = A \exp\left(-\frac{\Delta G^{\ddagger}}{RT}\right) = A \exp\left(-\frac{\Delta H^{\ddagger} - T\Delta S^{\ddagger}}{RT}\right) \quad (3.12)$$

where  $\Delta G^{\ddagger}$ ,  $\Delta H^{\ddagger}$ ,  $\Delta S^{\ddagger}$  is the activation energy, enthalpy and entropy respectively.  $R$  is the gas constant, and  $A$  is a prefactor that represents the value of  $k$  as  $\Delta G^{\ddagger} \rightarrow 0$ . The value of

$A$  is typically approximated as  $\frac{k_B T}{h}$ , where  $k_B$  is Boltzmann's constant and  $h$  is Planck's constant.

The temperature dependence of the equilibrium constant,  $K$ , is described as follows:<sup>99</sup>

$$K(T) = \exp\left(-\frac{\Delta G}{RT}\right) = \exp\left(\frac{\Delta S}{R}\right) \exp\left(-\frac{\Delta H}{RT}\right) \quad (3.13)$$

where  $\Delta G$ ,  $\Delta H$ , and  $\Delta S$  are the equilibrium free energy, enthalpy and entropy, respectively. Eq. 3.13 is the basis for determining the  $\Delta H$  and  $\Delta S$  contributions to  $\Delta G$  by using the van't Hoff analysis.

### **3.4 Retrieving Thermodynamic Parameters for Co<sup>II</sup>-substrate Radical Pair Formation**

The goal of our experiment is to retrieve the microscopic rate constants from experimental observables  $k_{obs}$ , which is a first-order reaction rate retrieved from the time course of the time-resolved, full spectrum continuous wave EPR spectroscopy. The expression for  $k_{obs}$  only provides one equation, which is not enough to solve all the four unknown microscopic rates,  $k_{12}$ ,  $k_{21}$ ,  $k_{23}$ , and  $k_{32}$ . Inspired by Eq. 3.11, the experimental observable  $\nu$  will be utilized to provide another equation to relate the microscopic rates. The following paragraphs will be focusing on the experimental technique to obtain the  $\nu$  and the explanation of the results.

#### **3.4.1 Equilibrium Perturbation Experiments**

Through the temperature dependence studies on the final amplitude of the capillary samples in the temperature step experiments by using time-resolved, full spectrum continuous wave EPR, the  $\nu$  value is measured at different temperatures by normalizing the final equilibrium amplitude with an amplitude, which is measured after the capillary sample relaxes at high temperature ( $>270$  K) to convert all the active sites to substrate radical pair. However, the limited number of the paramagnetic centers in the capillary sample and the general temperature effect on the EPR amplitude reduce the accuracy on comparing concentration of the  $\text{Co}^{\text{II}}$ -substrate radical pair by measuring the EPR signal amplitude at different temperatures.

To increase the accuracy in the measurement of radical concentration, a 300  $\mu\text{l}$  sample in a 4 mm outer diameter EPR tube (6-fold larger volume relative to the capillary samples) with 100-fold excess of substrate compared to EAL active sites is used in the equilibrium perturbation experiments to increase the number of detected spins, i.e. increases the *SNR*. The EPR hardware used in this experiment is the same as described for the time-resolved, full spectrum continuous wave EPR experiments.

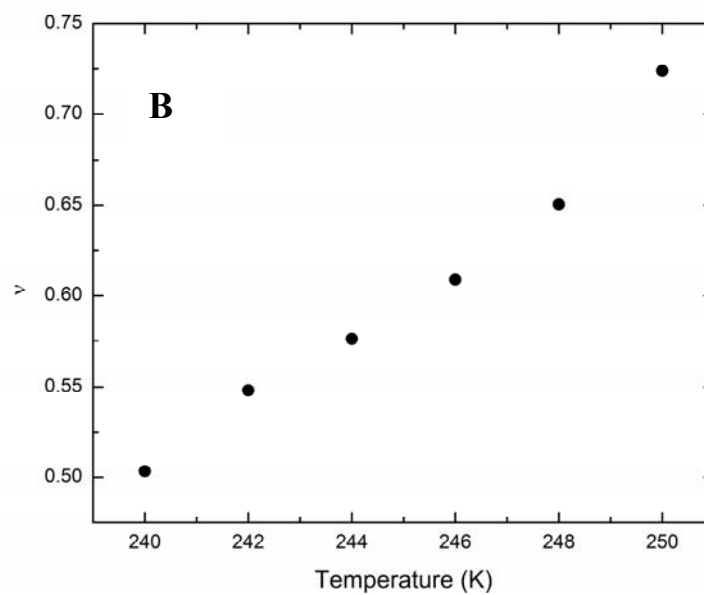
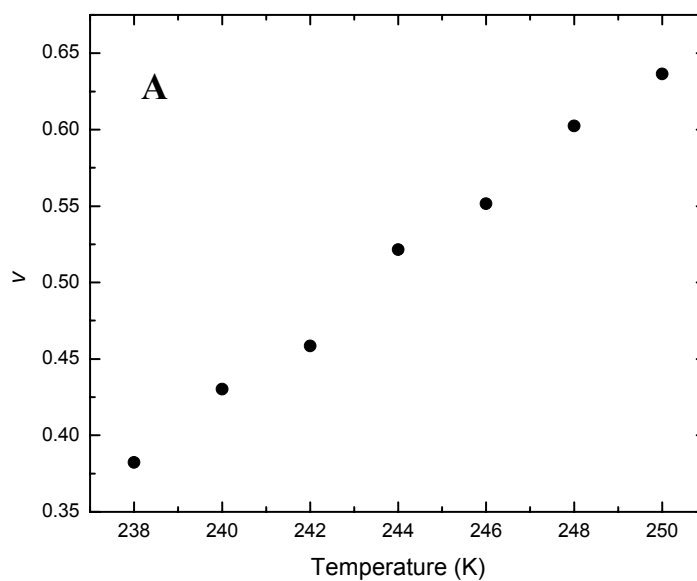
In a typical experiment, this ternary complex sample is initially adjusted to the incubation temperature,  $T_{\text{inc}}$ , in the ER 4123SHQE X-band resonator. The sample is then incubated to achieve a constant amplitude of the  $\text{Co}^{\text{II}}$ -substrate radical pair EPR signal. The incubation time period was generally  $>3\tau_{\text{obs}}$ , where  $\tau_{\text{obs}}$  is the characteristic reaction time at  $T_{\text{inc}}$ , as determined in the time-resolved experiments. The temperature of the sample is then quickly ( $< 15$  s) decreased to 120 K. The temperature transition time is significantly shorter than the equilibration time ( $15 \text{ s} \ll \tau_{\text{obs}}$ ). The EPR spectrum is then acquired at 120 K to retrieve the EPR signal amplitude for the substrate radical at the

equilibrium state, denoted as  $A_{pt}(\infty, T_{inc})$ . The EPR signal amplitude is measured as the difference in amplitude between the lowest field peak and highest field trough of the substrate radical lineshape. The point corresponding to the maximum or minimum amplitude is identified and averaged with the adjacent two points (five points total) to obtain the recorded amplitude. The sample temperature is then stepped to the next temperature incubation set point, and the incubation and measurement process is repeated. After finishing all desired incubation temperatures, the sample temperature is raised stepwise to 273 K, to avoid sudden  $pH$  change and dielectric shock, and held for 5 min. This leads to the formation of the  $Co^{II}$ -substrate radical pair in 100% of the functional EAL active sites, as found previously.<sup>17</sup> The fraction of EAL active sites occupied by the  $Co^{II}$ -substrate radical pair,  $v_i$ , was computed for each incubation temperature,  $T_i$ , by using the following expression:

$$v_i = \frac{A_{pt}(\infty, T_i)}{A_{pt}(\infty, T = 273 \text{ K})} \quad (3.14)$$

Figure 3.7A shows the normalized substrate radical amplitude,  $v$ , as a function of temperature (two additional data is presented in Figure 3.7B and 3.7C). The amplitude is normalized by using the amplitude of the substrate radical signal obtained after warming the sample to 273 K, followed by 5 min incubation at this temperature as explicitly defined in Eq. 3.14. In Figure 3.7A, the applied temperature perturbation sequence is not linear, in order to determine if the observed changes in the EPR amplitude of the  $Co^{II}$ -substrate radical pair are reversible. The sequence of temperature changes is as follows: 238→242, 242→240, 240→246, 246→244, 244→250, and 250→248 K. The linear

trend in Figure 3.7A indicates a reversible, temperature-dependent equilibrium between the ternary complex and the  $\text{Co}^{\text{II}}$ -substrate radical pair state. The value of  $\nu$  increases with increasing temperature from 0.37 to 0.64. Therefore, the ternary complex and the  $\text{Co}^{\text{II}}$ -substrate radical pair have comparable stabilities over the temperature range, with a trend towards a more stable  $\text{Co}^{\text{II}}$ -substrate radical pair state as temperature increases.



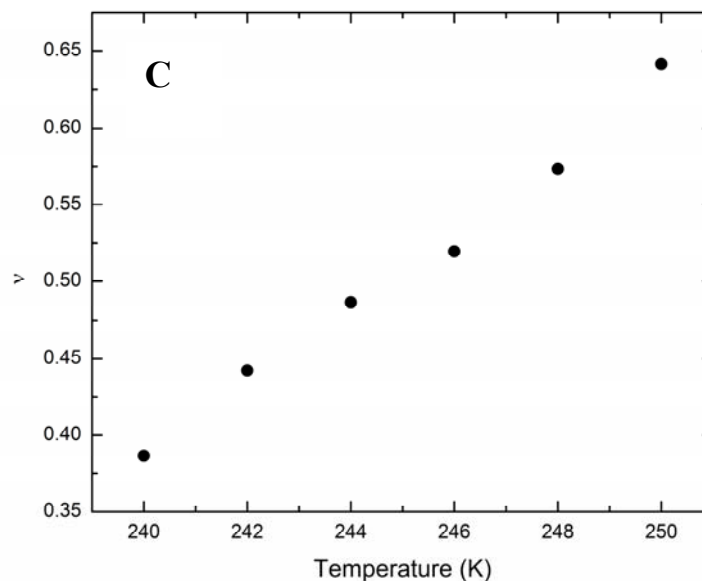


Figure 3.7: Normalized equilibrium saturation of the substrate radical EPR amplitude as a function of absolute temperature for three experiments A, B and C. The results for a single sample are shown, with the non-monotonic sequence of temperature values as described in the text. The EAL active site and substrate concentrations are 150  $\mu\text{M}$  and 15 mM, respectively.

### 3.4.2 Relations among Experimental Observables and Microscopic Rate

#### Constants

In the following paragraph, expressions will be mathematically derived from the mechanism in Scheme 3.2 to relate the experimental observables  $k_{obs}$  and  $\nu$  to the microscopic rates. The relations among the equilibrium constants that link the  $A_1$  strongly disfavor formation of the  $A_2$ . This accounts for the observed mono-exponential growth of the  $\text{Co}^{\text{II}}$ -substrate radical pair EPR signal.

The general linear two-step mechanism predicts a bi-exponential growth of  $A_3$  (the  $\text{Co}^{\text{II}}$ -substrate radical pair) as expressed by Eqs. 3.6 and 3.7 for the two relaxation constants,  $\lambda_2$  and  $\lambda_3$ .<sup>99</sup> Paramagnetic signals arising from an intermediate species,  $A_2$  (the  $\text{Co}^{\text{II}}$ -5'-deoxyadenosyl radical pair), are neither detected in the kinetic experiments at 234 - 248 K, nor in samples at equilibrium that are cryotrapped and examined by EPR

spectroscopy at 6 K (Figure 2.11). The highest  $SNR$  achieved is 1300. Therefore, if it is assumed that the  $Co^{II}$ -substrate radical pair and putative  $Co^{II}$ -5'-deoxyadenosyl radical pair EPR signals have comparable derivative amplitudes, then the  $SNR > 10^3$  leads to the inequality,  $\frac{[A_2]_\infty}{[A_3]_\infty} < 10^{-3}$ . This implies that  $K_{23} > 10^3$ . Further, the equilibrium perturbation

results presented in Figure 3.7 show that  $\nu \approx 0.5$  over the temperature range examined,

which implies that  $\frac{[A_3]_\infty}{[A_1]_0} \approx 0.5$  (Eq. 3.11). Substitution of the condition,

$[A_2]_\infty < 10^{-3}[A_3]_\infty$ , into Eq. 3.8 leads to the simplified expression,  $[A_1]_0 = [A_1]_\infty + [A_3]_\infty$ .

Substitution of this simplified expression into Eq. 3.11, and rearrangement, leads to the

approximation,  $\frac{[A_3]_\infty}{[A_1]_\infty} \approx 1$ , which holds over the temperature range examined. Substitution

of this result and  $K_{23} > 10^3$  (from above) into Eq. 3.10 leads to the inequality,  $K_{12} < 10^{-3}$ .

The limiting values obtained for  $K_{12}$  ( $= \frac{k_{12}}{k_{21}}$ ) and  $K_{23}$  ( $= \frac{k_{23}}{k_{32}}$ ) indicate that the following

inequalities hold for the corresponding pairs of rate constants:

$$k_{32} < 10^{-3} k_{23} \quad (3.15)$$

$$k_{12} < 10^{-3} k_{21} \quad (3.16)$$

The substitution of the limits from Eqs. 3.15 and 3.16 into Eqs. 3.6 and 3.7 leads to the following simplified approximate relations between  $\lambda_2$  and  $\lambda_3$  and the microscopic rate constants:

$$\lambda_2 = k_{21} + k_{23} \quad (3.17)$$

$$\lambda_3 = \frac{k_{12}k_{23} + k_{21}k_{32}}{k_{21} + k_{23}} \quad (3.18)$$

From the comparison of the right-hand sides of Eqs. 3.17 and 3.18 with the inequalities in Eqs. 3.15 and 3.16,  $\lambda_2 > 10^3 \lambda_3$ . The relaxation represented by  $\lambda_2$  will therefore not be detectable at our time resolution, and the growth of  $A_3$  (the state that corresponds to the EPR-detected  $\text{Co}^{\text{II}}$ -substrate radical pair) will be governed by an apparent mono-exponential process, which is in accord with experiment. The time-dependence of the growth of the normalized concentration of  $A_3$  is expressed as follows:

$$\frac{[A_3]_t}{[A_1]_0} \approx \frac{[A_3]_\infty}{[A_1]_0} (1 - e^{-\lambda_3 t}) \quad (3.19)$$

The parameters in Eq. 19,  $\frac{[A_3]_\infty}{[A_1]_0}$  and  $\lambda_3$ , are related to the experimental observables,  $k_{\text{obs}}$

and  $\nu$ , as follows:

$$k_{\text{obs}} = \lambda_3 = \frac{k_{12}k_{23} + k_{21}k_{32}}{k_{21} + k_{23}} \quad (3.20)$$

$$\nu = \frac{[A_3]_\infty}{[A_1]_0} = \frac{k_{12}k_{23}}{k_{12}k_{23} + k_{21}k_{32}} \quad (3.21)$$

The system is underdetermined, with respect to obtaining the values of the  $k_{ij}$ .

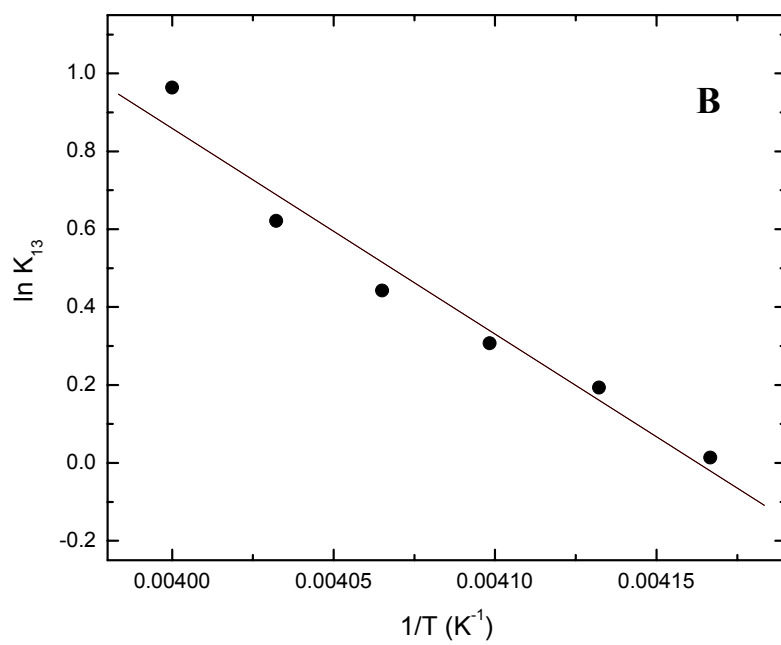
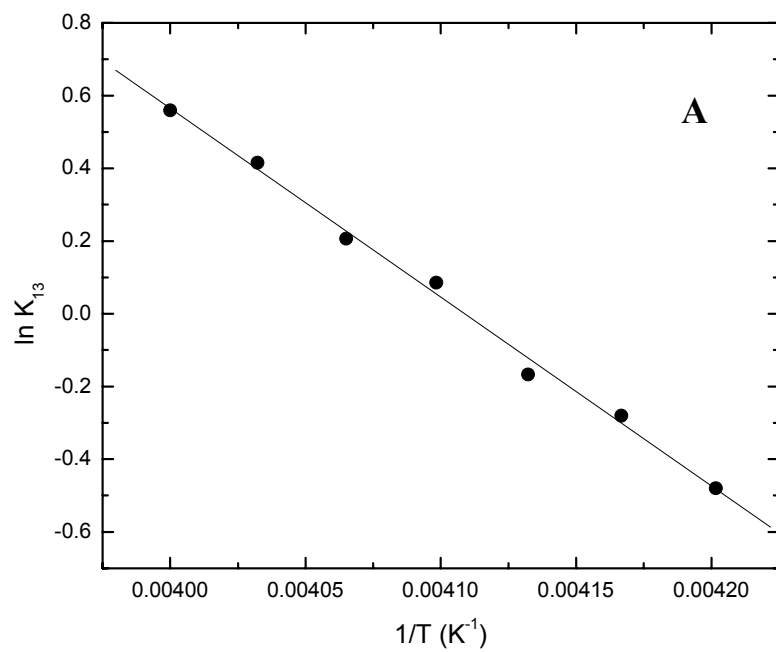
### 3.4.3 Thermodynamics of $\text{Co}^{\text{II}}$ -substrate Radical Pair Formation

The thermodynamic parameters,  $\Delta G_{13}$ ,  $\Delta H_{13}$ , and  $\Delta S_{13}$ , for the transition from the  $A_1$  (ternary complex) state to the  $A_3$  ( $\text{Co}^{\text{II}}$ -substrate radical pair) state are determined by van't Hoff analysis of  $K_{13}$  (Eq. 3.13). Values of  $K_{13}$  at different temperatures were obtained from the corresponding  $\nu$  values by using the following expression:

$$K_{13} = \frac{\nu}{1-\nu} \quad (3.22)$$

Eq. 3.22 is derived by dividing the numerator and denominator of the right-hand side of Eq. 3.21 by  $k_{21}k_{23}$ , expressing the resulting ratio of rate constants as  $K_{12}K_{23}=K_{13}$ , and rearranging to express  $K_{13}$  in terms of  $\nu$ . Figure 3.8 shows the van't Hoff plot for  $K_{13}$  that was obtained by using the  $\nu$  values presented in Figure 3.7. Table 3.3 presents values of  $\Delta H_{13}$  ( $10.8 \pm 0.8$  kcal/mol) and  $\Delta S_{13}$  ( $45 \pm 3$  cal/mol/K) that are obtained from the average of the linear fit parameters from each van't Hoff plot. Values of  $\Delta G_{13}$  are calculated from the Gibbs expression ( $\Delta G = \Delta H - T\Delta S$ ). The value of  $\Delta G_{13}$  is zero over the temperature range, to within the standard deviation of the measurements ( $+0.1 \pm 1.1$  kcal/mol at 238 K to  $-0.5 \pm 1.1$  kcal/mol at 250 K). The free energy contributions of the enthalpy and entropy ( $T\Delta S_{13} = -10.7$  to  $-11.3$  kcal/mol for 238 to 250 K, respectively) are nearly equal in magnitude.

Coenzyme B<sub>12</sub>-dependent RTPR also establishes an equivalent free energy at ambient temperature between the dGTP activator-bound enzyme and the first meta-stable  $\text{Co}^{\text{II}}$ -radical (thiyl) pair, in the absence of substrate.<sup>22</sup> However, in the substrate-bound condition in EAL, the relative stability of the  $\text{Co}^{\text{II}}$ -radical pair state increases with temperature, and the radical pair state becomes favored over the ternary complex at 298 K by  $-2.6$  kcal/mol, as described below.



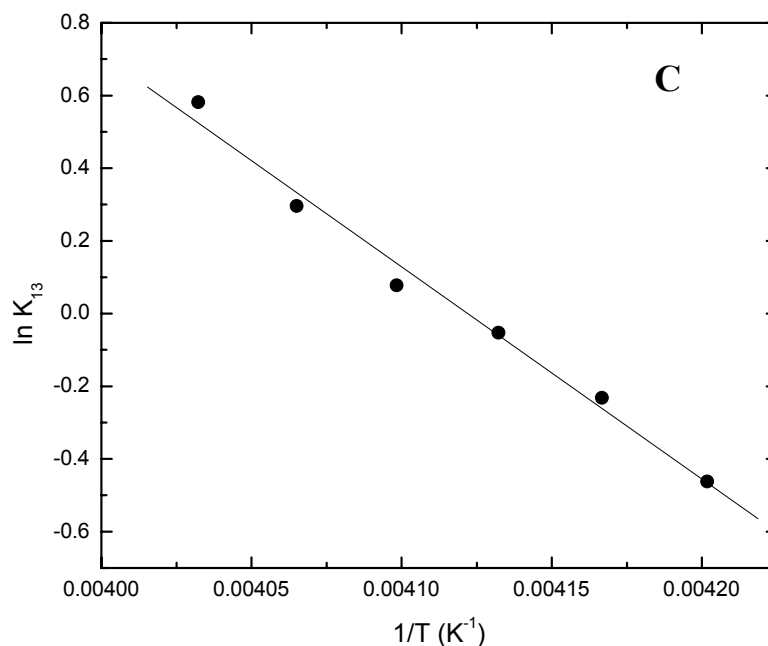


Figure 3.8: Van't Hoff plot of the equilibrium constant,  $K_{13}$ , representing the equilibrium between the ternary complex (state  $A_1$ ) and the  $\text{Co}^{\text{II}}$ -substrate radical pair (state  $A_3$ ), over the temperature range of 238-250 K. Best linear fit (solid line) parameters: (A) slope=  $-5.19 \times 10^3$ , ordinate intercept=  $2.13 \times 10^1$ ,  $R^2= 0.995$ . (B) slope=  $-5.28 \times 10^3$ , ordinate intercept=  $2.20 \times 10^1$ ,  $R^2= 0.957$ . (C) slope=  $-5.84 \times 10^3$ , ordinate intercept=  $2.40 \times 10^1$ ,  $R^2= 0.987$

EAL protein-associated contributions to the  $\text{Co}^{\text{II}}$ -radical pair stabilization process were estimated by comparison of the experimental parameters in Table 2 with data for the Co-C bond cleavage and hydrogen atom transfer sub-reactions that are associated with steps 1 and 2 in Figure 1. Solution studies indicate that Co-C bond cleavage, which is involved in the observed  $A_1 \rightarrow A_3$  reaction, is associated with a large, unfavorable enthalpy change,  $\Delta H_{\text{Co-C}}$ .<sup>22-24</sup> Comparison of  $\Delta H_{13}$  with  $\Delta H_{\text{Co-C}} = 30 \pm 2 \text{ kcal/mol}$ <sup>124</sup> indicates that the unfavorable Co-C bond cleavage is compensated by a favorable enthalpy contribution of approximately  $-19 \pm 2 \text{ kcal/mol}$  in EAL. The favorable enthalpy contribution to the  $A_1 \rightarrow A_3$  process in EAL originates, in part, from the linkage of Co-C bond cleavage to the

first hydrogen atom transfer reaction, HT1 (see Figure 1.2). The contributions of covalent bond-making and bond-breaking processes to  $\Delta H_{13}$  are estimated by using the following expression:

$$\Delta H_{\text{bond}} \approx \Delta H_{\text{Co-C}} + \Delta H_{\text{C1-H}} - \Delta H_{\text{C5-H}} \quad (3.22)$$

where  $\Delta H_{\text{C1-H}}$  and  $\Delta H_{\text{C5'-H}}$  represent the enthalpy for hydrogen atom abstraction from C1 and C5', respectively. The value of  $[\Delta H_{\text{C1-H}} - \Delta H_{\text{C5'-H}}]$  is estimated to be -5 to -7 kcal/mol, based on the experimental C-H bond dissociation energies reported for ethanol and ethane.<sup>125,126</sup> The value of -5 to -7 kcal/mol arises from the larger (more favorable) resonance stabilization energy associated with the formation of the  $\alpha$ -hydroxy-stabilized<sup>42</sup> radical at C1, relative to the primary alkyl radical at C5'. This estimate of  $[\Delta H_{\text{C1-H}} - \Delta H_{\text{C5'-H}}]$  is in general agreement with values of -6.1 kcal/mol<sup>127</sup> and -6.0 kcal/mol<sup>128</sup> calculated by using *ab initio*/density functional theory calculations of the energy change associated with hydrogen transfer between 2-ammonium-1-ethanol and the ethanol-1-yl radical in the gas phase, as a simple model for the HT1 step in EAL. Comparable values of -3.2 to -5.7 were obtained by a computational study that included auxiliary groups and additional interactions that contributed to the hydrogen transfer energy.<sup>129</sup> If an average value for  $[\Delta H_{\text{C1-H}} - \Delta H_{\text{C5'-H}}]$  of  $-6 \pm 2$  kcal/mol is assumed, then, from Eq. 3.22,  $\Delta H_{\text{bond}} \approx 24 \pm 3$  kcal/mol. The EAL protein-associated contribution to the enthalpy of the  $A_1 \rightarrow A_3$  transition is thus approximately equal to  $\Delta H_{13} - \Delta H_{\text{bond}}$ , or  $-13 \pm 3$  kcal/mol. In contrast, the residual enthalpy was zero (within the uncertainty) after subtraction of Co-C bond breaking and hydrogen atom exchange contributions to enthalpy of Co<sup>II</sup>-thiyl radical pair formation, following dGTP activator-induced Co-C

bond cleavage in RTPR.<sup>130</sup> We attribute the large, favorable protein-associated contribution to the enthalpy of the  $A_1 \rightarrow A_3$  transition in EAL to the presence of the bound substrate, which invokes changes in the protein that lead to the “substrate trigger” of cobalt-carbon bond cleavage.

Table 3.3. Values of experimentally determined thermodynamic parameters for the  $A_1$  (ternary complex) –  $A_3$  (Co<sup>II</sup>-substrate radical pair) equilibrium in the cryosolvent system, and estimated EAL protein-associated contributions.

Reaction	$\Delta G^b$ (kcal/mol)		$\Delta H$ (kcal/mol)		$\Delta S$ (cal/mol/K)	
Overall, $I \rightarrow 3$	0.0	$\pm 1.1$	10.8	$\pm 0.8$	45	$\pm 3$
EAL Contribution, <sup>a</sup> $I \rightarrow 3$	-24	$\pm 3$	-13	$\pm 3$	38	$\pm 3$

<sup>a</sup> Estimated by using Eq. 23, with  $\Delta H_{\text{Co-C}} = 30 \pm 2$  kcal/mol,<sup>24</sup>  $[\Delta H_{\text{C1-H}} - \Delta H_{\text{C5'-H}}] = -6 \pm 2$  kcal/mol,<sup>43,49-51</sup>  $\Delta S_{\text{Co-C}} = 7$  cal/mol/K,<sup>24</sup> and  $\Delta S_{\text{HT}} = 0$ , as described in the text.

<sup>b</sup> Free energy calculated for 240 K.

The van't Hoff analysis shows that the  $A_1 \rightarrow A_3$  transition in EAL is associated with a relatively large, favorable entropy change of  $\Delta S_{13} = 45 \pm 3$  cal/mol/K. In comparison,  $\Delta S_{\text{Co-C}}$  for the Co-C bond cleavage reaction in solution is smaller. A value of  $\Delta S_{\text{Co-C}} = 7 \pm 1$  cal/mol/K is estimated from the activation entropy for cleavage,<sup>124</sup> under the assumption that the bond reformation rate process is close to diffusion-controlled.<sup>130,131</sup> If it is assumed that  $\Delta S_{\text{Co-C}}$  is a reasonable estimate of the entropy change for Co-C cleavage contributed by the coenzyme in the enzyme, and that  $\Delta S \approx 0$  for the hydrogen atom transfer between carbon donor (C1) and acceptor (C5') atoms that are at van der Waals contact during reaction,<sup>25,132</sup> then the estimated protein-associated contribution to the  $A_1 \rightarrow A_3$  transition  $\Delta S_{13} - \Delta S_{\text{Co-C}} \approx 38 \pm 3$  cal/mol/K. A large entropy change of 70

cal/mol/K was determined for the dGTP-activated Co-C bond cleavage and Co<sup>II</sup>-thiyl radical pair formation in RTPR.<sup>130</sup> Thus, in RTPR, entropic effects dominate the protein-associated contribution to the dGTP-activated Co-C bond cleavage equilibrium.<sup>130</sup> The estimated protein-associated entropic contribution to the free energy change in EAL is -8.9 to  $-9.4 \pm 0.7$  kcal/mol from 234 to 248 K, respectively. Therefore, in EAL, the estimated protein-associated enthalpic and entropic contributions to the  $A_1 \rightarrow A_3$  transition are comparable.

The thermodynamic parameters for the  $A_1 \rightarrow A_3$  transition in EAL, and the estimated EAL protein-associated contributions, are summarized in Table 3.3. Figure 3.9 depicts the results of the thermodynamic measurements for low temperature in the cryosolvent system in a schematic free energy profile, including the lower limit on the free energy of the Co<sup>II</sup>-5'-deoxyadenosyl radical pair state.

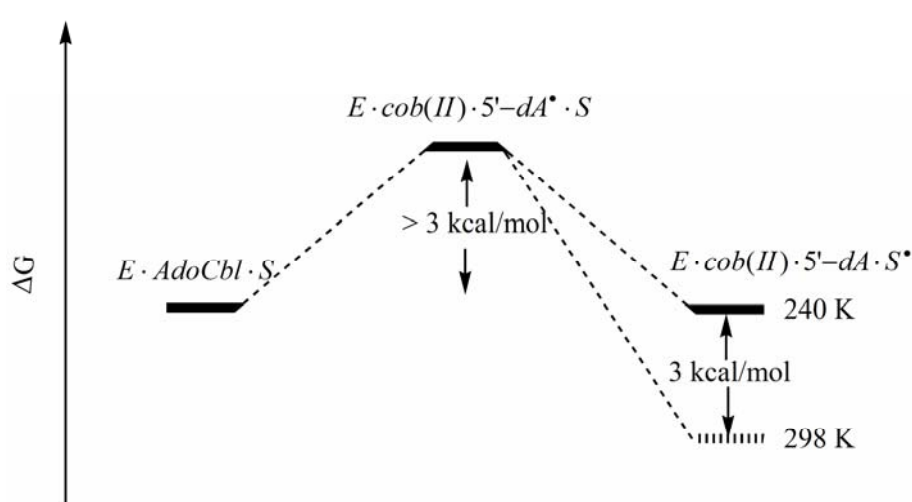


Figure 3.9: Schematic free energy diagram of the relative free energy levels of the ternary complex (state  $A_1$ ), Co<sup>II</sup>-5'-deoxyadenosyl radical pair (state  $A_2$ ), and Co<sup>II</sup>-substrate radical pair (state  $A_3$ ) in EAL. The relative free energy levels for  $T=240 \text{ K}$  are directly determined by experiment, and the change at  $T=298 \text{ K}$  is obtained by extrapolation of data for  $T=236-250 \text{ K}$ . The change in free energy between the ternary complex and Co<sup>II</sup>-substrate radical pair states at  $T=298 \text{ K}$  and  $T=240 \text{ K}$  is referenced to the level of the ternary complex.

### 3.4.4 Conclusion Remarks

The  $\Delta H_{13}$  and  $\Delta S_{13}$  values in Table 3 and the Gibbs expression lead to an estimated value for  $\Delta G_{13}$  at 298 K of  $-2.6 \pm 1.2$  kcal/mol. Therefore, under physiological conditions, the formation of the  $\text{Co}^{\text{II}}$ -substrate radical pair is predicted to be favored, relative to the ternary complex. The strong protein-associated contributions to both  $\Delta H_{13}$  and  $\Delta S_{13}$  are essential for the thermodynamic biasing of the native reaction in the forward direction of Co-C bond cleavage and  $\text{Co}^{\text{II}}$ -substrate radical pair formation.

The experimental constraint on values of  $K_{12}$  and  $K_{23}$  allow an estimation of the free energy of the  $\text{Co}^{\text{II}}$ -5'-deoxyadenosyl radical pair state for the temperature range, 234-248 K. The inequalities,  $K_{12} < 10^{-3}$  and  $K_{23} > 10^3$ , imply that  $\Delta G_{12} > 3.3$  kcal/mol and  $\Delta G_{23} < -3.3$  kcal/mol, respectively, over the range of temperatures examined. The limiting values for  $\Delta G_{12}$  and  $\Delta G_{23}$  indicate that the free energy of the  $\text{Co}^{\text{II}}$ -5'-deoxyadenosyl radical pair state is  $> 3.3$  kcal/mol, relative to the ternary complex and  $\text{Co}^{\text{II}}$ -substrate radical pair states.

**Chapter Four**

**Activation Parameters of**

**Cobalt-Carbon Bond**

**Cleavage**

Armed with the time-resolved, full spectrum continuous wave EPR technique and aiming to decouple the microscopic rates for the Co-C bond cleavage and HT1 steps from  $k_{obs}$ , we employed a three-state two-step model with the explicit consideration of 5'-deoxyadenosyl radical to quantify contributions of microscopic reaction rates to  $k_{obs}$ . From this mechanism, we were able to set a lower energy limit ( $>3.3$  kcal/mol), as compared with the ternary complex ground state energy. We also obtained thermodynamic parameters for the equilibrium between the ternary complex and the Co<sup>II</sup>-substrate radical pair from Figure as  $\Delta H_{13} = 10.8 \pm 0.8$  kcal/mol) and  $\Delta S_{13} = 45 \pm 3$  cal/mol/K by means of the temperature dependence on the experimental observable,  $\nu$ .

Based on Scheme 3.2, we have 4 variables,  $k_{12}$ ,  $k_{21}$ ,  $k_{23}$  and  $k_{32}$  to extrapolate and two equations (Eq. 3.20 and Eq. 3.21) to correlate these microscopic rate constants with experimental observables, which are the first-order rate constant  $k_{obs}$  and the normalized Co<sup>II</sup>-substrate radical pair population  $\nu$ . High resolution 6 K EPR yielded the Inequalities 3.15 and 3.16 for the population of  $A_2$ , which serves as an independent constraint.

Since the requirement to solve for a number of variables from a set of equations is that the number of the independent equations available should be equal to the number of these variables, one more experimental observable is desired to place another equation or constraint to determine the microscopic rate constants. To locate the possible origin of this equation, we will review and develop the three-state, two-step mechanism.

The time-dependence of the substrate radical concentration following the temperature step has been analyzed by using the two-step, three-state mechanism<sup>99</sup> shown in Scheme 3.2 of Chapter Three, where  $A_1$ ,  $A_2$ , and  $A_3$  represent the ternary complex, Co<sup>II</sup>-5'-deoxyadenosyl radical pair, and Co<sup>II</sup>-substrate radical pair, respectively. We have

previously demonstrated that the  $A_2$  intermediate is not detectable, with a limit<sup>26</sup>,  $[A_2]_{\infty}/[A_3]_{\infty} < 10^{-3}$ . This condition leads to a simplification of the expressions derived from the mechanism in Scheme 3.2 for the experimentally observed first-order rate constant ( $k_{obs}$ ) for growth of state  $A_3$ , and for the normalized population ratio of  $A_3$  in equilibrium, which is defined as  $v$ , as follows:

$$k_{obs} = \frac{k_{12}k_{23} + k_{21}k_{32}}{k_{21} + k_{23}} \quad (4.1)$$

$$v = \frac{[A_3]_{\infty}}{[A_1]_0} = \frac{k_{12}k_{23}}{k_{12}k_{23} + k_{21}k_{32}} \quad (4.2)$$

The analysis is extended to determine the microscopic first-order rate constant for Co-C bond cleavage, by defining a new term  $r$ , as follows:

$$r = \frac{k_{21}}{k_{23}} \quad (4.3)$$

Combining Eqs. 4.1, 4.2, and 4.3,  $k_{12}$  is expressed in terms of the experimental observables ( $k_{obs}$ ,  $v$  and  $r$ ) as:

$$k_{12} = v(1+r)k_{obs} \quad (4.4)$$

If the quantity,  $r$ , could be determined by a separate experiment, the Co-C bond cleavage rate  $k_{12}$  is straightforward to obtain. This critical information will be explored by the substrate isotope experiment in the following sections.

## 4.1 Synthesis of Deuterated Substrate

#### 4.1.1 Synthesis Protocol

[1,1-<sup>2</sup>H<sub>2</sub>]-(*S*)-2-aminopropanol is synthesized in the lab from L-alanine methyl ester<sup>18,133</sup>. The whole process comprises four major steps (full protocol listed in the Appendix):

1. Neutralize L-alanine methyl ester hydrochloride by passing through ammonia gas;
2. React with LiALD<sub>4</sub> in ether to produce the [1,1-<sup>2</sup>H<sub>2</sub>]-(*S*)-2-aminopropanol;
3. Extraction of product through a continuous extraction apparatus into pure ether;
4. Dry product in rotary evaporator.

The chemical used in the whole synthesis, including lithium aluminum deuteride, L-alanine methyl ester hydrochloride, diethyl ether and sodium sulphate, are purchased from either Sigma-Aldrich<sup>®</sup> or FisherSci<sup>®</sup>. The continuous extraction apparatus is purchased from ACE-glass<sup>®</sup> INC (part number 6840-30).

#### 4.1.2 Product Analysis

The isotopic enrichment of the product is tested by means of Electrospray Ionization (ESI) mass spectrometry technique in the Emory Mass Spectroscopy Center on a JEOL JMS-SX102/SX102A/E mass spectrometer. In addition to mass spectrometry, <sup>1</sup>H nuclear magnetic resonance spectroscopy (NMR) is applied to examine the position of deuterium atoms. In all the tests, a commercial sample ([1,1-<sup>1</sup>H<sub>2</sub>]-(*S*)-2-aminopropanol) purchased from Sigma-Aldrich<sup>®</sup> serves as the control.

Figure 4.1 shows the test result by ESI. Figure 4.1A is for [1,1-<sup>1</sup>H<sub>2</sub>]-(*S*)-2-aminopropanol and Figure 4.1B is for [1,1-<sup>2</sup>H<sub>2</sub>]-(*S*)-2-aminopropanol. From Figure 4.1A, a large peak at  $m/z = 76.07564$  is observed. This peak could be interpreted by two

possible chemical configurations,  $C_3H_{10}ON$  and  $CH_8N_4$ , the latter of which could be excluded.

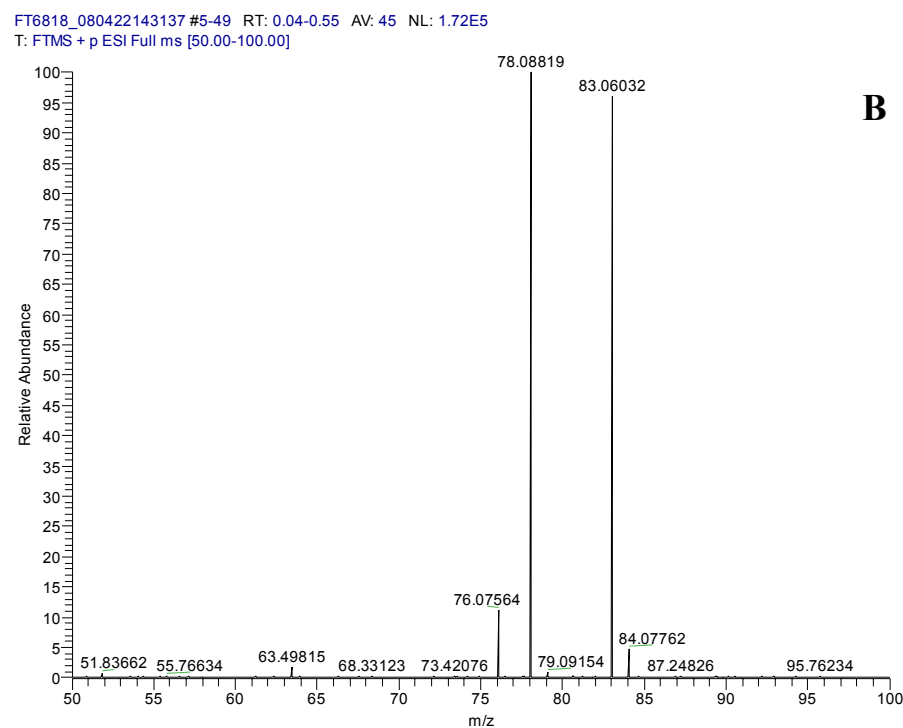
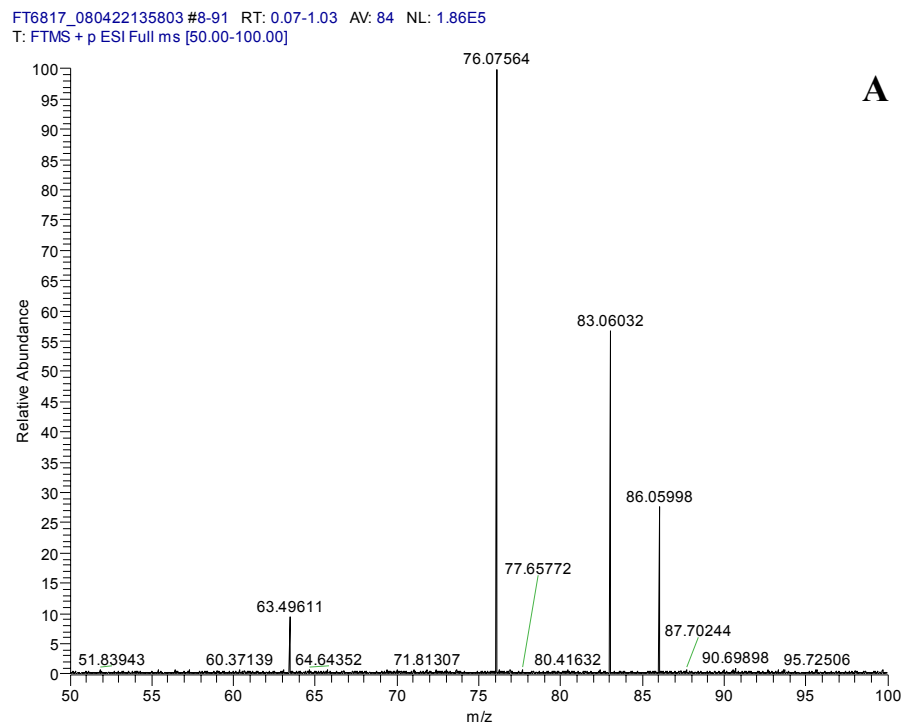
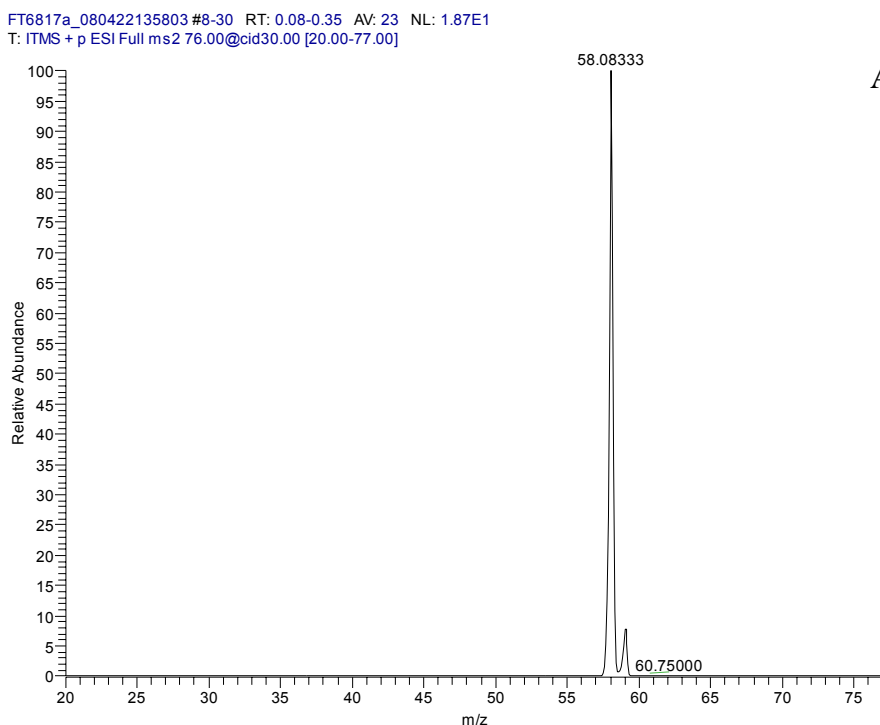


Figure 4.1: ESI spectrum for commercially obtained  $[1,1-^1\text{H}_2]$ -(*S*)-2-aminopropanol and home-synthesized  $[1,1-^2\text{H}_2]$ -(*S*)-2-aminopropanol. The 83.06032 is from the solvent used in ESI. Figure (A) represents the data collected from  $[1,1-^1\text{H}_2]$ -(*S*)-2-aminopropanol and (B) from  $[1,1-^2\text{H}_2]$ -(*S*)-2-aminopropanol.

Figure 4.1B shows a large peak at  $m/z = 78.08819$ . This peak could be interpreted by two possible chemicals as  $\text{C}_3\text{H}_8^2\text{H}_2\text{ON}$  and  $\text{CH}_6^2\text{H}_2\text{N}_4$ , the latter of which could be excluded from the synthesis protocol.

Figure 4.2 demonstrates the test result by MS/MS. Similar to Figure 4.1, Figure 4.2A is for the commercial sample  $[1,1-^1\text{H}_2]$ -(*S*)-2-aminopropanol and Figure 4.2B is for the home-synthesized sample  $[1,1-^2\text{H}_2]$ -(*S*)-2-aminopropanol. From Figure 4.2A, only one dominant peak at  $m/z = 58.0833$  is observed. This peak could be interpreted by a chemical as  $\text{C}_3\text{H}_6\text{N}$ . Comparing with Figure 4.1A, the  $\text{NH}_3$  group is believed to be fractured from  $[1,1-^1\text{H}_2]$ -(*S*)-2-aminopropanol during the data collection.



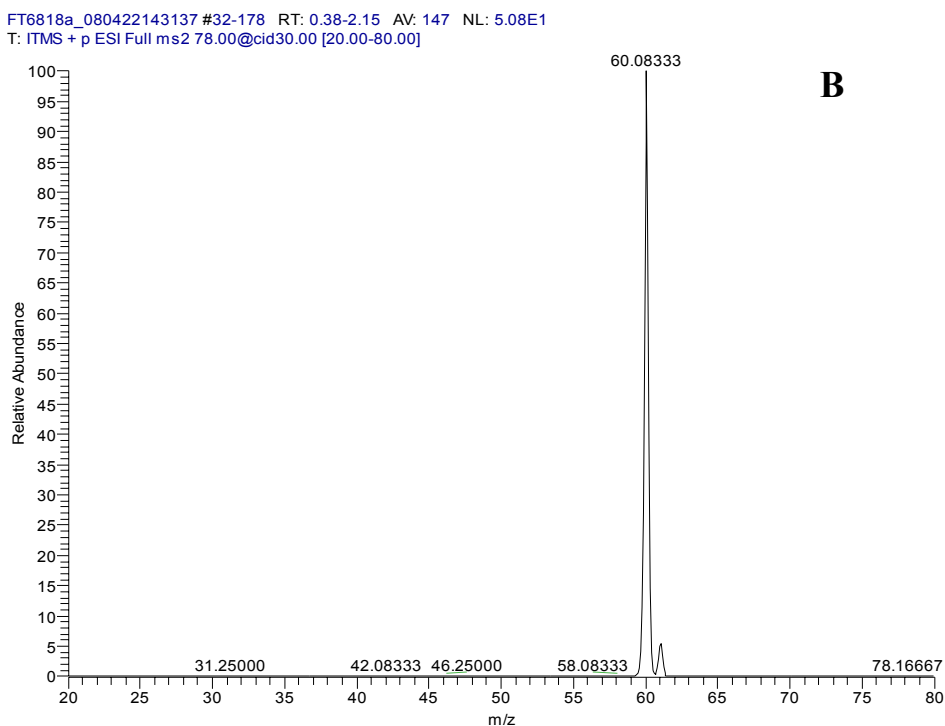


Figure 4.2: MS/MS spectrum for commercially obtained  $[1,1-^1\text{H}_2]$ -(*S*)-2-aminopropanol and home-synthesized  $[1,1-^2\text{H}_2]$ -(*S*)-2-aminopropanol. Figure (A) represents the data collected from  $[1,1-^1\text{H}_2]$ -(*S*)-2-aminopropanol and (B) from  $[1,1-^2\text{H}_2]$ -(*S*)-2-aminopropanol.

From Figure 4.2B, only one dominant peak at  $m/z = 60.0833$  is observed. This peak is shifted by exact 2.0000 unit, compared with the peak position in Figure 4.2A. Thereby, it confirms a successful substitution of two  $^1\text{H}$  atoms with  $^2\text{H}$  atoms, leading to a chemical configuration of  $\text{C}_3\text{H}_4^2\text{H}_2\text{N}$ . Similarly, the  $\text{NH}_3$  group is believed to be fractured from  $[1,1-^1\text{H}_2]$ -(*S*)-2-aminopropanol during the data collection. Though the mass spectroscopy measurements demonstrate the existence of two  $^2\text{H}$  in the home-synthesized chemical, the position of these hydrogen isotopes requires determination.

To solve this question,  $^1\text{H}$  NMR spectroscopy is applied to determine the number of protons and their relative positions by analysis of the J-J coupling in the home-synthesized chemical. From this information, the number of deuteriums and their

positions could be retrieved. All the proton NMR data are collected on an INOVA 400 console in the Emory NMR Center.

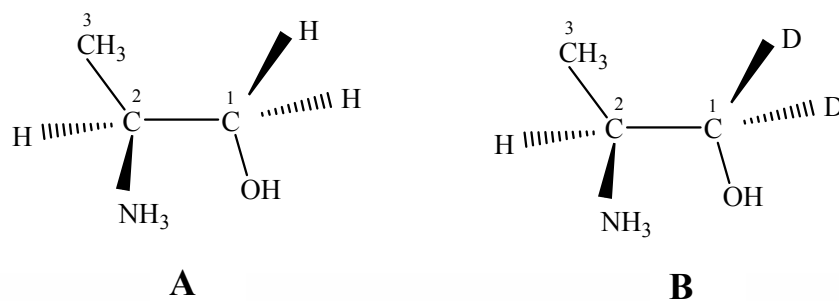


Figure 4.3: The chemical structure of  $[1,1-^1\text{H}_2]$ -(*S*)-2-aminopropanol and  $[1,1-^2\text{H}_2]$ -(*S*)-2-aminopropanol. Figure (A) represents the structure for  $[1,1-^1\text{H}_2]$ -(*S*)-2-aminopropanol and (B) for  $[1,1-^2\text{H}_2]$ -(*S*)-2-aminopropanol.

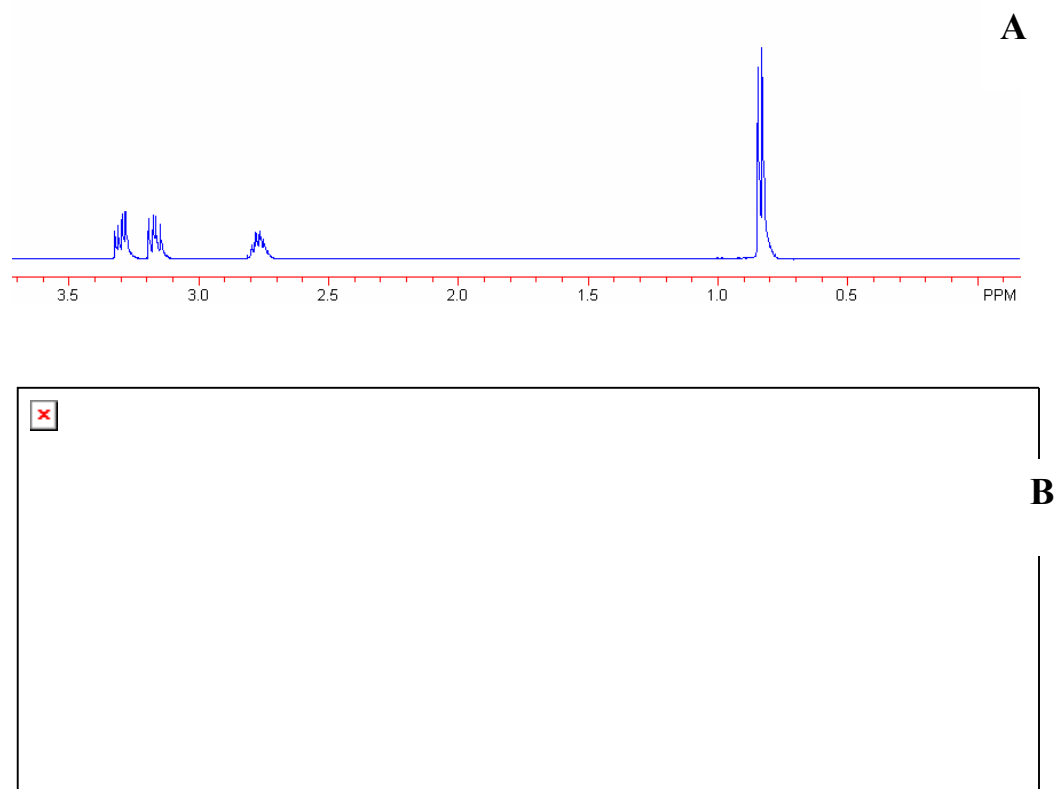


Figure 4.4: Comparison of  $^1\text{H}$  NMR spectra between  $[1,1-^1\text{H}_2]$ -(*S*)-2-aminopropanol and  $[1,1-^2\text{H}_2]$ -(*S*)-2-aminopropanol. The solvent used in the spectra collection is  $\text{D}_2\text{O}$ . Figure (A) represents the spectrum collected from  $[1,1-^1\text{H}_2]$ -(*S*)-2-aminopropanol and (B) from  $[1,1-^2\text{H}_2]$ -(*S*)-2-aminopropanol.

In all of the  $^1\text{H}$  NMR experiments,  $\text{D}_2\text{O}$  is employed as the solvent for frequency lock. Under this situation, the hydrogen atoms on the  $\text{NH}_3$  and  $\text{OH}$  group (see Figure 4.3) will be substituted by the deuterium and cannot generate a proton peak.

The  $\text{CH}_3$  group at 0.83 *ppm* in the spectrum of Figure 4.4A for  $[1,1\text{-}^1\text{H}_2]\text{-}(S)\text{-}2\text{-aminopropanol}$ , is split by the one proton on the adjacent  $\text{C}_2$  into two peaks (a doublet). The sextet at 2.75 *ppm* is from the single proton on  $\text{C}_2$ . The two protons on  $\text{C}_1$  show a pair of doublets, due to the existence of the hydroxyl group, which breaks the symmetry of the  $sp^3$  orbital. In the spectrum for Figure 4.4B, one doublet and one quartet resonance signal are observed around 1.15 *ppm* and 3.35 *ppm*. The doublet arises from the  $\text{CH}_3$  group and is split by the single proton on the adjacent  $\text{CH}$  group. The absorbance of the quartet is from the  $\text{CH}$  group and is split by the three protons on the  $\text{CH}_3$  group. Since no other  $^1\text{H}$  peaks are observed, based on comparison with Figure 4.4A, the chemical structure in Figure 4.3B is confirmed.

## 4.2 Substrate Radical Formation with Deuterated Substrate

### 4.2.1 EPR lineshape of $\text{Co}^{\text{II}}$ -substrate Radical Pair Generated with $^2\text{H}_2\text{-}$ Substrate in Aqueous and Cryosolvent Systems

Figure 4.5A shows that no significant EPR signal is observed following mixing and incubation of  $[1,1\text{-}^2\text{H}_2]\text{-}(S)\text{-}2\text{-aminopropanol}$  with holo-EAL at 230 K in the 41% DMSO/water cryosolvent by following the ternary complex preparation protocol. The minor (<1%) EPR signal component is the same as the characterized artifact signal that was observed for  $[1,1\text{-}^1\text{H}_2]\text{-}(S)\text{-}2\text{-aminopropanol}$ , and shown to be caused by kinetic

arrest and a decrease in the equilibrium constant for  $\text{Co}^{\text{II}}$ -substrate radical pair formation from the ternary complex, as demonstrated for natural abundance substrate. Figure 4.5B shows that, following T-step to 246 K and incubation for 30 min, the characteristic  $\text{Co}^{\text{II}}$ -substrate radical pair EPR spectrum develops. The partially resolved doublet splitting and broadening in the substrate radical lineshape are caused by the interaction of the unpaired electron spin at  $\text{C}_1$  of the substrate radical with the unpaired electron spin on  $\text{Co}^{\text{II}}$  <sup>23,25,121</sup>. The line shape of the substrate radical formed from  $^1\text{H}$ -substrate (Figure 4.5C) is broadened relative to the line shape in Figure 4.5B, as expected for the coupling of the unpaired electron spin at  $\text{C}_1$  with the larger nuclear magnetic moment ( $\mu_{\text{B}}$ ) of protium ( $\mu_{\text{B}}^{\text{H}}/\mu_{\text{B}}^{\text{D}}=3.26$ ).

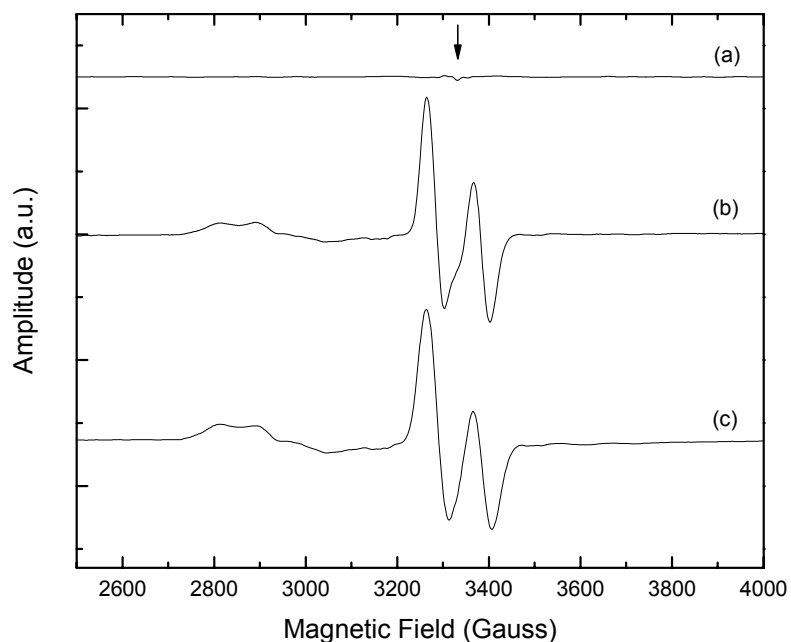


Figure 4.5: X-band continuous-wave EPR spectra of cryotrapped holo-EAL and substrate [1,1- $^2\text{H}_2$ ]-(*S*)-2-aminopropanol mixtures under different conditions of solvent and temperature. EPR spectroscopy was performed at  $T=120$  K. The concentrations of EAL active sites and coenzyme  $\text{B}_{12}$  were  $120 \mu\text{M}$  and  $12 \text{ mM}$ , respectively. (A) EPR spectrum of holo-EAL and  $^2\text{H}$ -substrate after mixing and incubation for 5 min at 230 K. (B) EPR spectrum of the  $\text{Co}^{\text{II}}$ -substrate radical pair state in aqueous solution. Holo-EAL was mixed with substrate at 246 K, and then incubated for 30 min, prior to cryotrapping. (C) EPR spectrum of the  $\text{Co}^{\text{II}}$ -substrate radical pair state in

aqueous cryosolvent. *EPR conditions*: microwave frequency, 9.372 GHz; microwave power, 10 dB (20 mW); magnetic field modulation, 10 Gauss peak-peak; modulation frequency, 100 kHz; field sweep rate, 1.5 Gauss s<sup>-1</sup>; time constant, 164 ms; average of 4 sweeps, minus average of 4 baseline spectra.

#### 4.2.2 Time-dependence of Co<sup>II</sup>-substrate Radical Pair Formation with <sup>2</sup>H-

##### Substrate

Figure 4.6 shows the time dependence of the substrate radical portion of the radical pair EPR spectrum, following T-step of the ternary complex with <sup>2</sup>H-substrate at 242 K. As shown by the plot and fit of the peak-to-trough amplitude ( $A_{pt}$ ) as a function of time in Figure 4.7, the single exponential growth (observed first-order rate constant,  $k_{obs}$ ) leads to a stable amplitude at long times, which corresponds to a fraction of Co<sup>II</sup>-substrate radical pair relative to initial ternary complex in equilibrium. No paramagnetic states, other than the Co<sup>II</sup>-substrate radical pair, are detected. These features of the T-step experiment have been observed previously for the reaction of the ternary complex formed with <sup>1</sup>H-substrate.

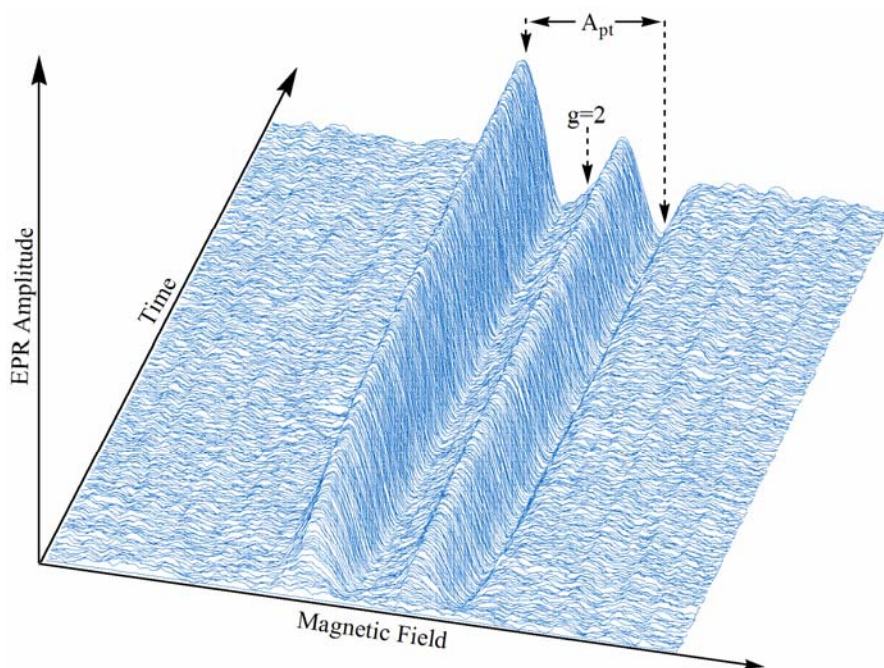


Figure 4.6: Time-dependence of the EPR spectrum of the  $^2\text{H}$ -substrate radical pair state in EAL in the cryosolvent system at  $T=242$  K, following temperature-step initiation of reaction. The time interval between each single-sweep spectrum is 15 s. The free electron resonance position at  $g=2.0$  is shown by the arrow. The first peak and second trough are positioned at 3284 and 3415 Gauss, respectively. The full extents of the magnetic field sweep and time course are 560 Gauss and  $6.43 \times 10^3$  s, respectively. The concentrations of EAL active sites and coenzyme  $\text{B}_{12}$  are 150  $\mu\text{M}$  and 15 mM, respectively. *EPR Conditions*: microwave frequency, 9.363 GHz; microwave power, 10 dB (20 mW); magnetic field modulation, 12 Gauss; modulation frequency, 100 kHz; scan rate: 53 Gauss  $\text{s}^{-1}$ ; time constant, 164 ms. The  $t=0$  spectrum (baseline) has been subtracted from each spectrum.

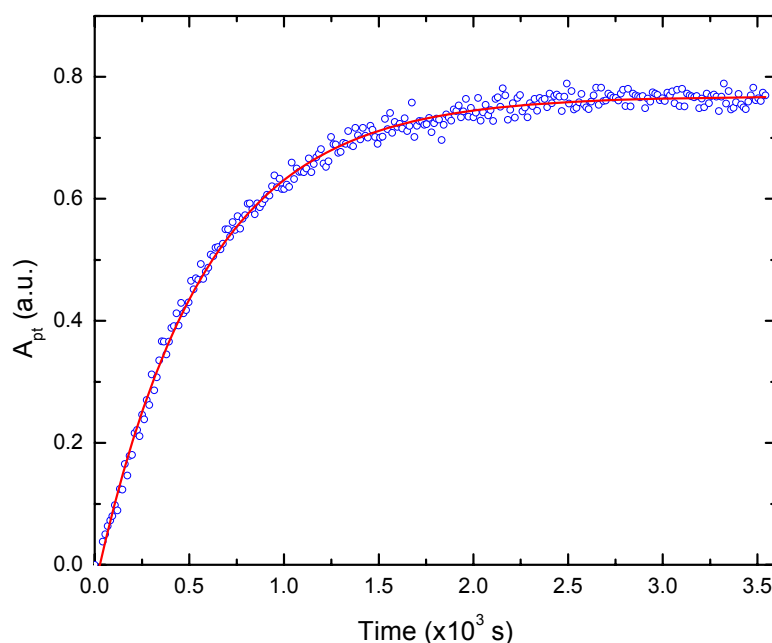


Figure 4.7: Time-dependence of the EPR amplitude of the  $^2\text{H}$ -substrate radical pair state in EAL in the cryosolvent system at  $T=242$  K, following temperature-jump initiation of reaction. The amplitude is given by the difference between the first peak (3284 Gauss) and second trough (3415 Gauss) amplitudes, as defined in Figure 4.3. Note that the data are truncated at  $3.50 \times 10^3$  s, relative to the full time scale of  $6.43 \times 10^3$  s presented in Figure 4.6. The experimental data points are overlaid with the best-fit exponential growth function (solid curve;  $k_{\text{obs}} = 1.77 \times 10^{-3} \text{ s}^{-1}$ ). EPR conditions are as described in legend to Figure 4.6.

### 4.2.3 Temperature-dependence of $k_{\text{obs}}$ with $^2\text{H}$ -Substrate

Figure 4.8 shows the natural logarithm of  $k_{\text{obs}}/T$  plotted as a function of inverse absolute temperature, in the Eyring plot form. The average values of  $k_{\text{obs}}$  for the different

temperatures, and standard deviations that represent at least three separate determinations, are collected in Table 4.1. The Arrhenius plot is linear, which suggests that the kinetic mechanism and the rate limiting step for  $\text{Co}^{\text{II}}$ -substrate radical pair formation are maintained over the temperature range of 234-246 K with  $^2\text{H}$ -substrate.

Table 4.1 also includes the ratios of the first-order rate constant  $k_{obs}$  between  $^1\text{H}$ - and  $^2\text{H}$ -substrate, which give the kinetic  $^1\text{H}/^2\text{H}$  hydrogen isotope effect at each temperature. The average of the substrate  $^1\text{H}/^2\text{H}$  isotope effect on  $k_{obs}$  over the examined temperatures is  $0.9 \pm 0.3$ , which is unity within one standard deviation. This is significantly smaller than the  $^1\text{H}/^2\text{H}$  isotope effect of 3.1 on the rate of formation of cob(II)alamin following mixing holo-EAL with substrate in stopped-flow studies at room temperature, and much smaller than the proposed intrinsic  $^1\text{H}/^2\text{H}$  isotope effect on the hydrogen atom transfer step. The subtle isotope effect indicates that the hydrogen atom transfer step is not rate-determining for the formation of the  $\text{Co}^{\text{II}}$ -substrate radical pair over the temperature range from 234 K to 246 K.

Table 4.1: Values of the observed rate constant for  $\text{Co}^{\text{II}}$ -substrate radical pair formation at different absolute temperatures for  $^1\text{H}$ -substrate ( $k_{obs}^H$ ) and  $^2\text{H}$ -substrate ( $k_{obs}^D$ ). Values represent the average of at least three separate experiments, and the corresponding standard deviation. The kinetic isotope effect is thereby calculated based on these values.

$T(\text{K})$	$k_{obs}^H (\times 10^3 \text{ s}^{-1})$		$k_{obs}^D (\times 10^3 \text{ s}^{-1})$		$k_{obs}^H/k_{obs}^D$	
234	0.29	$\pm 0.06$	0.28	$\pm 0.08$	1.0	$\pm 0.3$
236	0.39	$\pm 0.04$	0.51	$\pm 0.01$	0.8	$\pm 0.1$
238	0.58	$\pm 0.08$	0.7	$\pm 0.1$	0.8	$\pm 0.2$
240	1.1	$\pm 0.07$	1.0	$\pm 0.2$	1.1	$\pm 0.2$
242	1.5	$\pm 0.2$	1.9	$\pm 0.1$	0.8	$\pm 0.1$
244	2.5	$\pm 0.5$	3.1	$\pm 0.2$	0.8	$\pm 0.1$
246	4.4	$\pm 0.3$	3.8	$\pm 0.3$	1.2	$\pm 0.1$

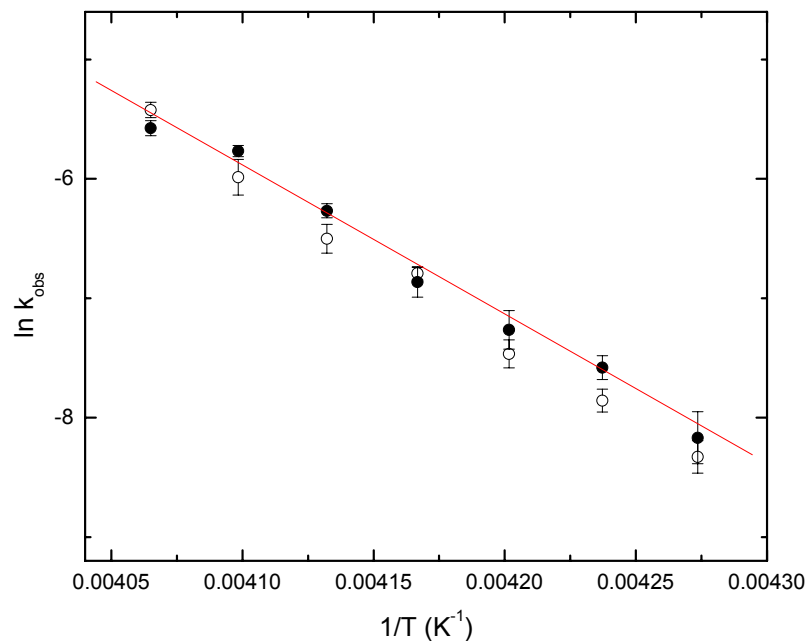


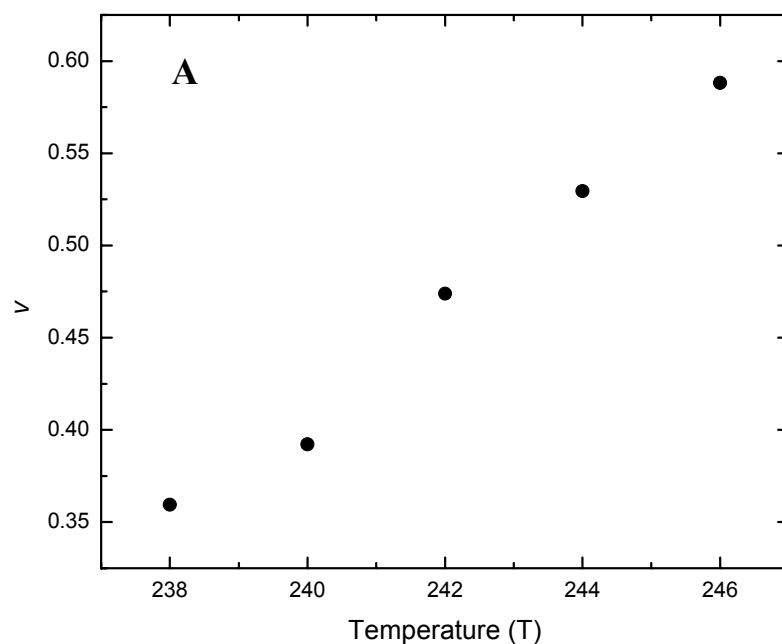
Figure 4.8: Dependence of the natural logarithm of the observed first-order rate constant for growth of the  $^2\text{H}$ -substrate radical EPR signal on the inverse absolute temperature from  $T=234$ - $246$  K (solid circles). The kinetic data for  $^1\text{H}$ -substrate is added to the plot (hollow circles) for better comparison. The substrate:active sites ratio was 100, and the concentration of active sites was  $150\ \mu\text{M}$ . The error bars represent the standard deviation obtained by combining three separate measurements at each temperature, which used EAL from three different preparations. Best linear fit (solid line) parameters: slope= $-1.25 \times 10^4$ , ordinate intercept= $4.50 \times 10^1$ ,  $R^2=0.99$ .

#### 4.2.4 Temperature-dependence of $\nu$ with $^2\text{H}$ -Substrate

Temperature perturbation experiments are used to determine the normalized population ratio of  $\text{Co}^{\text{II}}$ -substrate radical pair in the equilibrium state ( $\nu$  in Eq. 4.2) for  $^2\text{H}$ -substrate in the temperature range from 238-246 K. Figure 4.9A shows the normalized substrate radical amplitude,  $\nu$ , as a function of temperature (additional data is presented in Figure 4.9B). The amplitude is normalized by using the amplitude of the substrate radical signal obtained after warming the sample to 273 K, followed by 5 min incubation at this temperature (see Eq. 3.14). The sequence of temperature changes is as follows: 238 $\rightarrow$ 242, 242 $\rightarrow$ 240, 240 $\rightarrow$ 246, 246 $\rightarrow$ 244. The linear trend in Figure 4.9 indicates a

reversible, temperature-dependent equilibrium between the ternary complex and the  $\text{Co}^{\text{II}}$ -substrate radical pair state.

The thermodynamic parameters,  $\Delta G_{13}^D$ ,  $\Delta H_{13}^D$  and  $\Delta S_{13}^D$  for the transition from the  $A_1$  (ternary complex) state to the  $A_3$  ( $\text{Co}^{\text{II}}$ -substrate radical pair) state can be determined by van't Hoff analysis of  $K_{13}$  (Eqs. 3.10 and 3.13). Values of  $K_{13}$  at different temperatures are obtained from the corresponding  $\nu$  values by using Eq. 3.22. Figure 4.10A shows the van't Hoff plot for  $K_{13}$  that was obtained by using the  $\nu$  values presented in Figure 4.9A. One additional van't Hoff plots from separate experiments are shown in Figure 4.9B. Table 4.3 presents values of  $\Delta H_{13}^D$  ( $11 \pm 2$  kcal/mol) and  $\Delta S_{13}^D$  ( $47 \pm 14$  cal/mol/K) that are obtained from the average of the linear fit parameters from each van't Hoff plot.



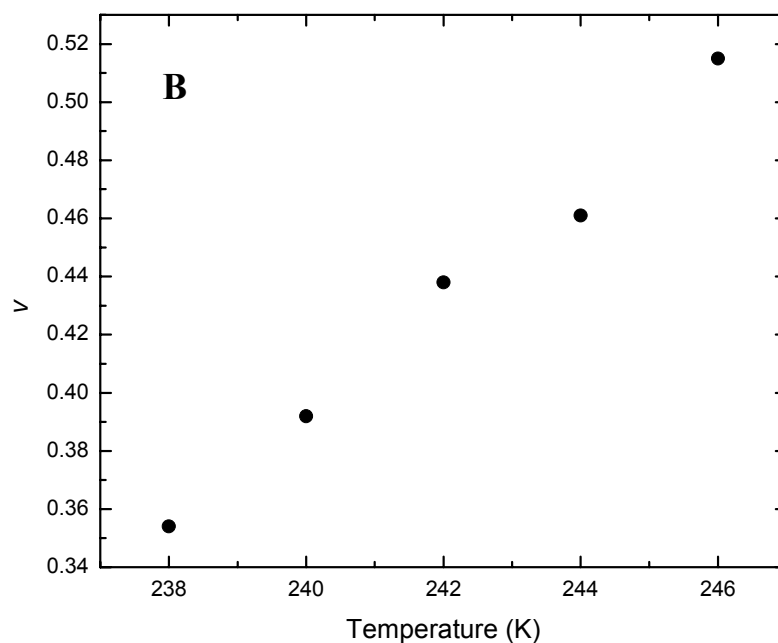


Figure 4.9: Normalized equilibrium saturation of the substrate radical EPR amplitude as a function of absolute temperature for two runs with different samples. The results for a single sample are shown in A and B separately, with the non-monotonic sequence of temperature values as described in the text. The EAL active site and substrate concentrations are 150  $\mu\text{M}$  and 15 mM, respectively.

Table 4.2: Values of experimentally determined population ratio for the equilibrated  $A_3$  (ternary complex) and the initial  $A_1$  ( $\text{Co}^{\text{II}}$ -substrate radical pair) in the cryosolvent system.

$T(\text{K})$	$v^H$		$v^D$		$v^H/v^D$	
238	0.45	$\pm 0.06$	0.59	$\pm 0.10$	0.76	$\pm 0.14$
240	0.50	$\pm 0.04$	0.64	$\pm 0.09$	0.78	$\pm 0.13$
242	0.55	$\pm 0.05$	0.69	$\pm 0.11$	0.80	$\pm 0.15$
244	0.59	$\pm 0.03$	0.72	$\pm 0.14$	0.82	$\pm 0.16$
246	0.63	$\pm 0.03$	0.76	$\pm 0.15$	0.83	$\pm 0.17$

Table 4.2 demonstrates that the average of the substrate  $^1\text{H}/^2\text{H}$  isotope effect on  $v$  is  $0.8 \pm 0.2$ , which is less than unity. The equilibrium isotope effect on  $v$  suggests that the sum of the energies of the C-H bonds that for  $^2\text{H}$ -substrate in the  $\text{Co}^{\text{II}}$ -substrate radical pair formation from the ternary complex is lower (stronger C-H bonds) than  $^1\text{H}$ -substrate.

This isotope effect is consistent with literature values for the strong, primary C5'-H bond and  $\alpha$ -hydroxy radical C-H bond formed in the radical pair, and the two relatively weak  $\alpha$ -hydroxy C-H that are present in substrate in the ternary complex.

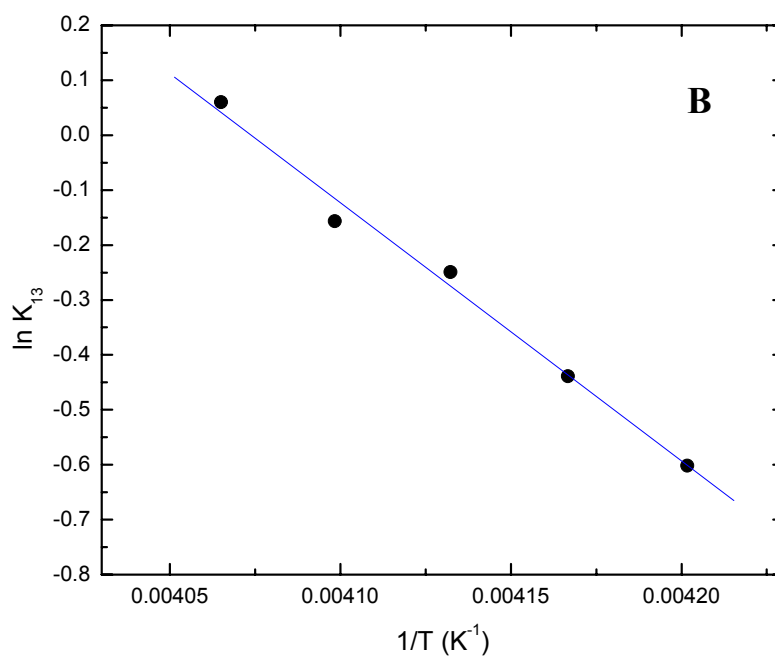
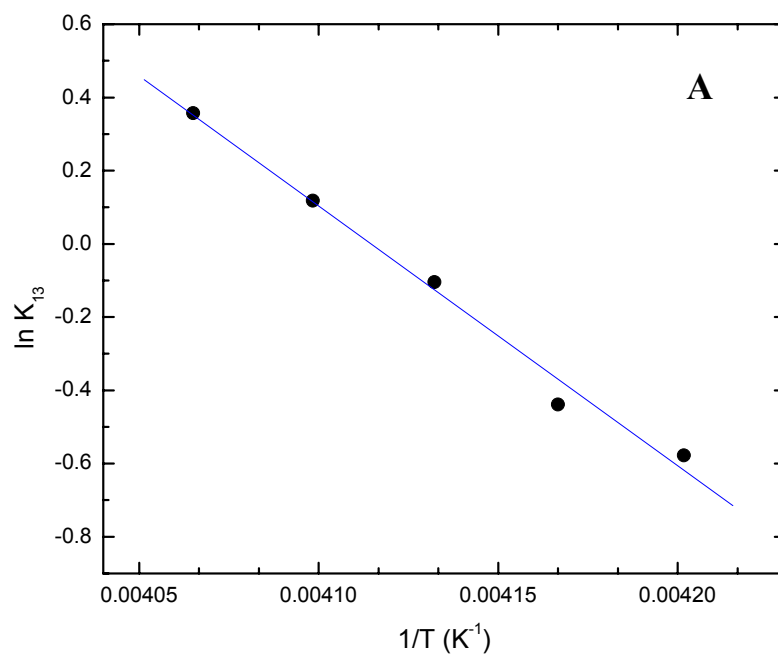


Figure 4.10: Van't Hoff plot of the equilibrium constant,  $K_{13}$ , representing the equilibrium between the ternary complex (state  $A_1$ ) and the  $\text{Co}^{\text{II}}$ -substrate radical pair (state  $A_3$ ), over the temperature range of 238-246 K from the data shown in Figure 4.9. Best linear fit (solid line) parameters: (A) slope=  $-7.1 \times 10^3$ , ordinate intercept=  $2.9 \times 10^1$ ,  $R^2= 0.994$ ; (B) slope=  $-4.7 \times 10^3$ , ordinate intercept=  $1.9 \times 10^1$ ,  $R^2= 0.995$ .

Table 4.3: Values of experimentally determined thermodynamic parameters for the  $A_1$  (ternary complex) –  $A_3$  ( $\text{Co}^{\text{II}}$ -substrate radical pair) equilibrium in the cryosolvent system.

substrate	$\Delta H_{13}(\text{kcal/mol})$		$\Delta S_{13}(\text{cal/mol/K})$	
$[1,1\text{-}^1\text{H}_2]\text{-(S)-2-aminopropanol}$	10.8	$\pm 0.8$	45	$\pm 3$
$[1,1\text{-}^2\text{H}_2]\text{-(S)-2-aminopropanol}$	11	$\pm 2$	47	$\pm 14$

## 4.2 Revisiting the Three-step, Two-state Reaction Model

Eq. 4.4 shows that the value of  $k_{12}$ , which represents the first-order rate constant for the Co-C bond cleavage step in Scheme 3.2, can be calculated, if the three quantities ( $k_{obs}$ ,  $v$ , and  $r$ ) are known. The  $k_{obs}$  and  $v$  for  $^1\text{H}$ - and  $^2\text{H}$  substrate have been directly obtained. In the following, we utilize the substrate hydrogen isotope effects to obtain the upper limit on  $r$  for  $^1\text{H}$ -substrate as  $r \ll 1$ . Therefore, Eq 4.4 can be simplified with dropping the  $r$  term within a well-defined limit of certainty.

From the three-state two-step model (Scheme 3.2), the  $k_{12}$  could be expressed for naturally abundant and deuterated substrate respectively as:

$$k_{12}^H(T_{low}) = v^H(T_{low})[1 + r^H(T_{low})]k_{obs}^H(T_{low}) \quad (4.5)$$

$$k_{12}^D(T_{low}) = v^D(T_{low})[1 + r^D(T_{low})]k_{obs}^D(T_{low}) \quad (4.6)$$

where the superscript  $H$  and  $D$  denotes the type of substrate in the reaction and  $T_{low}$  refers to any temperature point within 234 – 246 K.

The two-step mechanism for the reaction of the ternary complex in Scheme 3.2 indicates that the isotope substituted C-H bonds are not chemically altered during step 1, and therefore:

$$k_{12}^H(T_{low}) = k_{12}^D(T_{low}) \quad (4.7)$$

Substitution of the average values of the isotope effect,  $\frac{k_{obs}^H(T_{low})}{k_{obs}^D(T_{low})} = 0.9 \pm 0.3$  and

$\frac{v^H(T_{low})}{v^D(T_{low})} = 0.8 \pm 0.2$ , obtained from Table 4.1 and Table 4.2, into Eqs. 4.5 and 4.6 leads to

the following expression:

$$\frac{k_{obs}^H(T_{low})v^H(T_{low})}{k_{obs}^D(T_{low})v^D(T_{low})} = 0.72 + a \quad (4.8)$$

where  $a$  is the uncertainty. The absolute value of  $a$  can be estimated from the error propagation as:

$$|a| < 0.3 \quad (4.9)$$

Combing Eqs. 4.5, 4.6, 4.7 and 4.8, we have

$$\frac{1 + r^D(T_{low})}{1 + r^H(T_{low})} = \frac{k_{obs}^H(T_{low})v^H(T_{low})}{k_{obs}^D(T_{low})v^D(T_{low})} = 0.72 + a \quad (4.10)$$

The limit on the uncertainty is obtained by considering results from ambient temperature. Reed and coworkers have reported the substrate hydrogen isotope effect on Co<sup>II</sup>-substrate radical pair formation in stopped-flow mixing experiment for (S)-2-aminopropanol in EAL.<sup>18</sup> Their result yields:

$$\frac{k_{obs}^H(298K)}{k_{obs}^D(298K)} = 3.1 \quad (4.11)$$

All of the EAL active sites are occupied by the Co<sup>II</sup>-substrate radical pair at room temperature.<sup>17</sup> Therefore, the following equation holds true:

$$\frac{v^H(298K)}{v^D(298K)} = 1 \quad (4.12)$$

Substitution of Eqs. 4.11 and 4.12 into the generate set of equations (Eqs. 4.5, 4.6 and 4.7) for the three-step, two-state model leads to the following expressions:

$$r^D(298K) = 2.1 + 3.1r^H(298K) \quad (4.13)$$

Therefore the following inequality is valid at ambient temperature:

$$r^D(298K) > 3.1r^H(298K) \quad (4.14)$$

From Eqs. 4.3 and 4.7, the ratio  $r^D/r^H = k_{23}^H/k_{23}^D$  represents the intrinsic isotope effect in HT1. The general temperature dependence of the isotope effect on hydrogen transfer guarantees another inequality<sup>134,135</sup>, as follows:

$$\frac{r^D(T_{low})}{r^H(T_{low})} > \frac{r^D(298K)}{r^H(298K)} > 3.1 \quad (4.15)$$

Substitution of Inequality 4.15 into Eq. 4.10 leads to the following expression:

$$0.72 + a = \frac{1 + r^D(T_{low})}{1 + r^H(T_{low})} > \frac{1 + 3.1r^H(T_{low})}{1 + r^H(T_{low})} \quad (4.16)$$

By rearrange Inequality 4.16 and consider Inequality 4.9, the  $r^H(T_{low})$  could be assessed with an upper limit as:

$$r^H(T_{low}) < \frac{a - 0.28}{2.38 - a} < 0.01 \quad (4.17)$$

The derivation of the upper limit for  $r^H(T_{low})$  does not count in any factor arising from the temperature dependence of the isotope effect in Inequality 4.15. Theoretically, at low temperature, the hydrogen tunneling term will contribute significantly to  $k_{23}$ . The hydrogen isotope effect thus will be much larger than at room temperature. Experimentally, over six orders of magnitude increase due to temperature drop on kinetic isotope effect (*KIE*) has been reported.<sup>136</sup>

Even with a lenient consideration, the quantity of  $r$  is two still orders of magnitude less than 1. Therefore, the following equation is adapted to calculate  $k_{12}^H$  between 234 – 246 K:

$$k_{12}^H(T_{low}) = v^H(T_{low})k_{obs}^H(T_{low}) \quad (4.18)$$

The error in  $k_{12}^H(T_{low})$  is less than 1%.

#### 4.4 Retrieving Co-C Bond Cleavage Activation Parameters

By using Eq. 4.18, the Co-C bond cleavage rate  $k_{12}$  is calculated from the experimental determined  $k_{obs}$  and  $v$  in the temperature range from 234 – 246 K. From the linear fitting of  $\ln k_{12}/T$  vs.  $1/T$  in Figure 11, the following activation parameters are obtained for the Co-C bond cleavage step as:  $\Delta H_{12}^\ddagger = 32 \pm 1$  kcal/mol and  $\Delta S_{12}^\ddagger = 62 \pm 5$  cal/mol/K. The Gibbs free energy  $\Delta G_{12}^\ddagger$  at any given temperature could be extrapolated by using following equation:

$$\Delta G_{12}^\ddagger = \Delta H_{12}^\ddagger - T\Delta S_{12}^\ddagger \quad (4.19)$$

At 298 K,  $\Delta G_{12}^\ddagger$  is  $13.5 \pm 1.8$  kcal/mol from Eq. 4.19. The corresponding reaction (Co-C bond cleavage) rate at this temperature is  $750 \text{ s}^{-1}$  based on Eq. 3.12. Reed and coworkers reported that the first-order reaction rate for the formation of the  $\text{Co}^{\text{II}}$  state in EAL at 298 K following the mixing of holoenzyme and (*S*)-2-aminopropanol is  $74 \text{ s}^{-1}$ , which means that  $k_{obs}^H(298 \text{ K})=74 \text{ s}^{-1}$  in the three-state two-step mechanism. Another experimental fact is that at ambient temperature, all the active sites of the EAL are occupied by the  $\text{Co}^{\text{II}}$ -substrate radical pair. Therefore, the population ratio term  $v^H(298 \text{ K}) = 1$ . From these results, the coupling term  $r$  between Co-C bond cleavage and HT1 could be calculated based on Eq. 4.5 as  $r^H(298 \text{ K}) = 9$ .

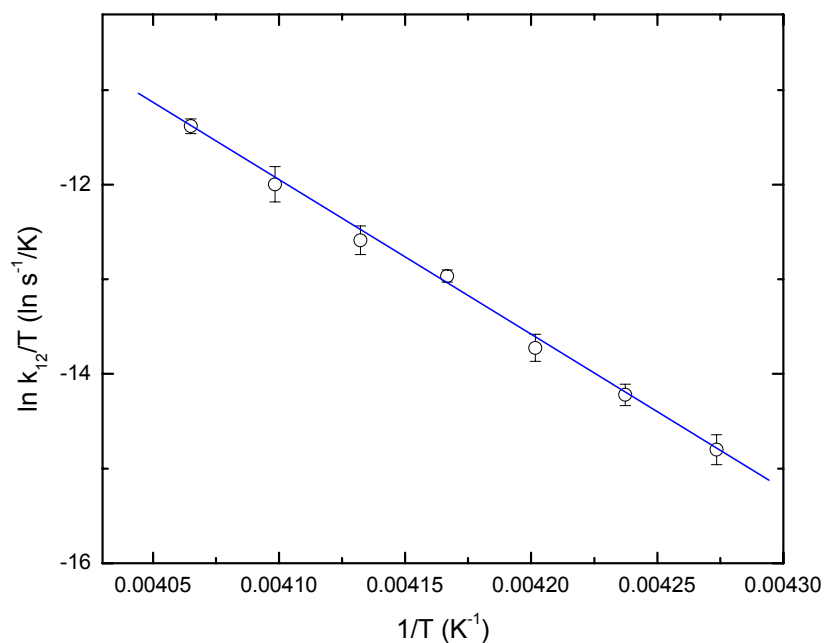


Figure 4.11: Eyring plot of the calculated Co-C bond cleavage rate constant. The substrate:active sites ratio was 100, and the concentration of active sites was  $150 \mu\text{M}$ . The error bars represent the standard deviation obtained by combining three separate measurements at each temperature, which used EAL from three different preparations. Best linear fit (solid line) parameters: slope=  $-1.6 \times 10^4$ , ordinate intercept=  $5.90 \times 10^1$ ,  $R^2 = 0.998$ .

According to the definition of  $r$  in Eq. 4.3 and the transition state theory in Eq. 3.12,  $r$  is related to the free energy difference between the transition states of Co-C bond cleavage and HT1:

$$r^H = \frac{k_{21}^H}{k_{23}^H} = \frac{\exp[-\Delta G_{21}^\ddagger(H)/RT]}{\exp[-\Delta G_{23}^\ddagger(H)/RT]} = \exp\left[\frac{\Delta G_{23}^\ddagger(H) - \Delta G_{21}^\ddagger(H)}{RT}\right] \quad (4.20)$$

To further explore the physical meaning of  $r$ , we adopt the symbol  $ZPE_{Co-C}^\ddagger$  to represent the zero-point energy for the transition state in Co-C bond cleavage step,  $ZPE_{HT1}^\ddagger$  to represent the zero-point energy for the transition state in HT1 step and  $ZPE_2$  to represent the ground state energy for the  $Co^{II}$ -5'-deoxydenosyl radical pair. Equation 4.20 could be rewritten as<sup>137</sup>:

$$r^H = \exp\left[\frac{\Delta G_{23}^\ddagger(H) - \Delta G_{21}^\ddagger(H)}{RT}\right] = \exp\left[\frac{(ZPE_{HT1}^\ddagger(H) - ZPE_2(H)) - (ZPE_{Co-C}^\ddagger(H) - ZPE_2(H))}{RT}\right] = \exp\left[\frac{ZPE_{HT1}^\ddagger(H) - ZPE_{Co-C}^\ddagger(H)}{RT}\right] \quad (4.21)$$

Therefore

$$ZPE_{HT1}^\ddagger(H) - ZPE_{Co-C}^\ddagger(H) = RT \ln r^H \quad (4.22)$$

Substitution of the value of  $r^H$  at 298 K into Eq. 4.22, we get

$$ZPE_{HT1}^\ddagger(H, 298K) - ZPE_{Co-C}^\ddagger(H, 298K) = 1.3 \text{ kcal/mol} \quad (4.23)$$

The result from Eq. 4.23 suggests that the transition state zero-point energy for the HT1 step is about 1 kcal/mol higher than the Co-C bond cleavage step under physiological condition.

Reed and coworkers also reported that the kinetic isotope effect for deuterated substrate is 3.1. Therefore,  $k_{obs}^D(298\text{ K})=23.9\text{ s}^{-1}$ . The Co-C bond cleavage is substrate isotope independent, and therefore, the analogous relation to Eq. 4.7 holds at ambient temperature, as follows:

$$k_{12}^D = k_{12}^H \quad (4.24)$$

Substitution of the extrapolated reaction rate for the Co-C bond cleavage at 298 K from naturally abundant substrate into Eq. 4.6, and the population ratio relation at ambient temperature of  $v^D(298\text{ K})=1$ , allows a coupling term  $r^D$  to be calculated. The results show that  $r^D(298\text{ K})=30$ . Following a similar procedure derived above for the naturally abundant substrate, we unraveled the following relationships:

$$ZPE_{HT1}^\ddagger(D,298K) - ZPE_{Co-C}^\ddagger(D,298K) = 2.0\text{ kcal/mol} \quad (4.25)$$

Since the Co-C bond cleavage is not substrate isotope sensitive,

$$ZPE_{Co-C}^\ddagger(H,298K) = ZPE_{Co-C}^\ddagger(D,298K) \quad (4.26)$$

Eq. 4.23 is subtracted from Eq. 4.25 and combined with Eq. 4.26, then obtain:

$$ZPE_{HT1}^\ddagger(D,298K) - ZPE_{HT1}^\ddagger(H,298K) = 0.7\text{ kcal/mol} \quad (4.27)$$

At 240 K, which is the temperature that we carried out the kinetic studies, the  $r^H$  is only assessed with an upper limit of 0.01. Applying this limit into Eq. 4.22, we get:

$$ZPE_{Co-C}^\ddagger(H,240K) - ZPE_{HT1}^\ddagger(H,240K) \geq 2.2\text{ kcal/mol} \quad (4.28)$$

Combining results from above (Eqs. 4.23 and 4.28), the free energy curve including the Co-C bond cleavage and HT1 steps is depicted in Figure 4.12 for 298 K and 240 K separately.

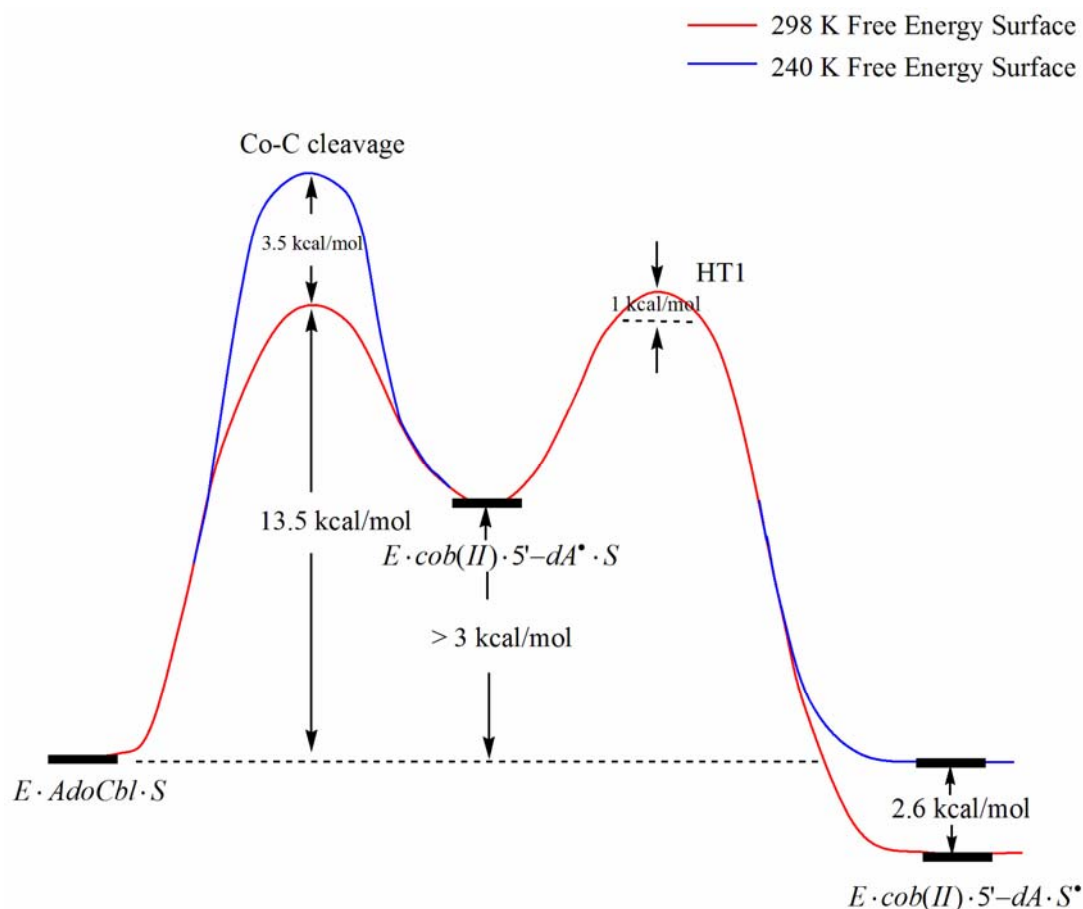
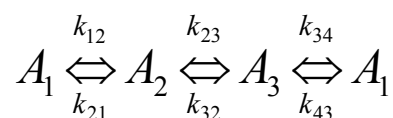


Figure 4.12: Schematic free energy diagram of the reaction curve of the ternary complex (state  $A_1$ ),  $Co^{II}$ -5'-deoxyadenosyl radical pair (state  $A_2$ ), and  $Co^{II}$ -substrate radical pair (state  $A_3$ ) in EAL. The relative free energy levels for  $T=240$  K were directly determined by experiment, and the change at  $T=298$  K was obtained by extrapolation of data for  $T=236$ -248 K.

## 4.5 Other Possible Reaction Schemes

One of the challenges in the kinetic studies is determining the appropriate reaction model. In the reaction Scheme 3.2, only the Co-C bond cleavage and HT1 step are considered without consideration of possible intermediate states, which may be the long range C5'-deoxydenosyl radical migration. In this section, we will explore a four-state, three-step reaction mechanism with Co-C bond cleavage, C5'-deoxydenosyl radical migration and HT1 step (Scheme 4.1)



Scheme 4.1: The four-state, three-step mechanism. This mechanism considers the Co-C bond cleavage, C5'-Ado radical migration and HT1 steps.

Consider three consecutive first-order reactions from four-state three-step mechanism (Scheme 4.1), the secular equation is:

$$\begin{vmatrix} k_{12} - \lambda & -k_{21} & 0 & 0 \\ -k_{12} & k_{21} + k_{23} - \lambda & -k_{32} & 0 \\ 0 & -k_{23} & k_{32} + k_{34} - \lambda & -k_{43} \\ 0 & 0 & -k_{34} & k_{43} - \lambda \end{vmatrix} = 0 \quad (4.29)$$

The values of the particular solution for the secular equation are  $\lambda_r$  ( $r=1, 2, \dots, m$ ). For these solutions, there is a set of relative values  $B_{jr}$  corresponding to each  $\lambda_r$ . Once the secular equation is solved, the general solution for  $A_i$  state is expressed as:

$$A_i = \sum_{r=1}^m B_{ir} Q_r^0 \exp(-\lambda_r t) \quad (4.30)$$

Where the  $Q_r^0$  are coefficients in the linear combination, which are determined from the initial conditions.

When the equilibrated system is probed by high resolution EPR, only one paramagnetic state (Co<sup>II</sup>-substrate radical pair) is detected at  $SNR=1300$ . This suggests that the energy profile of Co<sup>II</sup>-5'-deoxydenosyl radical pair is much higher comparing to other states. From Scheme 4.1, this corresponds to the condition:  $\Delta G_2, \Delta G_3 \gg \Delta G_1, \Delta G_4$ . This observation direct leads to the following inequality:

$$k_{21}, k_{34} \gg k_{12}, k_{43} \quad (4.31)$$

The migration of the C5'-methylene radical center from the  $\beta$ -face of cobalamin to the substrate binding site is thought not to be a rate limiting step comparing to the Co-C bond cleavage and HT1 steps from isotope studies. The following inequality is concluded:

$$k_{23}, k_{32} \gg k_{12}, k_{43} \quad (4.32)$$

In all the time course of Co<sup>II</sup>-substrate radical pair growth, only one kinetic phase is observed in the whole temperature range from 234 – 246 K. We are interested to interpret this single kinetic phase, which is one of the eigenvalues of the secular equation, in terms of these microscopic rates. This specific eigenvalue is named as  $\lambda_{obs}$ , which, it is assumed, will not be comparable with the fast microscopic rates:  $k_{21}$ ,  $k_{34}$ ,  $k_{23}$  and  $k_{32}$ . Therefore, the following expression holds:

$$k_{21}, k_{34}, k_{23}, k_{32} \gg \lambda_{obs} \quad (4.33)$$

The secular equation leading to the solution of  $\lambda_{obs}$  could be simplified under this approximation, as follows:

$$\begin{vmatrix} k_{12} - \lambda_{obs} & -k_{21} & 0 & 0 \\ -k_{12} & k_{21} + k_{23} & -k_{32} & 0 \\ 0 & -k_{23} & k_{32} + k_{34} & -k_{43} \\ 0 & 0 & -k_{34} & k_{43} - \lambda_{obs} \end{vmatrix} = 0 \quad (4.34)$$

Solving this equation yields one non-zero eigenvalue:

$$\lambda_{obs} = \frac{k_{12}k_{23}k_{34} + k_{32}k_{43}k_{21}}{k_{21}k_{32} + k_{21}k_{34} + k_{23}k_{34}} = k_{obs} \quad (4.35)$$

Since the population of different states is determined by its energy profile, the equilibrated population ration between  $A_4$  (Co<sup>II</sup>-substrate radical pair) and  $A_I$  (ternary complex) is expressed as:

$$\frac{[A_4]_{\infty}}{[A_1]_{\infty}} = \frac{[A_2]_{\infty}}{[A_1]_{\infty}} \frac{[A_3]_{\infty}}{[A_2]_{\infty}} \frac{[A_4]_{\infty}}{[A_3]_{\infty}} = \frac{k_{12} k_{23} k_{34}}{k_{21} k_{32} k_{43}} = \frac{[A_4]_{\infty}}{[A_{Tot}] - [A_2]_{\infty} - [A_3]_{\infty} - [A_4]_{\infty}} \quad (4.36)$$

High resolution EPR yields:

$$[A_2]_{\infty}, [A_3]_{\infty} \ll [A_4]_{\infty} \quad (4.37)$$

Substitution of Inequality 4.37 into Eq. 4.36 and combing with the definition of experimental observable,  $\nu$ , leads to the following:

$$\frac{k_{12} k_{23} k_{34}}{k_{21} k_{32} k_{43}} = \frac{[A_4]_{\infty}}{[A_{Tot}] - [A_2]_{\infty} - [A_3]_{\infty} - [A_4]_{\infty}} \approx \frac{[A_4]_{\infty}}{[A_{Tot}] - [A_4]_{\infty}} = \frac{\nu}{1 - \nu} \quad (4.38)$$

Substitution of Eq. 4.38 into Eq. 4.35 leads to:

$$k_{12} = \nu \left[ 1 + \frac{k_{21}}{k_{23}} + \frac{k_{21} k_{32}}{k_{23} k_{34}} \right] k_{obs} \quad (4.39)$$

For all the microscopic rate constants in Equation 39, only  $k_{34}$  is substrate hydrogen isotope dependent.

From experimental results on the temperature dependence of substrate hydrogen kinetic isotope effect and the equilibrium isotope effect, the following result is obtained:

$$\frac{k_{obs}^H(T_{low})v^H(T_{low})}{k_{obs}^D(T_{low})v^D(T_{low})} = 0.72 + a \quad (4.40)$$

where  $T_{low}$  is any temperature between 234 and 246 K and  $a$  is the uncertainty. From the standard deviation from experimental results, the uncertainty in Eq. 4.40 could be estimated as:

$$0 < a < 0.3 \quad (4.41)$$

Combine Eqs. 4.39 and 4.40:

$$\frac{1 + \frac{k_{21}(T_{low})}{k_{23}(T_{low})} + \frac{k_{21}(T_{low})}{k_{23}(T_{low})} \frac{k_{32}(T_{low})}{k_{34}^D(T_{low})}}{1 + \frac{k_{21}(T_{low})}{k_{23}(T_{low})} + \frac{k_{21}(T_{low})}{k_{23}(T_{low})} \frac{k_{32}(T_{low})}{k_{34}^H(T_{low})}} = 0.72 + a \quad (4.42)$$

Similar to three-state, two-step model, we define a new parameter  $R$  as:

$$R = \frac{k_{21} k_{32}}{k_{23} k_{34}} \quad (4.43)$$

Then  $k_{12}$  could be related to experimental observables as:

$$k_{12} = v \left( 1 + \frac{k_{21}}{k_{23}} + R \right) k_{obs} \quad (4.44)$$

From Eq. 4.44, Eq. 4.42 is reorganized as:

$$\frac{1 + \frac{k_{21}(T_{low})}{k_{23}(T_{low})} + R^D(T_{low})}{1 + \frac{k_{21}(T_{low})}{k_{23}(T_{low})} + R^H(T_{low})} = 0.72 + a \quad (4.45)$$

Based on Reed and coworker's kinetic isotope effect results at ambient temperature:

$$\frac{k_{obs}^H(298K)}{k_{obs}^D(298K)} = 3.1 \quad (4.46)$$

All the EAL active sites will be occupied by Co<sup>II</sup>-substrate radical pair at room temperature:

$$\frac{v^H(298K)}{v^D(298K)} = 1 \quad (4.47)$$

Substitution of Eqs. 4.46 and 4.47 into Eq. 4.39 leads to the following:

$$R^D(298K) = 2.1 + 2.1 \frac{k_{12}(298K)}{k_{23}(298K)} + 3.1R^H(298K) > 3.1R^H(298K) \quad (4.48)$$

Since  $R^D/R^H = k_{34}^H/k_{34}^D$  represents the intrinsic isotope effect in HT1, the temperature dependence of the isotope effect on general hydrogen transfer guarantees another inequality as:

$$\frac{R^D(T_{low})}{R^H(T_{low})} > \frac{R^D(298K)}{R^H(298K)} > 3.1 \quad (4.49)$$

Substitution of Inequity 4.49 into Eq. 4.45 leads to the following:

$$0.72 + a = \frac{1 + \frac{k_{21}(T_{low})}{k_{23}(T_{low})} + R^D(T_{low})}{1 + \frac{k_{21}(T_{low})}{k_{23}(T_{low})} + R^H(T_{low})} > \frac{1 + \frac{k_{21}(T_{low})}{k_{23}(T_{low})} + 3.1R^H(T_{low})}{1 + \frac{k_{21}(T_{low})}{k_{23}(T_{low})} + R^H(T_{low})} > 1 \quad (4.50)$$

By rearranging Inequality 4.50 and using the Inequality 4.41, the  $R^H(T_{low})$  could be set with an upper limit as:

$$R^H(T_{low}) < \frac{a-0.28}{2.38-a} \left[1 + \frac{k_{21}(T_{low})}{k_{23}(T_{low})}\right] < 0.01 \left[1 + \frac{k_{21}(T_{low})}{k_{23}(T_{low})}\right] \quad (4.51)$$

Comparing the limit from Inequality 4.51 with the results from three-state, two-step mechanism, the difference in calculating  $k_{12}$  from experimental observables is contributed by the positive  $k_{21}/k_{23}$  and  $R$  terms. The deviation on  $k_{12}$  derived from three-state, two-step model could be assessed by two aspects, compared with four-state three-step model: (1)  $k_{12}$  is underestimated, (2) in the  $\ln k_{12}/T$  vs.  $1/T$  plot,  $k_{12}$  has a more flat slope and smaller intercept. The decreased slope and intercept imply a lower activation enthalpy and entropy value for  $k_{12}$ .

If it is true that the Co-C bond cleavage is the rate-limiting step in the temperature range from 234 – 246 K, the transition state of C5'-deoxydenosyl radical migration step may possess a lower energy profile than the Co-C bond cleavage transition state. In this case,  $k_{21}/k_{23}$  will be  $\ll 1$ , which yields the upper limit and lower limit on  $k_{12}$  as:

$$k_{12} = v \left(1 + \frac{k_{21}}{k_{23}} + R\right) k_{obs} < v \left(1 + 1.01 \frac{k_{21}}{k_{23}} + 0.01\right) k_{obs} \quad (4.52)$$

This suggests that by using the lower limit of  $k_{12}$ , which is  $vk_{obs}$ , to represent the Co-C bond cleavage rate, the error is controlled to within  $(R+k_{21}/k_{23})$ .

Therefore, at low temperature, if diffusion of the C5'-deoxydenosyl radical to the substrate bidding site is not rate limiting, it is not necessary to adopt the four-state, three-step reaction mechanism.

## 4.6 Solvent Effect Study

The solvent effect study is aimed to an examining the impact of 41% DMSO/water solution on the hydrophobic/hydrophilic property of the solvent, in comparison with aqueous solution. This solvent property is commonly quantified by the parameter partition coefficient<sup>138</sup> (P) as a ratio of the concentrations of a compound in the two phases of a mixture of two immiscible solvents at equilibrium. We employ shake-flask plus UV-visible method<sup>139</sup> to determine the partition coefficient of the hexane/cryosolvent and hexane/aqueous solution by using the same solute methyl-p-benzoquinone, respectively. Figure 4.13 presents the experimental results.

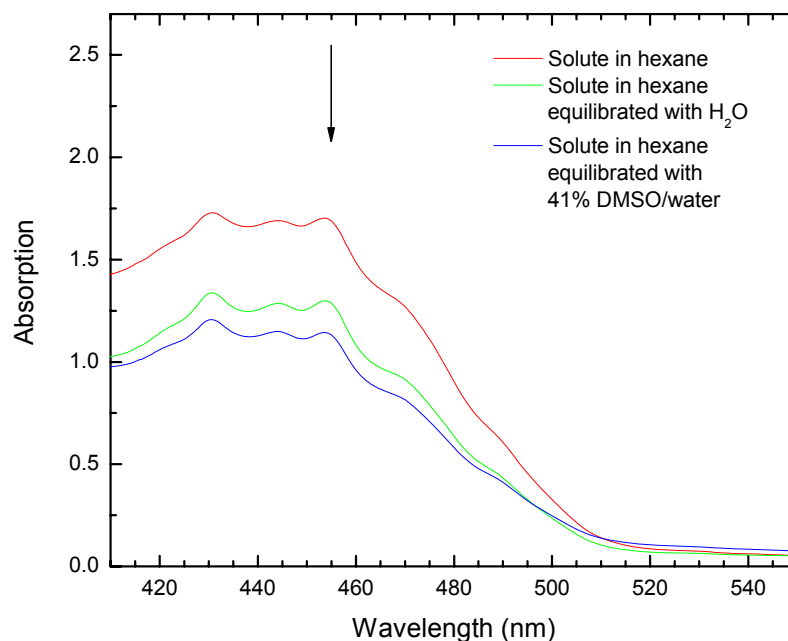


Figure 4.13: UV-visible absorption spectrum for the solvent effect studies with methyl-p-benzoquinone. The arrow points to the peak position at 453.6 nm, where the Abs(methyl-p-benzoquinone in hexane)= 1.70, Abs(methyl-p-benzoquinone in hexane equilibrated with H<sub>2</sub>O)=1.25 and Abs(methyl-p-benzoquinone in hexane equilibrated with 41%DMSO/water)=1.14.

The partition coefficient is often expressed in its logarithm form, as given Eq. 4.53.

$$\log P_{A/B} = \log\left(\frac{[solute]_A}{[solute]_B}\right) \quad (4.53)$$

From Beer-Lambert's law in optical spectroscopy, which states that the solute concentration vs. UV-Visible absolute absorption is linear over, substitution of the absorption peak amplitude at 453.6 nm in Figure 4.13 leads to the following calculations as:  $\log P(\text{hexane}/\text{H}_2\text{O}) = 0.58$  and  $\log P(\text{hexane}/\text{cryosolvent}) = 0.48$ . These results demonstrate that the 41% DMSO/water cryosolvent can extract 20% more polar solute from the apolar hexane than aqueous solution at ambient temperature. Considering the partition coefficient generally increases upon temperature decreasing, the cryosolvent effect on kinetics, especially on the entropy due to the hydrophobic contribution, is minimized relatively to aqueous solution at 240 K, around which we carried out the kinetic study.

## 4.6 Concluding Remarks

Figure 4.14 shows a schematic diagram of the enthalpic and entropic contribution to the Co-C bond cleavage in aqueous solution<sup>131</sup> (uncatalyzed reaction; denoted "soln") and in EAL (catalyzed reaction) at  $T=298$  K. In solution, the large value of  $\Delta H_{\text{soln}}^\ddagger$  ( $32 \pm 1$  kcal/mol) dominates the  $\Delta G_{\text{soln}}^\ddagger$  ( $30 \pm 1$  kcal/mol), because of the relatively small positive value of  $T\Delta S_{\text{soln}}^\ddagger$  ( $2.0 \pm 0.3$  kcal/mol). Comparison of the solution and EAL contributions shows that the values of  $\Delta H_{12}^\ddagger$  and  $\Delta H_{\text{soln}}^\ddagger$  are equal. Therefore, the protein

does not use enthalpic factors to catalyze Co-C bond cleavage. Instead, the catalysis of Co-C bond cleavage in EAL arises almost entirely from the large, favorable activation entropy. The relatively small  $\Delta S_{\text{soln}}^{\ddagger}$  value for the uncatalyzed reaction, and the expected smaller extrinsic and intrinsic degrees of freedom of the protein-enclosed 5'-deoxyadenosyl and cob(II)alamin, suggest that the activation entropy contribution originates from the protein ( $T\Delta S_{\text{prot}}^{\ddagger} \geq 16.4 \pm 1.5$  kcal/mol), possibly with additional solvent effects.

The identification of dominant activation entropy contributions represents a paradigm shift for the mechanistic basis of Co-C bond cleavage catalysis in B<sub>12</sub> enzymes. The molecular mechanism of Co-C bond cleavage catalysis has eluded four decades of proposals based on experimentally or theoretically motivated enthalpic mechanisms, including destabilization of the Co-C bond through (1) *trans*-<sup>8-10</sup>, (2) *cis*-axial ligand effects<sup>9</sup>, (3) corrin ring flexure<sup>1,11,12</sup>, and stabilization of the 5'-deoxyadenosyl group following cleavage<sup>140</sup>. Recent spectroscopic studies, including FT-Raman<sup>27</sup>, Resonance Raman<sup>28</sup> and UV-visible (unpublished data), have shown that AdoCbl is not significantly distorted in the enzymes, relative to solution. In EAL, substrate binding in the ternary complex also does not induce UV-visible spectral changes, relative to holo-EAL, that would provide evidence for significant structural distortions of the bound AdoCbl.

The specification of the molecular mechanism of Co-C bond cleavage in EAL entails understanding the origin of  $\Delta S_{12}^{\ddagger}$ . The large magnitude of  $\Delta S_{12}^{\ddagger}$  may be difficult for the protein itself to realize, and suggests an association with changes in the interaction of the aqueous solvent with the protein. Large entropy changes are associated with changes in aqueous solvent accessibility of apolar regions of the protein, primarily on the

surface.<sup>14,22</sup> Liberation of water associated with the apolar surface results in an increase in entropy.<sup>141,142</sup> Alternatively,  $\Delta S_{12}^{\ddagger}$  may arise from the dynamical effect of coupling the motions of the protein that are associated with bond cleavage to the solvent hydration layer dynamics. Thus, an increase in the number of accessible states in the transition state for Co-C cleavage in EAL, owing to multiple hydration layer configurations, could also increase  $\Delta S_{12}^{\ddagger}$ .

Our kinetic study focused on a covalent bond breaking event, which is catalyzed by an enzyme. The huge rate enhancement is long and intuitively thought to be caused by enthalpic contributions. Our study unraveled a dominant entropic contribution in the bond cleavage, which is very counterintuitive and pushing cutting edge inquiries into factors that govern ligand binding, and single molecule protein fluctuations. Therefore, the commonly held view that high affinity interactions are necessarily energetically dominated by specific structural (enthalpic) interactions must be relaxed to include the structural dynamics and heterogeneity that contributes to conformational protein entropy.

A large positive entropy has been shown in a couple of coenzyme B<sub>12</sub>-dependent enzyme including methylmalonyl-CoA mutase (MCM)<sup>14</sup> and ribonucleotide triphosphate reductase (RTPR)<sup>22</sup>. However, extraction of “pure” activation parameters for Co-C bond cleavage is obscured by treating the reaction by a concerted reaction mechanism, in which the Co-C bond cleavage and HT1 are treated as a single step. This has been adopted, due to the limitation of the experimental method. In these kinetic studies, the observed Co<sup>II</sup> state accumulation rate (represented  $k_{obs}$  in Scheme 3.2) reflects an extra substrate/cofactor binding step since the initial state is not the ternary complex. Through studies on the dependence of  $k_{obs}$  on substrate/cofactor concentration, a forward first-

order reaction rate constant is obtained, which corresponds to “ $v k_{obs}$ ” under substrate saturation conditions. This is treated to represent the Co-C bond cleavage rate constant ( $k_f$ ). Comparing with Equation 4.15, the ratio between the Co-C bond cleavage rate ( $k_{12}$ ) from the three-state, two-step mechanism and this forward rate ( $k_f$ ) is  $1+r$ . As shown in the previous calculation,  $r$  could be as large as 9 at 298 K, which means that the concerted mechanism may underestimate the Co-C bond cleavage rate by an order of magnitude. We have also shown that the coupling term  $r$  generally decreases dramatically upon temperature decrease (from 9 at 298 K to less than 0.01 at 240 K) due to the fact that Co-C bond cleavage has a larger entropy contribution than HT1 step. Therefore, in the Eyring plot of  $\ln k_{12}/T$  vs.  $1/T$ , the linear relation for the concerted mechanism has a decreased slope, owing to neglect of the contribution from  $r$ . Based on this analysis, the concerted mechanism underestimate both the  $\Delta H_{12}^\ddagger$  and  $\Delta S_{12}^\ddagger$ .

Our 41% DMSO/water system gives us a unique ability to investigate the Co-C bond cleavage in EAL and this system has potential to be applied to other members in the conenzyme B<sub>12</sub>-dependent enzyme superfamily, in which all active site containing large subunits are characterized by the robust  $\alpha_8\beta_8$ -barrel structure. Our system also offers us the ability to further investigate the molecular dynamical origins of the entropy, so that we can build it into rationally designed and constructed molecular systems, with applications as diverse as photosynthetic catalysts and drug binding.

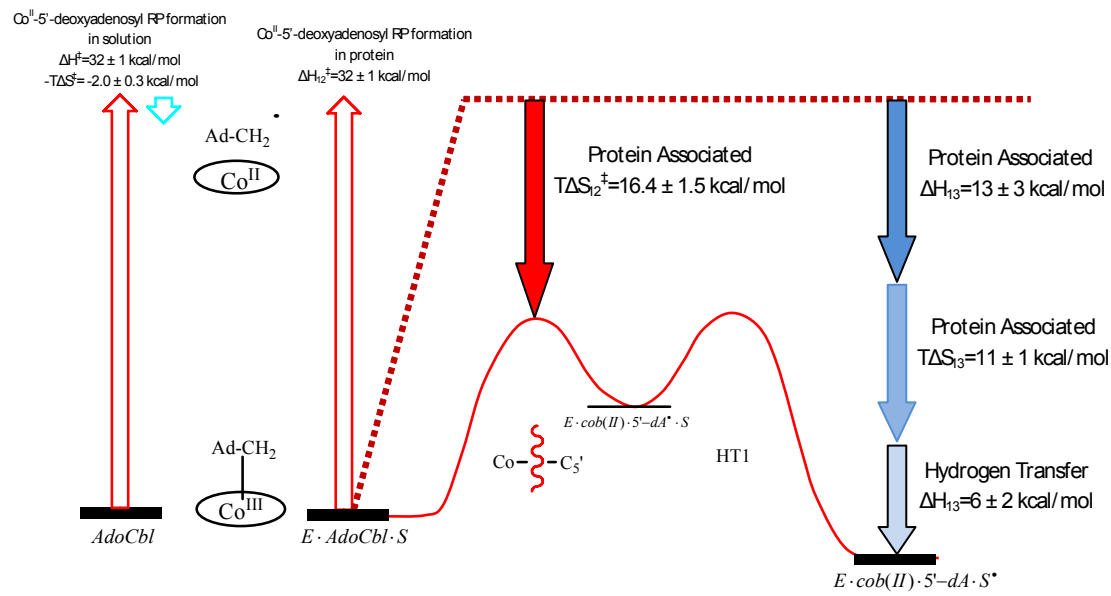


Figure 4.14: Schematic diagram of the enthalpic and entropic contribution to the Co-C bond cleavage in aqueous solution and in EAL at  $T=298 \text{ K}$ .

**Chapter Five**

**Optical Absorption Studies of**

**the Ternary Complex**

The kinetically arrested EAL·B<sub>12</sub>·substrate ternary complex<sup>26</sup> offers a key to answer fundamental questions in the mechanism of the coenzyme B<sub>12</sub>-dependent enzymes. We took advantage of this system, and demonstrated that the >10<sup>11</sup> fold rate enhancement<sup>4-6</sup> on the Co-C bond cleavage rate in the presence of enzyme, compared to the cleavage rate of free AdoCbl in aqueous solution<sup>2</sup>, originates from an entropic effect, as stated in Chapter Four. Another application of the ternary complex is in testing the strain hypothesis<sup>4,5</sup>, in which the enzyme is proposed to destabilize the Co-C bond ground state by imposing chemomechanical stress. In order to test this hypothesis, our experimental design is inspired by the fact that the electronic absorption (Abs) spectrum of coenzyme is sensitive to the  $\sigma$ -donation strength of the alkyl ligand. This shown by the different Abs spectra of MeCbl, AdoCbl and CNCbl, which is caused by the difference in  $\sigma$ -donation from the alkyl ligand to the Co center and the consequent variation in destabilization for all Co 3*d* orbitals.<sup>29</sup> By capturing the Abs spectra from free AdoCbl in solution, AdoCbl bound in EAL and AdoCbl bound in the ternary complex, the ligand stress may be visualized form the Abs spectrum.

## 5.1 Instrument Design and Setup

Low temperature UV-visible Abs experiments are performed on a Shimadzu UV-1601 optical bench spectrophotometer with a Shimadzu constant temperature 2 cell sample holder. Dry nitrogen gas serves as the cooling mediator by running through a stainless-steel heat exchanging coil, which is immersed inside liquid nitrogen. A home-made temperature controller, which is based on a 1/16 DIN MICROMEGA<sup>®</sup> autotune

PID temperature/process controllers (Omega part number CN77000), heats the cold nitrogen gas to the desired temperature by feeding the electric current through an electric coil heater embedded along the nitrogen gas pathway. The amount of current is determined by the temperature reading from a T-band thermocouple (Omega part number 5STRC-TT-T-30-36), temperature setting point and PID parameters. After heating, the nitrogen gas passes through the Shimadzu 2 cell constant temperature sample holder to cool down a quartz cuvette (Hellma QS 282 1.000 ml), where the sample is held.

Since temperature below 230 K is desired to allow the formation of the kinetically arrested ternary complex, an air-tight adapter is required to eliminate the moisture condensation along the optical path in order to guarantee the accuracy of the absolute Abs value. The sample volume for the UV-visible Abs experiment is around 1 ml, which is 5 times more than the sample volume in EPR studies. Therefore, this adapter should also serve to reduce the temperature inhomogeneity over the whole sample length ( $\approx 3$  cm).

Based on these design expectations, an aluminum adapter, which seals the sample cuvette and its holder from ambient air, was home-designed and home-built. In this adapter, the pre-cooled nitrogen gas is used as purge gas inside the adapter after passing through the sample holder. Two heated quartz windows provide  $>90\%$  transmission from 250 nm to 2500 nm at temperatures down to 230 K. The top of the adapter is covered by one piece of removable glass for easy sample access. To further reduce the temperature gradient inside the sample, a quartz cuvette (Hellma QS 282 1.000 ml) is employed to maximize the thermal transmission due to the fact that the thermal conductivity of quartz is one order of magnitude greater than glass.<sup>143,144</sup>

The PID parameters, heater power and N<sub>2</sub> gas flow rate of the home-made cooling system are carefully adjusted to minimize the following factors: (1) the temperature fluctuation at 230 K; (2) temperature undershoot during the sample cooling process; (3) the temperature settling time. After tuning, a set of parameters are selected, which assures that the temperature decreasing and settling process from 298 K to 230 K takes less than 30 minutes with an undershoot of  $\leq 5$  K. The temperature stability at 230 K is  $\pm 1.5$  K over the 2-hour data acquisition time interval.

## 5.2 Temperature-dependence of AdoCbl UV-visible Spectrum

The first application of this home-designed and home-built constant low temperature sample holder is to study the temperature dependence of the AdoCbl Abs spectrum. The choice of the temperature point, at which the UV-visible spectroscopy is applied on the free AdoCbl in DMSO/water cryosolvent, is confined by the available stable temperature points that can be provided by the system, which are 298 K, 247 K and 231 K.

Figure 5.1 shows the Abs spectra of AdoCbl at different temperature points from 250 to 700 nm. All these spectra represent the unique UV-visible spectrum with well resolved  $\alpha/\beta$  bands and spread  $\gamma$  band as stated in Chapter One.

To make comparison between these spectra, we select the peak position of the  $\alpha$  band at around 525 nm as the evaluating parameter. The determination of the exact peak position is by 2<sup>nd</sup> order polynomial fit of the  $\alpha$  band.

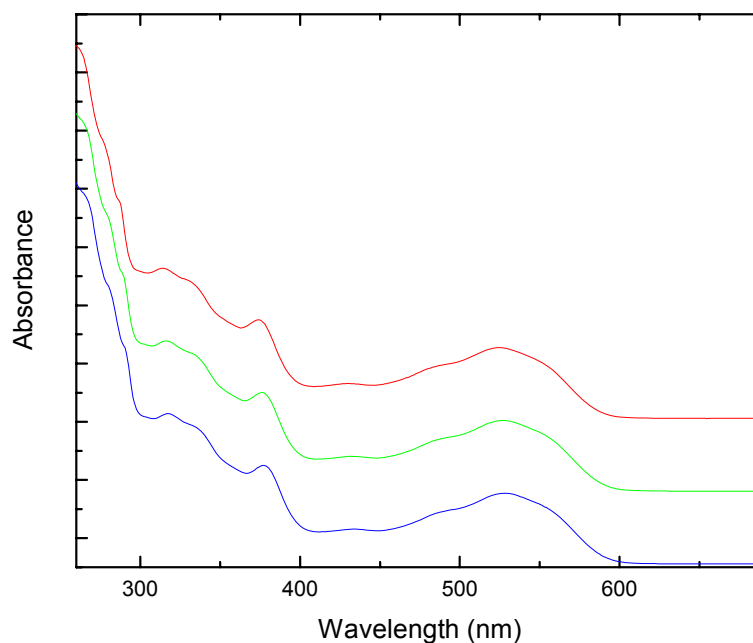


Figure 5.1: UV-visible Abs spectrum of AdoCbl in 41% DMSO/water cryosolvent at different temperatures. Bottom (blue) spectrum is collected at 231 K, middle (green) spectrum is collected at 247 K, top (red) spectrum is collected at 295 K.

Table 5.1: Values of  $\alpha/\beta$  band peak position for AdoCbl Abs spectrum at different absolute temperatures. Values represent the average of at least three separate experiments, and the corresponding standard deviation.

Temperature (K)	Peak Position (nm)	Standard Deviation (nm)
295	525.0	0.5
247	527.2	0.3
231	528.3	0.4

The curve fitting was carried out by the program OriginPro 7.5 (OriginLab Corporation, Northampton, MA), with the least-squares fitting method.

Figure 5.2 shows the  $\alpha/\beta$  band peak position plotted as a function of absolute temperature. The averaged values of peak position at different temperatures and

corresponding standard deviations, which represent at least three separate determinations, are collected in Table 5.1. The peak wavelength of  $\alpha/\beta$  band generally exhibits a blue-shift to shorter wavelengths as the temperature increases. The fitting of the data yield a linear dependence, which has been understood in terms of temperature-dependent dilatation of the lattice and electron lattice interaction.<sup>145</sup> The slope of the temperature dependency of AboCbl is estimated as 0.05 nm/K from the linear data fitting in Figure 5.2.

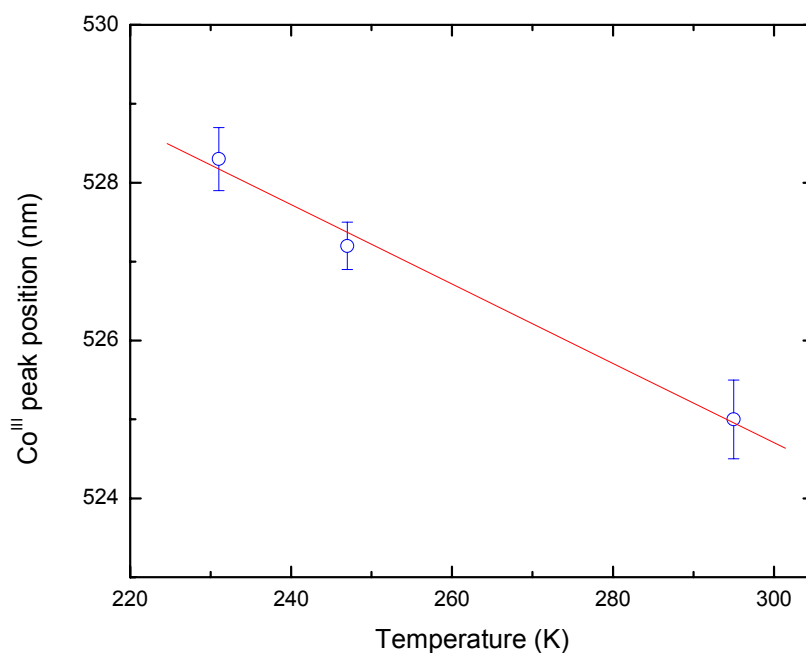


Figure 5.2: Temperature dependence of the  $\alpha/\beta$  band peak of AdoCbl from ambient temperature to 231 K. This spectrum reflects the average of three different runs. Linear fitting parameters: intercept = 540, slop = -0.05,  $R^2=0.996$ .

A potential application of this temperature dependence is to utilize AdoCbl as a noncontact temperature probe, which is similar to the luminescence-based quantum dots (QD)<sup>146,147</sup>. The spectral shift of a single quantum dot was reported to be 0.1 nm/K, which is comparable with the Abs shift for AdoCbl. Li and coworkers reported that about 1200

particles are needed to achieve 1 K precision in optical temperature readout by using QDs.<sup>146</sup> This requirement of large amount of particles is due to a distribution in the size and shape of individual wet-chemistry-synthesized QD.<sup>148,149</sup> Since AdoCbl has literally zero standard deviation on size and shape, the number of particles to achieve the same temperature resolution will be reduced.

### 5.3 Ternary Complex Preparation Protocol

The ternary complex preparation protocol for UV-visible Abs study is similar to the one for EPR experiments except that the percentage of DMSO in the cryosolvent is slightly increased to a final value of 49% DMSO/water (v:v) proportion. This modification is targeted to increase the transparency of the cryosolvent at 230 K for optical study. From the pioneering research in Figure 2.14, this concentration variation will not impede the enzyme's ability to react and form the  $\text{Co}^{\text{II}}$ -substrate radical pair. To achieve the EAL·B<sub>12</sub>·substrate ternary complex, the first step is to prepare holoenzyme in a cacodylate buffered 41% DMSO/water cryosolvent inside an EPR tube by following the ternary complex preparation protocol that is developed in Chapter Two. Then the holoenzyme is transferred to a pre-cooled cuvette, which is filled with additional DMSO/water cryosolvent, in the Shimadzu 1601 at 247 K. In the last step, excess substrate, (S)-2-aminopropanol, is mixed with holoenzyme at 230 K. At this stage, the volume of the substrate added to the holoenzyme is less than 1% of the total solvent volume. The whole procedure (detailed explanation in the Appendix) is performed under a dim red safe light.

## 5.4 UV-visible Spectrum of the Ternary Complex and Holoenzyme

In the following paragraph, an experiment is described to test the strain hypothesis<sup>4,5</sup>, which states that protein would exert significant mechanochemical strain on the Co-C bond to destabilize its ground state energy, and therefore facilitate the hemolytic cleavage process. The coenzyme B<sub>12</sub>-dependent enzymes have been described as the “last bastion”<sup>140</sup> for strain mechanisms in enzymology.<sup>4,9</sup>

In our experiment, UV-visible Abs spectroscopy is employed as the primary probe for detecting any spectrum variation caused by this strain, by the comparison between the ternary complex, the holoenzyme and free cofactor AdoCbl samples. These three samples are prepared separately, as explained below.

One 1 ml liquid sample, which contains EAL·B<sub>12</sub>·substrate ternary complex, is prepared in a quartz cuvette (detailed procedure is listed in the Appendix) at 230 K. UV-visible Abs spectroscopy is sequentially acquired on this sample in the Shimadzu 1601 spectrometer with the Shimadzu constant temperature 2 cell sample holder. The stabilized temperature is achieved by using a home-designed and home-made cooling system. To increase the *SNR*, the sample scan interval is set to be 0.1 nm and 3 scans are accumulated.

The background is obtained by using a separate 1 ml liquid sample, which contains EAL·substrate binary complex without the cofactor AdoCbl. The preparation of the background sample is the same as the protocol in the Appendix, except that AdoCbl is

not added in the whole process. The sample scan interval is also set to 0.1 nm and 3 scans are accumulated.

Similar to the data collection procedure on the ternary complex sample, UV-visible Abs spectra are performed on holoenzyme and free AdoCbl sample individually.

The results are presented in Figure 5.3. By comparison of the spectrum shapes, the spectrum from ternary complex does not contain the  $\text{Co}^{\text{II}}$  signal<sup>66</sup>. This yields a consistent conclusion with EPR studies, that the ternary complex is under kinetic arrest before the Co-C bond cleavage step.<sup>26</sup> To make quantitative comparison between these spectra, the peak position of the  $\alpha/\beta$  band around 525 nm is again selected as the evaluating parameter. The determination of this parameter is by 2<sup>nd</sup> order polynomial fit of the  $\alpha/\beta$  band. Three individual runs have been carried out with the averaged value and standard deviation shown in Table 5.2. To better visualize the results, a bar plot is provided in Figure 5.4 based on the experimental results in Table 5.2.

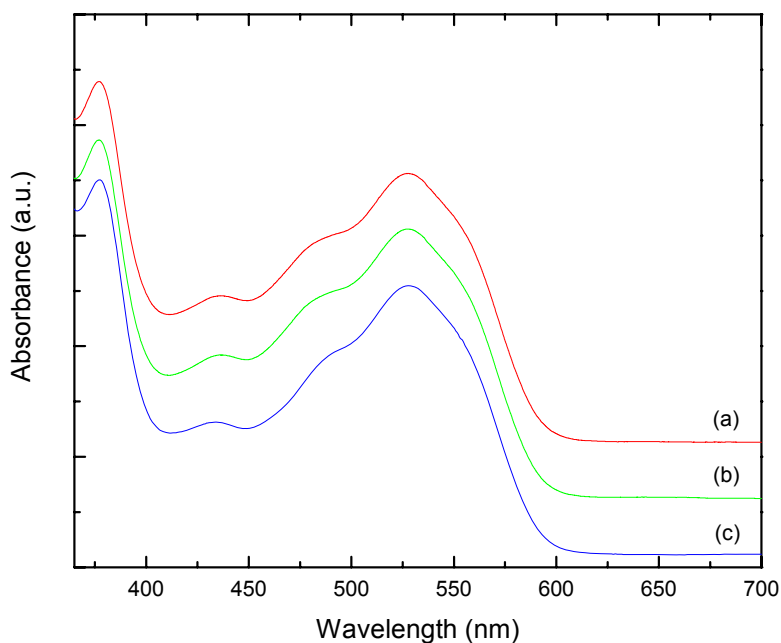


Figure 5.3: UV-visible Abs spectra comparison between (a) ternary complex, (b) holoenzyme and (c) free AdoCbl. All the spectra are collected at 230 K. The wavelength increment is 0.1 nm from 350 nm to 700 nm.

Table 5.2: Values of  $\alpha/\beta$  band peak position for the UV-visible Abs spectrum on ternary complex, holoenzyme and AdoCbl at 230 K. Values represent the average of at least three separate experiments, and the corresponding standard deviation.

Sample	$\alpha/\beta$ band peak position (nm)	Standard Deviation (nm)
<b>Ternary Complex</b>	527.9	0.3
<b>Holoenzyme</b>	527.7	0.2
<b>AdoCbl</b>	528.3	0.3

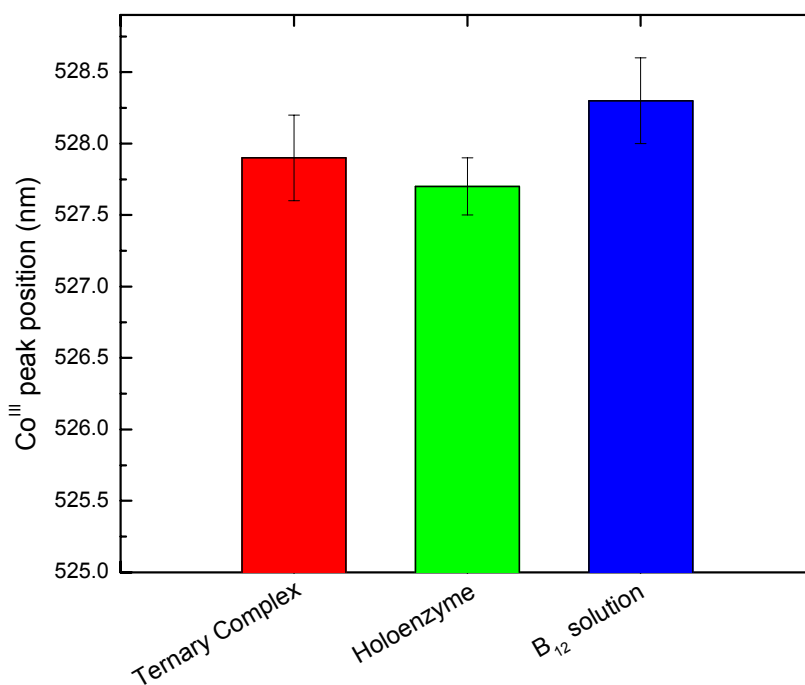


Figure 5.4: Bar plot for the  $\alpha/\beta$  band peak position for the UV-visible Abs spectrum on ternary complex, holoenzyme and AdoCbl at 230 K. Values represent the average of at least three separate experiments, and the corresponding standard deviation.

The  $\alpha/\beta$  band peak position of bound AdoCbl in holoenzyme shows a 0.6 nm blue-shift to lower wavelength compared to free AdoCbl at 230 K. This shift is consistent with the results found at room temperature (W. Robertson and K. Warncke, unpublished result) with holoenzyme and free AdoCbl in aqueous solution. This small 0.6 nm blue-shift exhibits large contrast to the 5 nm peak position shift between MeCbl ( $\alpha/\beta$  band  $\lambda_{\max}=520$  at 298 K) and AdoCbl ( $\alpha/\beta$  band  $\lambda_{\max}=525$  at 298 K),<sup>29</sup> each of which has a bound dissociation energy (BDE) as 36 kcal/mol<sup>150-152</sup> and 31 kcal/mol<sup>3,153</sup> separately. For a rough estimation, the observed spectrum shift reflects a smaller BDE difference between bound and free AdoCbl than the case between MeCbl and AdoCbl, which is 5 kcal/mol. This peak shift could also be compared with the thermal induced  $\alpha/\beta$  band peak shift in Figure 5.2, which corresponds to a thermal energy change of at least one order-of-magnitude less than 1 kcal/mol (calculated from *RAT*). Therefore, this 0.6 nm shift could not be related to a ground state destabilization, which is on the order of 14-16 kcal/mol<sup>5</sup> in coenzyme B<sub>12</sub>-dependent enzymes, from the contribution from the cofactor binding. From the Abs spectrum comparison, we conclude that the EAL would not significantly perturb the corrinoid structure, which implies that the Co-C bond is unaffected after the cofactor binding. This result directly questions the *trans*-effect hypothesis<sup>154,155</sup>, in which the  $\alpha$ -face 5,6-dimethylbenzimidazole(DMB) is proposed to mediate the Co-C bond cleavage in order to explain the catalytic effect of coenzyme B<sub>12</sub>-dependent enzymes. Since the hydrogen bonding network of the AdoCbl largely relies on the DMB group,<sup>30</sup> our result suggests that the *trans*-effect would not be the major contributor to facilitate the Co-C bond cleavage process.

The absence of a significant *trans*-effect in EAL is consistent with many independent theoretical and experimental studies on AdoCbl. For example, the UV-visible Abs and DFT calculation from Brunold's group have demonstrated that the strength of the Co-C bond is largely unperturbed by removal of the DMB base from AdoCbl, which generates the corresponding Cbi that binds a water molecule in the  $\alpha$ -axial position.<sup>29</sup> Mayer's computational analysis also showed that the Co-C bond order decreases up to 1% by substituting DMB base with a water molecule.<sup>156-158</sup> Supporting results are also found on Resonance Raman and IR vibrational data for alkylcobalamins that reveal negligible changes in the Co-C bond strength upon substitution of the lower axial base by a water molecule.<sup>27</sup> Thus, all these results plus our finding from UV-visible Abs spectrum show that the *trans*-effect is unlikely to account for the  $>10^{11}$  fold rate enhancement on the Co-C bond cleavage rate.

The *cis*-effect is another proposed strain hypothesis<sup>4,9</sup>, in which the protein interacts with the bound Ado group to exert chemomechanical strain to the Co-C bond. Our Abs experimental results also challenge this *cis*-effect hypothesis by showing a small energy perturbation to the corrinoid structure after the enzyme binding. This observation is again supported by independent resonance Raman studies of methylmalonyl-coenzyme A mutase, which shows that the corrin vibrational modes that are responsive to the ring conformation are unaffected by substrate analog binding.<sup>159</sup>

The last but not least member of the ground state destabilization hypothesis is the substrate binding trigger mechanism, which was proposed by Evans and co-workers from an X-ray crystallography study in the case of methylmalonyl-CoA mutase.<sup>57,160</sup> In such a hypothesis, a large conformational change is induced by substrate binding to destabilize

the Co-C bond. This hypothesis was thought to be only applicable to enzymes that bind large substrate, such as CoA derivatives, because of the large binding energy required to initiate the enzyme conformational change. However, Toraya's group proposed a similar mechanism for the diol dehydratases, which bind a much smaller substrate as 1,2-dihydroxyprpane, by showing the crystal structure of the substrate-free and inhibitor-bound form.<sup>54</sup> This research revealed that upon the substrate binding, the Co-C bond is tilted by relatively small angle of 3°, which leads to negligible angular distortion of the coenzyme. Due to the fact that CNCbl, which is a cofactor analog, that is used to avoid the cleavage of the Co-C bond in AdoCbl during X-ray irradiation in the crystallography study, this hypothesis remains questionable.

Comparison of the AdoCbl  $\alpha/\beta$  band peak position in holoenzyme and ternary complex in Figure 5.2 reveals a 0.2 nm red-shift that is barely resolved from the statistical error between different runs. This small shift does not support the substrate binding trigger mechanism and is consistent with the peak shift trend found at room temperature when substrate analog/inhibitor is bound to the enzyme (W. Robertson and K. Warncke, unpublished result). This experimental result is also consistent with the independent resonance Raman measurements by Spiro and co-workers.<sup>28,161,162</sup> They have explored the influence of protein binding on the vibrational spectrum of the corrin ring and the effect of the axial nitrogenous ligand on the vibrational frequency of the Co-C bond. A small frequency shift from 530  $\text{cm}^{-1}$  for AdoCbl in free solution to 524  $\text{cm}^{-1}$  for AdoCbl bound to methylmalonyl-CoA mutase is observed, but in the presence of bound substrate or product the vibration returns to 530  $\text{cm}^{-1}$ .

All of these UV-visible Abs experiments lead to the same conclusion as that any additional AdoCbl ground state destabilization upon substrate binding would be at most comparable to the change caused by the cofactor binding in the EAL active site.

## **5.5 Concluding Remarks**

This section described a careful design of the low temperature UV-visible Abs experiment with the aim to test the strain hypothesis, which credits the amazing catalytic effect of the coenzyme B<sub>12</sub>-dependent enzyme superfamily members to the external chemomechanical stress on the Co-C bond placed by the enzyme binding network. With the help of the kinetic arrested ternary complex, the possibility of this strain hypothesis has been excluded for the case of EAL.

**Chapter Six**

**Investigation of Photo-**  
**induced Co<sup>II</sup>-substrate**  
**Radical Pair Formation**

Photo-induced homolytic cleavage of the Co-C bond under anaerobic conditions has been employed as an alternative approach to study the AdoCbl thermal homolysis reaction since the late 1960's, because both reactions lead to the same primary products, which are the Co<sup>II</sup> derivative and the 5'-deoxyadenosyl radical.<sup>152,163-165</sup> In the early stages of photolysis studies, cryophotolysis in solution was often employed to study the products of the light-induced bond cleavage,<sup>73,166,167</sup> owing to the lack of transient techniques. For example, Loew and coworkers<sup>167</sup> applied EPR to study the photolysis of coenzyme B<sub>12</sub> in aqueous propane-1,2-diol and did not observe any photo-induced product at 77 K. Higher temperature photolysis led to a Co<sup>II</sup> signal plus an uncharacterized free radical signal. Upon further annealing to 300 K, the uncharacterized radical signal vanished but the Co<sup>II</sup> signal greatly increased.

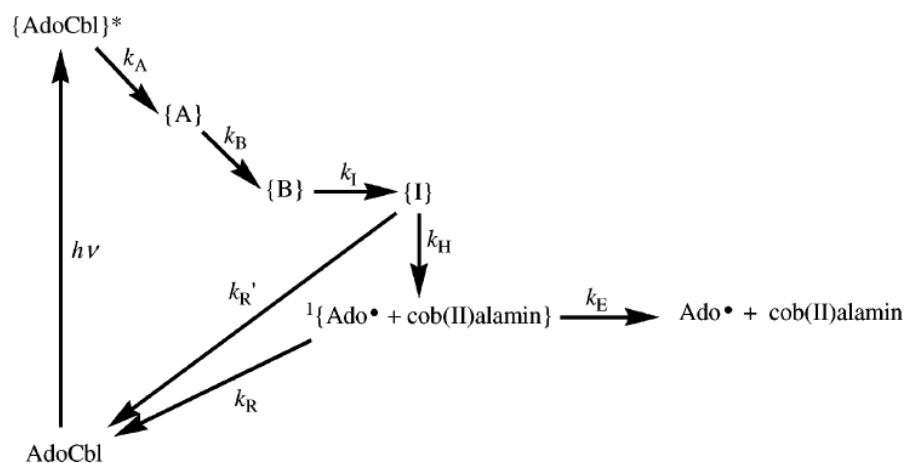
Nanosecond transient absorption spectroscopy was first applied in the investigation of the AdoCbl photolysis at ambient temperature by Endicott and coworkers.<sup>168</sup> The kinetic information on the formation of Co<sup>II</sup> on a sub 10 ns time scale after excitation of adenosylcobalamin in aqueous solution was further investigated experiments by a 532 or 355 nm laser pulse.<sup>169,170</sup> The results show that the photolysis process of AdoCbl at ambient temperature in aqueous solution is wavelength independent, whereas the photolysis of MeCbl is wavelength dependent, in terms of the intermediate species.<sup>170</sup> Continuous wave measurements with excitation at 442 nm was also used to confirm these findings.<sup>169</sup>

The time resolution in photolysis studies was further enhanced by Sension's group to the femtosecond range by using ultrafast spectroscopic techniques.<sup>13,171-174</sup> They applied this technique to study the solvent effect on the photolysis of AdoCbl in ethylene

glycol, water, and mixtures of these solvents.<sup>173,174</sup> In aqueous buffer, the photolysis produces different excited states with spectra evolving from the  $\text{Co}^{\text{III}}$  state to  $\text{Co}^{\text{II}}$  state, which decays sequentially on the 100 fs, 1-3 ps, and 14-37 ps times scales to form the intermediate state I, as shown in Scheme 1.<sup>173</sup> They also tested the kinetics of homolysis and recombination for AdoCbl bound in the active site of glutamate mutase,<sup>13</sup> which was the first such measurement on an AdoCbl-dependent enzyme. They found that the photo-induced homolytic cleavage and recombination rate constants were not significantly different from those measured in free solution, and concluded that the protein does not significantly perturb the stability of the Co-C bond upon binding the coenzyme, which supports our conclusion from UV-visible Abs experiments.

The previous work inspired us to apply the photolysis method to examine the kinetic information obtained in Chapter Three and Chapter Four, which focused on the thermally induced bond breaking event in AdoCbl in the presence of EAL enzyme. In these chapters, the time-resolved, full spectrum EPR study was applied to reveal a dominant entropic contribution to the Co-C bond cleavage process, which is intuitively thought to be caused by enthalpic contributions from either ground state destabilization and/or transition state stabilization.<sup>4,5</sup> In this chapter, we continue to investigate the EAL catalytic effect by adopting photo-induced Co-C bond cleavage as an alternative approach. The results will not only check the consistency of the entropy-driven mechanism, but also demonstrate the feasibility of the photo-induced enzyme catalysis, which is a mind-refreshing field. Pioneered efforts include the observation of carbon monoxide (or dioxygen) to migrate and rebind to the heme iron in myoglobin (Mb) after photolysis of the carboxy or oxy-heme state in frozen solutions at temperatures from 10

to 270 K.<sup>74,75</sup> Also usage of  $\gamma$ -ray in the irradiation of a frozen solution sample at 77 K to elicit one-electron reduction of a previously redox-poised metal center in the protein<sup>81-83</sup> have been reported. However none of these work leads to “jump-start” of the enzyme’s catalysis cycle by accumulating a significant population of intermediate states, as observed in the thermally induced enzyme activity. With the availability of the kinetically arrested EAL·B<sub>12</sub>·substrate ternary complex,<sup>26</sup> for the first time, we have the ability to probe the photo-induced enzyme activity.



Scheme 6.1: Mechanism for photolysis of AdoCbl in aqueous solution.<sup>173</sup>

## 6.1 Instrument Setup

The photolysis temperature is controlled by a home-made cooling system with  $T_{min} = 120$  K and temperature accuracy =  $\pm 1.5$  K in the range from 200 K to 300 K. The construction of this system has been explained in Chapter Two. Photolysis samples are loaded into 4 mm EPR tubes with a total volume of approximately 200  $\mu$ l. For anaerobic

experiments, the samples are carefully deoxygenated by several freeze-pump-thaw cycles and backfilled with argon gas. All light-sensitive samples, which contain AdoCbl, are prepared under a dim red-safe light.

Multiple light sources have been used to cover a wide excitation wavelength from 532 nm to 254 nm, as follows: (1) a pulsed Nd:YAG laser with 10 ns width (SpectraPhysics GCR-10) provides 532 nm and 355 nm photon via the second and third harmonic output individually. The pulse energy is adjustable through a glan prism polarizer/half-wave plate; (2) a continuous wave resonance lamp (Oriel 66021), which contains mercury vapor at high pressures, is coupled to a Leybold 400 nm short-pass filter and an  $\text{CuSO}_4$  IR-cut filter (General Glassblowing Company) to provide UV light. From such optical set up, the 254, 313 and 365 nm emission peaks are selected.<sup>175</sup> (3) a continuous wave low-noise 300 W xenon arc lamp (Hamamatsu, L2480) coupled with a monochromator (Applied Photophysics, F-34) offers a continuously adjustable excitation beam with a bandwidth of approximately 25 nm from 532 nm to 400 nm.

The photon beam emitted from various light sources is focused through a cylindrical lens (Newport Corp.) onto the sample, which is loaded in a 4 mm OD quartz EPR tube. After focusing, the light beam covers an area with width  $\approx 0.5$  cm and length  $\approx 2.0$  cm. The pulsed photon beam energy can be measured with an EPM1000 laser power meter (Molelectron Detector Inc.).

A typical experiment consists of 4-6 intervals of photolysis, followed by a rapid cryotrapping in liquid nitrogen and sequential EPR spectrum collection with a Bruker ER560 spectrometer. The EPR spectrum recorded after each photolysis interval is used to trace the time course of any paramagnetic states induced by the irradiation. EPR spectrum

of the initial state is also recorded as background. The time interval of irradiation depends on the light source intensity.

## 6.2 Photolysis of Cofactor B<sub>12</sub>

The anaerobic solution of AdoCbl in 41% DMSO/water cryosolvent is irradiated by different light sources at ambient temperature. Figure 6.1 shows representative EPR spectra of AdoCbl photolyzed by using the pulsed 532 nm laser, pulsed 355 nm laser at 298 K.

At ambient temperature, samples that received photon irradiation for 2-10 min by the different light sources all produce a well resolved "base-on" Co<sup>II</sup> signal. This Co<sup>II</sup> signal has a dominant line shape centered at  $g=2.26$ , which correspond to the orientations of the magnetic field perpendicular to the  $d_z^2$  orbital of the Co<sup>II</sup>. Hyperfine coupling of the unpaired  $d$  electron with the <sup>59</sup>Co nuclear ( $I=7/2$ ) splits transitions in the perpendicular and parallel regions into eight components. The components of the <sup>59</sup>Co hyperfine splitting in the perpendicular direction are unresolved due to its small amplitude, whereas those for the magnetic field parallel to the  $d_z^2$  orbital give rise to resolved features centered at  $g = 2.0$ , which yields a coupling constant  $A_{||} = 110$  G from previous reports.<sup>73,167</sup> A superhyperfine interaction with an axial nitrogen ligand ( $I=1$ ) further splits the parallel components into 1:1:1 triplets ( $A_N = 19$  G). This result is consistent with the previous AdoCbl photolysis result inside aqueous solution.<sup>169,170</sup>

## 6.3 Photolysis of Holoenzyme and Ternary Complex

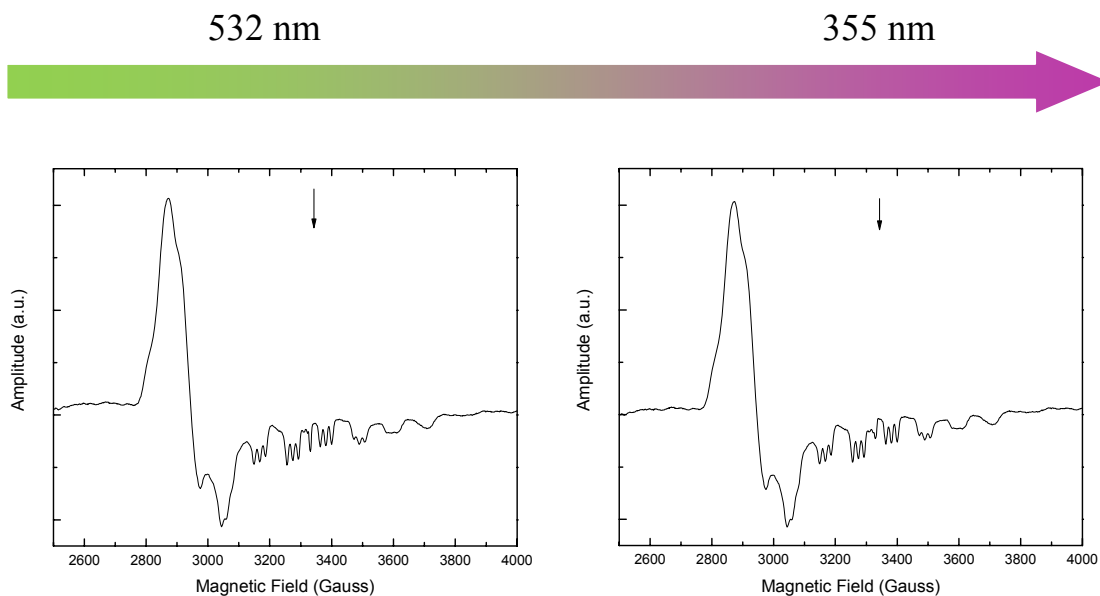


Figure 6.1: EPR spectra following photolysis of AdoCbl in 41% DMSO/water cryosolvent. [AdoCbl]=60  $\mu$ M. 532 nm, 355 nm and UV refer to the sample irradiation with 532 nm pulsed-laser, 355 nm pulsed-laser and mercury lamp respectively. The arrow indicates the  $g=2.000$  position. *EPR conditions*: microwave frequency, 9.379 GHz; microwave power, 10 dB (20 mW); magnetic field modulation, 10 Gauss peak-peak; modulation frequency, 100 kHz; field sweep rate, 1.5 Gauss  $s^{-1}$ ; time constant, 164 ms; average of 2 sweeps, minus average of 2 baseline spectra.

In contrast to the photolysis experiment of free AdoCbl, the photolysis of EAL holoenzyme and ternary complex does not require the anaerobic condition since our control experiments demonstrate that the presence of oxygen does not alter the photolysis products. This conclusion implies a tight binding of the AdoCbl by EAL, which prevents the access of  $O_2$  inside the EAL active site, in the absence of substrate. It has also been experimentally confirmed that the irradiation of the EAL apo-enzyme will not lead to the generation of any protein-related radical. Figure 6.2 shows the representative results, which are the EPR spectra of holoenzyme and ternary complex samples that are photolyzed with pulsed 532 nm and pulsed 355 nm laser at 230 K.

In the low temperature range, a new EPR signal is observed after photolysis on the holoenzyme. As shown in the top part of Figure 6.2, holoenzyme samples irradiated with 532 nm pulsed laser beam at 230 K both produce a weak “base-on”  $\text{Co}^{\text{II}}$  lineshape plus a six times stronger  $g = 2.0$  signal with a line width of  $\sim 100$  G. This  $g = 2.0$  signal increases with irradiation time over tens of minutes before reaching maximum amplitude and does not decay at 230 K for at least hours. The photolysis products from irradiation with the 355 nm pulsed-laser are similar to the case of irradiation with the 532 nm pulsed laser, except that the  $\text{Co}^{\text{II}}$  state doubles its population at lower wavelength. These results are in large contrast to the single “base-on”  $\text{Co}^{\text{II}}$  signal observed in the photolysis of free AdoCbl in Figure 6.1. The further pursuit of the photolysis mechanism relies on the transient UV-visible spectroscopy and will not be discussed in this dissertation.

The photolysis of the ternary complex yield identical results at various irradiation wavelengths comparing to the case of holoenzyme. The EPR spectra after photolysis show the “base-on”  $\text{Co}^{\text{II}}$  signal and the uncharacterized  $g = 2.0$  signal in the bottom of Figure 6.2. Besides pulsed-laser, continuous wave light sources including the mercury lamp and the Xeon lamp have been employed to perform the photolysis within a wide wavelength range from 533 nm down to 254 nm. None of these efforts “jump-start” the EAL catalytic cycle, in which the  $\text{Co}^{\text{II}}$ -substrate radical pair will be accumulated and detected by EPR. This observation supports our previous finding that the catalytic effect of EAL is not contributed by enthalpic factor but rather than other entropic considerations. The rationalization is that if EAL exerted chemomechanical strain on the Co-C bond to facilitate the catalysis, the photo-induced homolytic cleavage of the Co-C bond will lead

the enzyme to the hydrogen transfer (HT1) step, during which the  $\text{Co}^{\text{II}}$ -substrate radical pair is formed and accumulated.

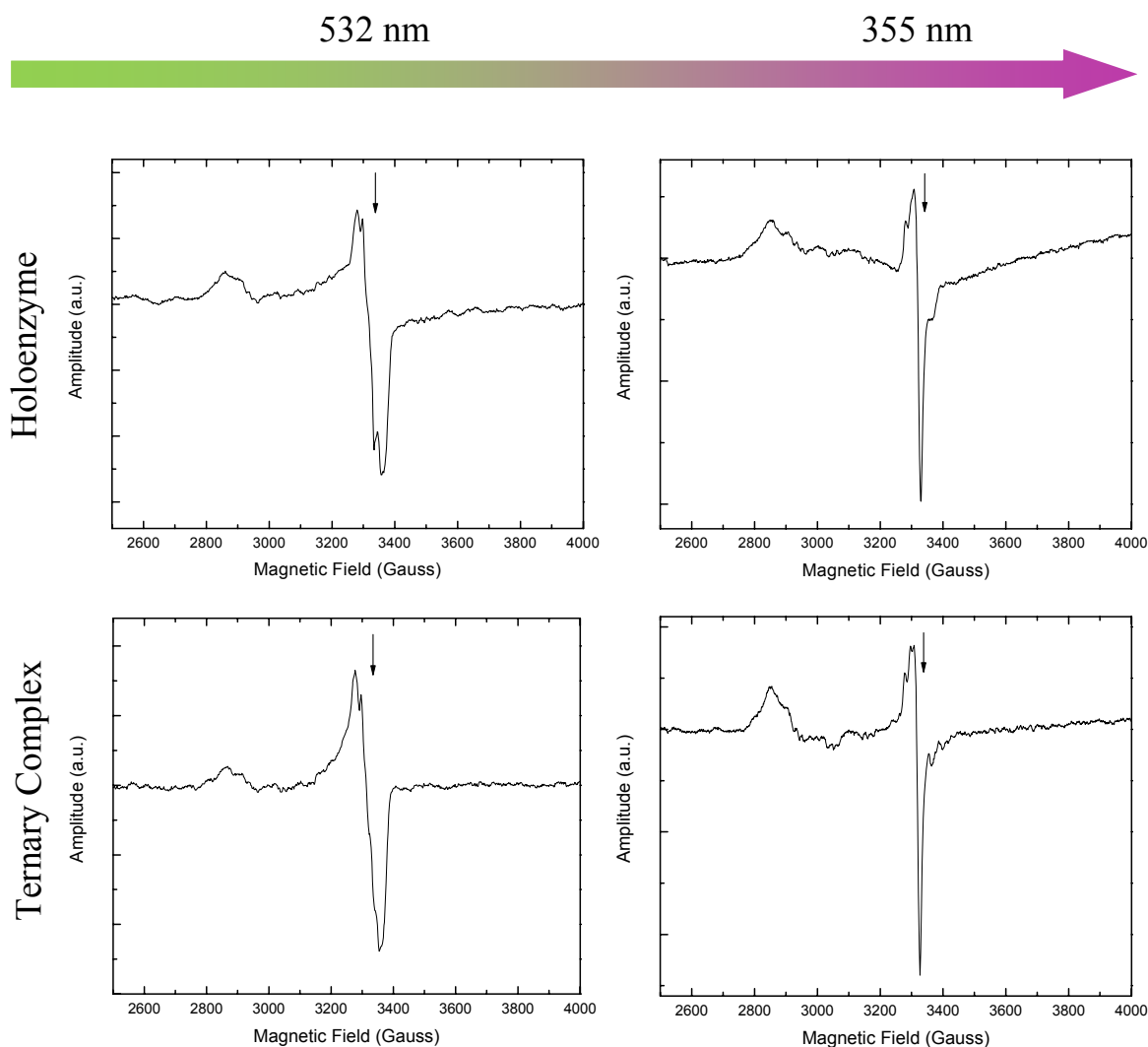


Figure 6.2: EPR spectra following photolysis of holoenzyme and ternary complex at 230 K. 532 nm, 355 nm and UV refer to the irradiation with 532 nm pulsed-laser and 355 nm pulsed-laser. The arrow indicates the  $g=2.000$  position. The concentrations of EAL active sites, coenzyme  $\text{B}_{12}$  and substrate are  $120 \mu\text{M}$ ,  $30 \mu\text{M}$  and  $12 \text{ mM}$ , respectively. *EPR conditions*: microwave frequency,  $9.374 \text{ GHz}$ ; microwave power,  $10 \text{ dB}$  ( $20 \text{ mW}$ ); magnetic field modulation,  $10 \text{ Gauss}$  peak-peak; modulation frequency,  $100 \text{ kHz}$ ; field sweep rate,  $1.5 \text{ Gauss s}^{-1}$ ; time constant,  $164 \text{ ms}$ ; average of 2 sweeps, minus average of 2 baseline spectra.

## 6.4 Application of Spin Trap in Photolysis

Spin trap has been applied in the kinetic study of the thermolysis of AdoCbl and its derivatives. For example, Brown and Zou studied the thermolysis of AdoCbl in the aqueous solution by using radical trap H-TEMPO.<sup>176</sup> In their experiment, the only Ado-derived products observed are adenine and the trapped Ado• radical, which is Ado-H-TEMPO. This observation indicates that the radical trap is kinetically competent to prevent both reentry of the solvent-separated radicals into the solvent cage and the cyclization of the Ado• radical. Similarly, Magnusson and Frey applied the radical trap TEMPO to investigate the thermolysis of 3',4'-anAdoCbl in ethylene glycol. The only observed nucleoside-containing products are 5'-TEMPO-3',4'-anhydroadenosine and 3'-TEMPO-3',4'-anhydroadenosine.<sup>177</sup>

However, our experiment utilizes EPR to analyze the photolysis produce. This makes TEMPO an unsuitable spin trapping chemical because TEMPO is already in paramagnetic state before reacting with any short-lived radical, which will not provide a clean initial EPR background. The most commonly used spin traps in EPR study is 5,5-dimethylpyrroline-*N*-oxide (DMPO, shown in Figure 4). This spin trap utilizes the reaction of unstable free radicals with nitrones spin traps resulting in the production of long-lived nitroxide radicals, which can be detected by EPR spectroscopy. DMPO has been applied in various reactions to trap •O, •OH, and alkyl radicals.<sup>178-180</sup>

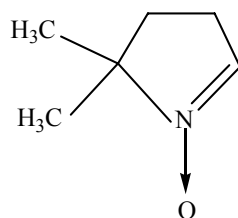


Figure 6.3: Chemical structure of DMPO

For the irradiation of the holoenzyme and ternary complex at 230 K, 1000 fold excess DMPO over the AdoCbl was added to the sample. The introduction of spin trap does not alter the photolysis product. This result implies that the radical species, which are generated from photolysis, are confined inside the EAL enzyme and do not migrate to the surface. This observation is consistent with independent experimental result that the radical intermediates at the active site is well shielded by the backbone of methylmalonyl-CoA mutase.<sup>181</sup>

## 6.5 Concluding Remarks

For the first time, photolysis on the ternary complex of coenzyme B<sub>12</sub>-dependent enzyme with functional substrate is performed. The photon irradiation at various wavelengths does not lead to the formation of Co<sup>II</sup>-substrate radical pair, which is the intermediate state that has large population during the EAL catalysis. This result implies that the intrinsic event of Co-C bond cleavage is not enthalpy driven and possibly synchronized to other entropy driven process, which is concluded from the studies on thermally induced Co<sup>II</sup>-substrate radical pair formation.

# **Appendix**

## **Manuals and Protocols**

## Instruction for Oxford Cryostat System with Bruker E560 Console

### **Preparing the Helium Tank**

- (1) The Helium Tank (60 L or 100 L) should be steadily stored near the location (within 3 feet) where it will be during experiment for at least 12 hours before starting the experiment.
- (2) The safety vent valve should be open.

### **Preparing the Bruker ESR900 Cryostat**

- (1) Place the Helium purge gas inlet adaptor on top of the chimneystack and plug in the outlet adaptor on the entry arm. Turn on the GF3 mechanic pump, the pressure shown on VC41 should drop below -800 millibar in seconds. Then turn off the pump, the pressure should remain below -800 millibar for minutes. If the pressure rises, check for leaks.
- (2) Use the Helium gas to flush the system for 5 minutes.
- (3) Turn on the GF3 mechanic pump to vacuum the cryostat for 20 minutes.
- (4) Repeat step (2) and (3) for another 2 cycles.
- (5) Open the Helium purge gas.

### **Preparing the transfer line**

- (1) If the transfer line has not been used for weeks. Need to complete the following steps first.
  - (a) Put the transfer line on diffusion pump for overnight in the machine shop. The final pressure is around  $3.2 \times 10^{-6}$  torr.
  - (b) Use the nitrogen gas with the plastic stem adaptor to flush the transfer line for minutes;
  - (c) Double check the transfer line nozzle tip. Make sure it is straight.
- (2) Connect the transfer line needle valve cable to the ITC503.
- (3) Turn on the ITC503. Wait until the gas control light stops flashing.
- (4) Manually dial the gas flow rate to 99.99% and wait until the transfer line motor stops.
- (5) Gently disconnect the transfer line.

**Inserting the transfer line stem in the liquid Helium tank**

Warning! To avoid possible damage to the transfer line (both the front nozzle tip and the needle valve motor are very fragile), two persons are required to finish this part. Also make sure the transfer line stem is not bended during the whole process.

- (1) Open the helium gas vent valve to lower the tank pressure to one atmosphere. Open the top insertion valve and loose the top brass nut.
- (2) Use the ladder to SLOWLY insert the stem into the liquid Helium tank. Watch out for the obstacles on the roof to protect the motor. The gas vent valve should remain wide open during the insertion process.
- (3) Quickly tighten the top brass nut and close the gas vent valve. The safety vent valve should remain OPEN.
- (4) Use a small flask of ethanol to perform the bubble test by immersing the front nozzle tip into the liquid. If no bubbles, check if the flow rate is still 99.99% by connecting the transfer line cable to ITC503. If the gas flow rate is correct, you have to remove the transfer line, warm up to room temperature.

**Inserting the transfer line to the ESR900 cryostat**

- (1) Slowly move the Helium tank with the transfer line to make the cryostat entry arm and the transfer line nozzle close enough for a convenient insertion.
- (2) Make sure the helium gas purge in ESR900 is still on. Take off the purge gas outlet adaptor and quickly insert the transfer line nozzle into the cryostat until it stops. But do not tighten the nut on the transfer line.
- (3) Connect the pump line and the needle valve line to the transfer line.
- (4) Quickly take off the inlet helium gas purge adaptor and substitute it with the black seal hat. Close the He gas cylinder gauge.
- (5) Turn on the GF3 pump. The initial gas flow rate should be almost 0 and the cryostat pressure should be lowered again to below -800 millibar.

- (6) After 5 to 10 minutes, the gas flow rate will rise quickly to the top limit. At this time point, quickly tighten the nut all the way to the bottom. The gas flow rate will immediately drop and the temperature will go up slightly first and then start to fall. If the temperature could not fall below 273 K within 10 minutes after you finish the above steps, you have to restart from the very beginning.
- (7) Slowly lift the transfer line stem 1 inch from the tank bottom and retighten the brass nut. Use a Teflon tape to monitor the stem position.

### **Connecting to the computer console**

- (1) Start the E560 system as normal. Open the Xepr software on the computer and link to the spectrometer.
- (2) Select Acquisition -> Spectrometer configuration menu. Click the Misc. Tab. Under the TEMPERATURE CONTROLLER, select Type from a pulling down menu to be ITC 503, select Heater Sensor from another pulling down menu to be SENSOR 1. On the bottom of the window, click Apply and then click Close button.
- (3) Under the main graphic panel, click the Temperature Controller icon. In the following window under the Temperature tab, first select Use VTU, then adjust the following parameters to be: Temperature -> 6 K (or your desired temperature), Tolerance -> 0.2 K, Setting Time-> 5 s. Switch to the ITC5 Tab, in the multiple choices of ITC5 OPERATION MODES, select the HEATER Control to be Auto and the Gas Flow Control to be Manual. Then select Unlock PID SETTING. Set the Gas Flow to be 99% initially. Input 100 in the HEATER Power Limit (%). Under the PID Parameters, set Proportion to be 50 K, the Integral Time to be 0.2 min and the Derivative Time to be 0.2 min.
- (4) Wait until the temperature falls below 80 K, then set the Gas Flow to be around 20% if your desired temperature is 6 K. (Power off the pump and insert your sample at this time if needed. Repower on the GF3 pump)
- (5) Wait till your desired temperature is reached. Make fine adjustment of the Gas Flow rate (by

step of 0.5 at most) until a stabilized temperature (less than 0.2 K) is achieved.

(6) Start scanning spectrum. Do not touch the liquid helium tank during the experiment.

### **Changing Samples:**

(1) Set the microwave bridge in Tune mode.

(2) Thoroughly clean the EPR tube for the next scan by multiple (at least 3 times) wiping of the tube wall.

(3) Power off the GF3 pump and wait until the pressure meter on VC41 to reach 0 millibar.

(4) Quickly take out the sample with the top seal adaptor and put on the black hat seal.

(5) Take of the seal adaptor from the old sample and put it on the sample for next scan.

(6) Quickly take off the black hat seal and switch in the new sample.

(7) Slowly lowering down the sample to find the bottom dip inside the cryostat. Once the bottom position is found, tighten the EPR tube seal adaptor.

(8) Power on the GF3 pump and wait until the temperature restablizes. Make fine adjustment (less then 0.5) of the Gas Flow rate if necessary.

### **Finishing experiment**

Warning: To avoid possible damage to the transfer line (both the front nozzle tip and the needle valve motor are very fragile), two persons are required to finish this part. Also make sure the transfer line stem is straight during the whole process.

(1) Turn off the GF3 pump.

(2) Quickly take out your sample and put on the black hat seal.

(3) Power down the spectrometer and ITC503.

(4) Use an electric heater to heat up the joining section between the white plastic pump line and the transfer line. Then disconnect the pump line.

(5) Gently disconnect the needle valve line.

(6) Loose the transfer line nut completely and pull out the transfer line from the cryostat entry arm.

- (7) Connect the inlet and outlet adaptor to the ESR900 cryostat to perform a 30 minutes He gas purge.
- (8) Use the ladder to pull out the transfer line from the liquid helium tank.

### **Data Analysis**

Use the Matlab program **LH2EPR.m** to analyze the stability and SNR of the data.

## Ternary Complex Preparation Procedure for EPR Studies

### Preparation:

Take proper amount of dilute EDA from large centrifuge tube and spin 12 min at 5500 rpm, remove the upper liquid and adjust to desired final volume with 10 mM strength K cacodylate buffer, which is balanced to pH =7.2 at 25 °C. I usually prepare 5 of these 100  $\mu$ L EDA at one time for further useage;

- (1) Prepare one 100  $\mu$ L EDA at 480  $\mu$ M (40 mg/ml) concentration in a clean culture tube A;
- (2) Take 140  $\mu$ L 99.5% DMSO and pipette to a separate clean culture tube B, dilute with 60  $\mu$ L 10 mM strength K cacodylate buffer, pH =7.2 at 25 °C;
- (3) Prepare proper amount of substrate in tube C (depends on the ratio of active sites to substrate), dilute with same volume of 99.5% DMSO organic solvent to make a 50% (v:v) solution. Make sure the total volume of the substrate solution is less than 20  $\mu$ L;
- (4) Cut a clean 5 mm o.d. NMR test tube to 10.2 cm length (keep the sealed end intact);
- (5) Take a clean 2 mm o.d. EPR test tube and cut to 16.0 cm length (both ends need to be open). Then make two black lines on the outer shell. One at 4.0 cm (count from the cut end, this will be the liquid level), one at 16.0 cm (also count from the cut end, this line indicates the position of the plastic nut). Then insert one open end to a clean disposable syringe;
- (6) Turn on the cryostat in N107 and dial it to 1 °C;
- (7) Prepare -60 °C isopentane under the hood of E126 (keep a thermostat in the Dewar);

### **All the procedures below should be performed under red safe light in N107**

- (8) Pipette proper amount of B<sub>12</sub> into the tube A. I usually keep the ratio of B<sub>12</sub> to active site as 2:1, then vertex the tube A at room temperature (25 °C) for 1 min;
- (9) Take a clean long glass pipette to slowly transfer the solution in the tube A to one 5 mm o.d. NMR tube;

- (10) Insert the 5 mm o.d. tube into the cryostat. Wait 2 min to reach temperature equilibrium;
- (11) Use a clean long glass pipette to transfer 15  $\mu\text{L}$  water/DMSO solvent in the tube B into the 5 mm o.d. tube, wait 3 min to reach temperature equilibrium;
- (12) Set the cryostat to  $-8\text{ }^{\circ}\text{C}$ , wait 2 min. If frozen happens (solution becomes opaque), stir with a clean 1 mm steel bar sealed with Teflon;
- (13) Use the long glass pipette to transfer 30  $\mu\text{L}$  water/DMSO solvent in the tube B into the 5 mm o.d. tube;
- (14) Set the cryostat to  $-16\text{ }^{\circ}\text{C}$ , wait 2 min. If frozen happens, stir with the 1 mm steel bar;
- (15) Use the long glass pipette to transfer 30  $\mu\text{L}$  water/DMSO solvent in the tube B into the 5 mm o.d. tube;
- (16) Set the cryostat to  $-24\text{ }^{\circ}\text{C}$ , wait 2 min. If frozen happens, stir with the 1 mm steel bar;
- (17) Use the long glass pipette to transfer 30  $\mu\text{L}$  water/DMSO solvent in the tube B into the 5 mm o.d. tube;
- (18) Set the cryostat to  $-34\text{ }^{\circ}\text{C}$ , wait 2 min. If frozen happens, stir with the 1 mm steel bar;
- (19) Use the long glass pipette to transfer 50  $\mu\text{L}$  water/DMSO solvent in the tube B into the 5 mm o.d. tube;
- (20) Set the cryostat to  $-43\text{ }^{\circ}\text{C}$ , wait 2 min. If frozen occurs, stir with the 1 mm bar;
- (21) Use a separate clean long glass pipette to slowly transfer the substrate in the tube C into the 5 mm o.d. tube. Stir with the 1 mm bar for 30 seconds;
- (22) Check the temperature of the isopentane. If less than  $-50\text{ }^{\circ}\text{C}$ , need to add in some  $\text{LN}_2$  to make it  $-50\text{ }^{\circ}\text{C}$  to  $-60\text{ }^{\circ}\text{C}$ ;
- (23) Take a clean 1.5 mL white centrifuge test tube. Drop in a section of 5 mm length blue wax and melt the wax into blue liquid with the electric heater in N107. Start a timer, 1 min and 30 seconds count down;
- (24) Insert the 2 mm o.d. tube into the 5 mm o.d. tube and use the syringe on top to carefully raise the solution level to the 4.0 cm black line;

- (25) Quickly dip the 2 mm o.d. tube into the cold isopentane and put the 5 mm o.d. tube in LN<sub>2</sub> for further use;
- (26) When the timer alarm is on, quickly pull out the 2 mm o.d. tube from the isopentane and push it into the blue wax to make a seal. This step must be completed within 15 seconds;
- (27) Quickly dip the 2 mm o.d. tube back to isopentane. Wait for 1 min, then repeat step 26;
- (28) Quickly dip the 2 mm o.d. tube back to isopentane. Remove the syringe and seal the other open end with the blue wax.
- (29) Bring the 2 mm o.d. tube in isopentane to E126 to perform further EPR experiment.

Note: One batch of ternary complex prepared in 5 mm o.d. tube could provide at least 5 2 mm o.d. tube samples.

Synthesis of [1,1-<sup>2</sup>H<sub>2</sub>]-aminopropanol**Preparation:**

- (P1) Clean all the glass ware thoroughly and keep it dry;
- (P2) Use 30-50 ml ether to wash the refluxing apparatus, continuous extraction apparatus and rotary evaporator separately;
- (P3) Keep all the apparatus dry under the fume hood.

**Day One Afternoon:**

- (1) Suspend 1.4 g L-alanine methyl ester hydrochloride in 20 ml ether at 0 °C;
- (2) Transform to free base by passing ammonia at 0 °C for 60 minutes (NH<sub>3</sub> flow rate 5 cc/min);
- (3) Adjust the total volume of the liquid phase with ether to 20 ml
- (4) Dry the solution over Na<sub>2</sub>SO<sub>4</sub> (5 gram powder) for overnight in 4 °C refrigerator;

**Day Two: try to finish before 12:00 p.m.**

- (5) Pull negative vacuum over the flask with side arm (35 cc/min flow rate) at 0 °C and filter the liquid quickly;
- (6) Add 20 ml ether to the flask with Na<sub>2</sub>SO<sub>4</sub> to wash the deposit and filter the liquid (total volume now is around 35 ml);
- (7) Transfer the combined liquid to the round bottom flask and drop in 1 g of LiAlD<sub>4</sub> in 30 ml ether (require magnetic stir bar, reflux condenser, dropping funnel setup);
- (8) Boil the water bath to 38 °C with heater power and then turn off the heater;
- (9) Turn on the heater with full power once the temperature drops down to 38 °C and turn off once the water bath reached 41 °C;
- (10) Keep adjusting the water bath temperature for 60 minutes of reaction;
- (11) Cool the mixture to 0 °C in the ice bucket;
- (12) Add 6 ml D<sub>2</sub>O to quench the excessive LiAlD<sub>4</sub> (now total volume is around 70 ml);

- (13) Add in 30 ml water to dilution the solution (total volume is around 100 ml);
- (14) Transfer the mixture to the continuous extraction apparatus and extract for 48 hours with 170 ml ether containing 10 ml of 10% w/w HCl solution in the 250 ml round bottom flask. The stock HCl acid concentration is around 37% w/w;

**Day Three**

- (15) Wait for the continuous extraction. Always fill the water to the top level. The water level dropping rate on the average at 55 °C is 4 mm/hour.

**Day Four:**

- (1) After 48 hours of continuous extraction, evaporate the extracted solution to dryness in the rotary evaporator for 40 minutes at 55 °C at one atmosphere;
- (15) Adjust temperature to 85 °C and evaporate for 1 hour under vacuum;
- (16) Use 3:1 ethanol-ether solution to recrystallize the residue three times, each cycle last for 40 minutes;
- (15) Expect 567 mg (if 50% yield) [1,1-<sup>2</sup>H<sub>2</sub>]-aminopropanol in oil liquid.

## Ternary Complex Sample Preparation for UV-Visible Abs

- (1) Turn on the Shimadzu 1601 spectrometer, warm up the UV lamp;
- (2) prepare 140  $\mu\text{L}$  apo-EAL at concentration 43.6 mg/ml in a culture tube, the aqueous buffer should be the 10 mM cacodylate buffer;
- (3) Add 7  $\mu\text{L}$  5.2 mM AdoCbl at ambient temperature to obtain EAL holoenzyme;
- (4) Prepare 300  $\mu\text{L}$  70% v:v DMSO solvent by mixing 210  $\mu\text{L}$  99.8% DMSO with 90  $\mu\text{L}$  10 mM cacodylate buffer in a separate culture tube;
- (5) Load the holoenzyme sample into one 4 mm O.D. EPR tube and use the cryostat in N107 to pre-cool the sample to 1  $^{\circ}\text{C}$ ;
- (6) Introduce the following amount of 70% DMSO/water cryosolvent at the corresponding temperature. This step follows the ternary sample preparation protocol for EPR study.

<b>Cryosolvent Introducing Temperature (<math>^{\circ}\text{C}</math>)</b>	<b>Volume of Cryosolvent to be Introduced (<math>\mu\text{L}</math>)</b>
<b>1</b>	21
<b>-8</b>	42
<b>-16</b>	42
<b>-24</b>	42
<b>-34</b>	70

- (7) Mix 440.64  $\mu\text{L}$  99.8% DMSO with 375.36  $\mu\text{L}$  10 mM cacodylate buffer in a culture tube to obtain 54% v:v DMSO/water cryosolvent;
- (8) Load the 54% DMSO/water cryosolvent to the Hellma QS 282 1.000 ml quartz cuvette;
- (9) Take 50  $\mu\text{L}$  cryosolvent out of the cuvette and pipette back into the culture tube for later sample wash;

- (10) Load the cuvette into the sample holder and turn on the cooling system;
- (11) Dial the setting temperature to  $-33\text{ }^{\circ}\text{C}$  and wait until the system reach equilibrium;
- (12) Bring the prepared holoenzyme in N107 to the Shimadzu with the protection of pre-cooled isopentane at  $-33\text{ }^{\circ}\text{C}$ ;
- (13) Use a pre-cooled glass pipette to transfer the holoenzyme into the cuvette at  $-33\text{ }^{\circ}\text{C}$ ;
- (14) Wash the holoenzyme residue inside the EPR tube with the  $50\text{ }\mu\text{L}$  cryosolvent and transfer to the cuvette;
- (15) Dial the setting temperature to  $-42\text{ }^{\circ}\text{C}$  and wait until the system reach equilibrium;
- (16) Prepare  $6.6\text{ }\mu\text{L}$  substrate solution by mixing  $3.3\text{ }\mu\text{L}$   $2.2\text{ M}$  S-2-aminopropanol with  $3.3\text{ }\mu\text{L}$   $99.8\%$  DMSO in a clean culture tube;
- (17) Cool down the substrate solution be dipping the culture tube into the cold isopentane solution;
- (18) Use a pre-cooled glass pipette to transfer the substrate into the cuvette at  $-42\text{ }^{\circ}\text{C}$ ;
- (19) Start Data Collection.

- When mixing occurs at low temperature, always use the Teflon stir bar to perform thorough mixing for at least 2 minutes;
- A  $0.1\text{ nm}$  scan step with 3 accumulations are suggested in the data collection. Use program **uvspec.m** to read the data file.

## Cary 100 Basic Operation Manual

- (1) Make sure the sample compartment is empty and the lid is closed;
- (2) Turn on the spectrometer by depressing the rocker switch marked | ;
- (3) Wait 15 minutes for the instrument to warm up;
- (4) Start the WinUV Scan Program;
- (5) click Setup from the Menu line;
- (6) In the Cary Tab
  - a. set X mode to nanometers;
  - b. input the scan wavelength range;
  - c. set Y mode to Abs;
  - d. input Ymin and Ymax;
  - e. set Ave Time (try 0.1)
  - f. set Data Interval (try 0.1 nm);
  - g. decide if select Cycle Mode
- (7) In the Options tab
  - a. Set the SBW to 0.2 nm (spectrometer lower limit);
  - b. Set Beam Mode to Double (usual mode);
  - c. Decide if select UV/Vis to turn on both lamps (recommended);
  - d. Decide if select Auto Lamps Off to turn off the lamps after each run (not recommended);
  - e. Do not select 'Signal-to-Noise Mode';
  - f. Select Individual Data or Overlay Data (recommended);
- (8) No change in the Independent tab;
- (9) In the Baseline Tab, select Baseline Correction;

- (10) In the Accessories 1 tab, 2 tab, 3 tab, make sure select nothing;
- (11) In the Reports Tab
  - a. Enter name in the Name entry field;
  - b. Enter a comment in the Comment field;
  - c. Select your report style, Auto Print is not recommended;
  - d. Select Autoconvert option (ASCII with Log);
- (12) In the Auto Store tab, select Storage On;
- (13) click OK;
- (14) Save the Method by clicking Save in the Menu line and select save method;
- (15) Click Zero;
- (16) Insert two blank samples (nanowater in cuvettes), click Baseline;
- (17) Insert 1 ml sonicated EAL apoenzyme (dilute to 5 mg/ml, 60  $\mu$ M active site), relax for 10 minutes;
- (18) Click Start and input file name and comments, do it four times;
- (19) Add in substrate (S-1-amino-2-propanol, 100 $\times$  enzyme active sites), stir well (2 minutes) and relax for 10 minutes;
- (20) Click Start and input file name and comment, do it four times;
- (21) Add in B12 (0.5 X enzyme), stir well (2 minutes) and relax for 10 minutes;
- (22) Click Start and input file name and comment, do it four times.
- (23) Insert sonicated EAL apoenzyme and collect spectrum;
- (24) Add in B<sub>12</sub>, stir well (2 minutes) and relax for 10 minutes;
- (25) Collect spectrum;
- (26) Transfer the data and turn off spectrometer.

## List of Coded Programs

**matview.m:** Read the spectrum from Xepr program directly with automatic reading the EPR condition from DSC file, which includes magnetic field range, number of data points etc. Please copy the DSC and DTA file together under the same folder.

**timecourse.m:** Generate the time course of  $\text{Co}^{\text{II}}$ -substrate radical formation with automatic reading the EPR condition, such as field range, number of points, time axle etc. Please copy the DSC and DTA file together under the same file folder.

**LH2EPR.m:** Analyze the stability and SNR of 6 K EPR spectrum. Please copy and DSC and DTA file together under the same file folder.

**uvkinetic.m:** Generate the optical  $\text{Co}^{\text{III}}$  to  $\text{Co}^{\text{II}}$  conversion time course from direct readout of the spc file produced by Shimazhu 1601.

**uvspec.m:** Read the spc file from Shimazhu 1601 directly with optional multispectrum average function.

**cary100.m:** Read and average the Cary 100 output, which is in the format of csv.

All these programs are available on the physics network server at:

[\\Luma\gr\\_warncke\mwang\Programs](\\Luma\gr_warncke\mwang\Programs)

## Bibliography:

- (1) Kratky, C.; Farber, G.; Gruber, K.; Wilson, K.; Dauter, Z.; Nolting, H. F.; Konrat, R.; Krautler, B. *Journal of the American Chemical Society* **1995**, *117*, 4654-4670.
- (2) Hay, B. P.; Finke, R. G. *Journal of the American Chemical Society* **1987**, *109*, 8012-8018.
- (3) Hay, B. P.; Finke, R. G. *Polyhedron* **1988**, *7*, 1469-1481.
- (4) Toraya, T. *Chem. Rev.* **2003**, *103*, 2095-2127.
- (5) Brown, K. L. *Chem. Rev.* **2005**, *105*, 2075-2149.
- (6) Banerjee, R. *Chemistry and Biochemistry of B12*; Wiley: New York, 1999.
- (7) *B12*; Dolphin, D., Ed.; Wiley: New York, 1982; Vol. 2.
- (8) Ng, F. T. T.; Rempel, G. L.; Halpern, J. *Journal of the American Chemical Society* **1982**, *104*, 621-623.
- (9) Marzilli, L. G.; Summers, M. F.; Brescianipahor, N.; Zangrando, E.; Charland, J. P.; Randaccio, L. *Journal of the American Chemical Society* **1985**, *107*, 6880-6888.
- (10) DeRidder, D. J. A.; Zangrando, E.; Burgi, H. B. In *9th International Symposium on Organic Crystal Chemistry (a Satellite Symposium of the 15th European Crystallographics Meeting in Dresden)*; Elsevier Science Bv: Poznan Rydzyna, Poland, 1994, p 63-83.
- (11) Grate, J. H.; Schrauzer, G. N. *Journal of the American Chemical Society* **1979**, *101*, 4601-4611.
- (12) Geno, M. K.; Halpern, J. *Journal of the American Chemical Society* **1987**, *109*, 1238-1240.
- (13) Sension, R. J.; Cole, A. G.; Harris, A. D.; Fox, C. C.; Woodbury, N. W.; Lin, S.; Marsh, E. N. G. *Journal of the American Chemical Society* **2004**, *126*, 1598-1599.
- (14) Chowdhury, S.; Banerjee, R. *Biochemistry* **2000**, *39*, 7998-8006.
- (15) Chih, H. W.; Roymoulik, I.; Huhta, M. S.; Madhavapeddi, P.; Marsh, E. N. G. In *Enzyme Kinetics and Mechanism, Pt F: Detection and Characterization of Enzyme Reaction Intermediates*; Academic Press Inc: San Diego, 2002; Vol. 354, p 380-399.
- (16) Licht, S.; Gerfen, G. J.; Stubbe, J. *Science* **1996**, *271*, 477-481.
- (17) Hollaway, M. R.; White, H. A.; Joblin, K. N.; Johnson, A. W.; Lappert, M. F.; Wallis, O. C. *Eur. J. Biochem.* **1978**, *82*, 143-154.
- (18) Bandarian, V.; Reed, G. H. *Biochemistry* **2000**, *39*, 12069-12075.
- (19) Padmakumar, R.; Padmakumar, R.; Banerjee, R. *Biochemistry* **1997**, *36*, 3713-3718.
- (20) Banerjee, R. *Biochemistry* **2001**, *40*, 6191-6198.
- (21) Mansoorabadi, S. O.; Magnusson, O. T.; Poyner, R. R.; Frey, P. A.; Reed, G. H. *Biochemistry* **2006**, *45*, 14362-14370.
- (22) Licht, S.; Lawrence, C. C.; Stubbe, J. *Biochemistry* **1999**, *38*, 1234-1242.
- (23) Boas, J. F.; Hicks, P. R.; Pilbrow, J. R.; Smith, T. D. *J. Chem. Soc. Faraday II* **1978**, *74*, 417-431.
- (24) Gerfen, G. J.; Licht, S.; Willems, J. P.; Hoffman, B. M.; Stubbe, J. *Journal of the American Chemical Society* **1996**, *118*, 8192-8197.
- (25) Canfield, J. M.; Warncke, K. *J. Phys. Chem. B* **2002**, *106*, 8831-8841.

- (26) Wang, M.; Warncke, K. *Journal of the American Chemical Society* **2008**, *130*, 4846-4858.
- (27) Puckett, J. M.; Mitchell, M. B.; Hirota, S.; Marzilli, L. G. *Inorganic Chemistry* **1996**, *35*, 4656-4662.
- (28) Dong, S. L.; Padmakumar, R.; Banerjee, R.; Spiro, T. G. *Journal of the American Chemical Society* **1996**, *118*, 9182-9183.
- (29) Stich, T. A.; Brooks, A. J.; Buan, N. R.; Brunold, T. C. *Journal of the American Chemical Society* **2003**, *125*, 5897-5914.
- (30) Yamanishi, M.; Yunoki, M.; Tobimatsu, T.; Sato, H.; Matsui, J.; Dokiya, A.; Iuchi, Y.; Oe, K.; Suto, K.; Shibata, N.; Morimoto, Y.; Yasuoka, N.; Toraya, T. *European Journal of Biochemistry* **2002**, *269*, 4484-4494.
- (31) Gerards, L. E. H.; Bulthuis, H.; Debolster, M. W. G.; Balt, S. *Inorganica Chimica Acta* **1991**, *190*, 47-53.
- (32) Sension, R. J.; Harris, D. A.; Stickrath, A.; Cole, A. G.; Fox, C. C.; Marsh, E. N. G. *Journal of Physical Chemistry B* **2005**, *109*, 18146-18152.
- (33) Schwartz, P. A.; Frey, P. A. *Biochemistry* **2007**, *46*, 7284-7292.
- (34) Barker, H. A.; Iodice, A. A.; Rooze, V.; Suzuki, F. *Journal of Biological Chemistry* **1964**, *239*, 3260-&.
- (35) Moore, B. S.; Eisenberg, R.; Weber, C.; Bridges, A.; Nanz, D.; Robinson, J. A. *Journal of the American Chemical Society* **1995**, *117*, 11285-11291.
- (36) Pierik, A. J.; Ciceri, D.; Broker, G.; Edwards, C. H.; McFarlane, W.; Winter, J.; Buckel, W.; Golding, B. T. *Journal of the American Chemical Society* **2002**, *124*, 14039-14048.
- (37) Marsh, E. N.; Harding, S. E. *Biochemical Journal* **1993**, *290*, 551-555.
- (38) Chirpich, T. P.; Zappia, V.; Costilow, R. N.; Barker, H. A. *Journal of Biological Chemistry* **1970**, *245*, 1778-&.
- (39) Wolthers, K. R.; Rigby, S. E. J.; Scrutton, N. S. *Journal of Biological Chemistry* **2008**, *283*, 34615-34625.
- (40) Babior, B. M. In *B12*; Dolphin, D., Ed.; Wiley: New York, 1982; Vol. 2, p 263-387.
- (41) Klotow, T.; Wiater, A. *Archives of Biochemistry and Biophysics* **1965**, *112*, 562-&.
- (42) Manitto, P.; Speranza, G.; Fontana, G.; Galli, A. *Helvetica Chimica Acta* **1998**, *81*, 2005-2016.
- (43) Ghambeer, R. K. *Indian Journal of Biochemistry* **1967**, *4*, 36-&.
- (44) Bandarian, V.; Reed, G. H. In *Chemistry and Biochemistry of B12*; Banerjee, R., Ed.; John Wiley and Sons: New York, 1999, p 811-833.
- (45) Bradbeer, C. *Journal of Biological Chemistry* **1965**, *240*, 4669-&.
- (46) Blackwell, C. M.; Turner, J. M. *Biochemical Journal* **1978**, *175*, 555-563.
- (47) Carty, T. J.; Babior, B. M.; Abeles, R. H. *Journal of Biological Chemistry* **1974**, *249*, 1683-1688.
- (48) Graves, S. W.; Krouwer, J. S.; Babior, B. M. *Journal of Biological Chemistry* **1980**, *255*, 7444-7448.
- (49) Poyner, R. R.; Anderson, M. A.; Bandarian, V.; Cleland, W. W.; Reed, G. H. *Journal of the American Chemical Society* **2006**, *128*, 7120-7121.

- (50) Sun, L.; Groover, O. A.; Canfield, J. M.; Warncke, K. *Biochemistry* **2008**, *47*, 5523-5535.
- (51) Babior, B. M.; Moss, T. H.; Orme-Johnson, W. H.; Beinert, H. *Journal of Biological Chemistry* **1974**, *249*, 4537-4544.
- (52) Carty, T. J.; Babior, B. M.; Abeles, R. H. *J. Biol. Chem.* **1971**, *246*, 6313-6317.
- (53) Graves, S. W.; Fox, J. A.; Babior, B. M. *Biochemistry* **1980**, *19*, 3630-3633.
- (54) Shibata, N.; Masuda, J.; Tobimatsu, T.; Toraya, T.; Suto, K.; Morimoto, Y.; Yasuoka, N. *Structure* **1999**, *7*, 997-1008.
- (55) Faust, L. P.; Babior, B. M. *Archives of Biochemistry and Biophysics* **1992**, *294*, 50-54.
- (56) Faust, L. R. P.; Connor, J. A.; Roof, D. M.; Hoch, J. A.; Babior, B. M. *Journal of Biological Chemistry* **1990**, *265*, 12462-12466.
- (57) Mancina, F.; Evans, P. R. *Structure with Folding & Design* **1998**, *6*, 711-720.
- (58) Reitzer, R.; Gruber, K.; Jogl, G.; Wagner, U. G.; Bothe, H.; Buckel, W.; Kratky, C. *Structure* **1999**, *7*, 891-902.
- (59) Canfield, J. M.; Warncke, K. *Journal of Physical Chemistry B* **2005**, *109*, 3053-3064.
- (60) Sun, L.; Warncke, K. *Proteins: Structure, Function, and Bioinformatics* **2006**, *64*, 308-319.
- (61) Joint-Center-for-Structural-Genomics [10.2210/pdb2qez/pdb](https://doi.org/10.2210/pdb2qez/pdb) **2007**.
- (62) Atherton, N. M. *Principles of Electron Spin Resonance*; Ellis Horwood Limited: New York, 1993.
- (63) Bender, C. J.; Berliner, L. J. *Computational and instrumental methods in EPR* New York, NY : Springer, 2006.
- (64) Scott, R. A. *Applications of physical methods to inorganic and bioinorganic chemistry*; Hoboken, NJ : Wiley, 2007.
- (65) Jensen, K. P. *Journal of Physical Chemistry B* **2005**, *109*, 10505-10512.
- (66) Stich, T. A.; Buan, N. R.; Brunold, T. C. *Journal of the American Chemical Society* **2004**, *126*, 9735-9749.
- (67) Stich, T. A.; Yamanishi, M.; Banerjee, R.; Brunold, T. C. *Journal of the American Chemical Society* **2005**, *127*, 7660-7661.
- (68) Legrini, O.; Oliveros, E.; Braun, A. M. *Chemical Reviews* **1993**, *93*, 671-698.
- (69) Lamola, A. A.; Hammond, G. S. *Journal of Chemical Physics* **1965**, *43*, 2129-&.
- (70) Wasielewski, M. R. *Chemical Reviews* **1992**, *92*, 435-461.
- (71) Rettig, W. *Angewandte Chemie-International Edition in English* **1986**, *25*, 971-988.
- (72) Brady, R. O.; Barker, H. A. *Biochemical and Biophysical Research Communications* **1961**, *4*, 373-&.
- (73) Rao, D. N. R.; Symons, M. C. R. *Journal of the Chemical Society-Perkin Transactions 2* **1983**, 187-190.
- (74) Gibson, Q. H. *Journal of Physiology-London* **1956**, *134*, 112-122.

- (75) Austin, R. H.; Beeson, K. W.; Eisenstein, L.; Frauenfelder, H.; Gunsalus, I. *C. Biochemistry* **1975**, *14*, 5355-5373.
- (76) Frauenfelder, H.; Fenimore, P. W.; McMahon, B. H. *Biophysical Chemistry* **2002**, *98*, 35-48.
- (77) Fenimore, P. W.; Frauenfelder, H.; McMahon, B. H.; Parak, F. G. *Proceedings of the National Academy of Sciences of the United States of America* **2002**, *99*, 16047-16051.
- (78) Frauenfelder, H.; Parak, F.; Young, R. D. *Annual Review of Biophysics and Biophysical Chemistry* **1988**, *17*, 451-479.
- (79) Tetreau, C.; Tourbez, M.; Gorren, A.; Mayer, B.; Lavalette, D. *Biochemistry* **1999**, *38*, 7210-7218.
- (80) Ehrenstein, D.; Nienhaus, G. U. *Proceedings of the National Academy of Sciences of the United States of America* **1992**, *89*, 9681-9685.
- (81) Symons, M. C. R.; Petersen, R. L. *Proceedings of the Royal Society of London Series B-Biological Sciences* **1978**, *201*, 285-300.
- (82) Gasyňa, Z. *Febs Letters* **1979**, *106*, 213-218.
- (83) Davydov, R.; Kuprin, S.; Graslund, A.; Ehrenberg, A. *Journal of the American Chemical Society* **1994**, *116*, 11120-11128.
- (84) Blumenfeld, L.; Davydov, R. M.; Fel, N. S.; Magonov, S. N.; Vilu, R. O. *Febs Letters* **1974**, *45*, 256-258.
- (85) Ericson, A.; Hedman, B.; Hodgson, K. O.; Green, J.; Dalton, H.; Bentsen, J. G.; Beer, R. H.; Lippard, S. J. *Journal of the American Chemical Society* **1988**, *110*, 2330-2332.
- (86) Chance, B. *Review of Scientific Instruments* **1951**, *22*, 619-627.
- (87) Gomezzens, A.; Perezbendito, D. *Analytica Chimica Acta* **1991**, *242*, 147-177.
- (88) Barman, T. E.; Travers, F. *Methods of Biochemical Analysis* **1985**, *31*, 1-59.
- (89) Thrall, S. H.; Krebs, R.; Wohrl, B. M.; Cellai, L.; Goody, R. S.; Restle, T. *Biochemistry* **1998**, *37*, 13349-13358.
- (90) Porter, G. *Proceedings of the Royal Society of London Series a-Mathematical and Physical Sciences* **1950**, *200*, 284-&.
- (91) Das, R.; Venkataraman, B. *Research on Chemical Intermediates* **2005**, *31*, 167-192.
- (92) Closs, G. L.; Miller, R. J. *Journal of the American Chemical Society* **1979**, *101*, 1639-1641.
- (93) Jacob, M.; Holtermann, G.; Perl, D.; Reinstein, J.; Schindler, T.; Geeves, M. A.; Schmid, F. X. *Biochemistry* **1999**, *38*, 2882-2891.
- (94) Quick, C. R.; Wittig, C. *Chemical Physics Letters* **1977**, *48*, 420-424.
- (95) Atkins, P. W.; McLauchlan, K.; Simpson, A. F. *Nature* **1968**, *219*, 927-&.
- (96) Wilson, A. D.; Friedmann, H.; Ahiman, V. *Chemical Physics Letters* **1976**, *43*, 539-543.
- (97) Fink, A. L. *Accounts of Chemical Research* **1977**, *10*, 233-239.
- (98) Travers, F.; Barman, T. *Biochimie* **1995**, *77*, 937-948.
- (99) Moore, J. W.; Pearson, R. G. *Kinetics and Mechanism*; Wiley and Sons: New York, 1981.

- (100) Douzou, P.; Sireix, R.; Travers, F. *Proc. Natl. Acad. Sci.* **1970**, *66*, 787-792.
- (101) Mustafi, D.; Hofer, J. E.; Huang, W.; Palzkill, T.; Makinen, M. W. *Spectrochimica Acta A* **2004**, *60*, 1279-1289.
- (102) Travers, F.; Bertrand, R.; Roseau, G.; Vanthoai, N. *Eur. J. Biochem.* **1978**, *88*, 523-528.
- (103) Feig, A. L.; Ammons, G. E.; Uhlenbeck, O. C. *RNA* **1998**, *4*, 1251-1258.
- (104) Douzou, P. *Cryobiochemistry: An Introduction*; Academic Press: New York, 1977.
- (105) Tesi, C.; Travers, F.; Barman, T. *Biochemistry* **1990**, *29*, 1846-1852.
- (106) Bicknell, R.; Waley, S. G. *Biochemistry* **1985**, *24*, 6876-6887.
- (107) Bragger, J. M.; Dunn, R. V.; Daniel, R. M. *Biochimica Et Biophysica Acta-Protein Structure and Molecular Enzymology* **2000**, *1480*, 278-282.
- (108) Babior, B. M. *J. Biol. Chem.* **1970**, *245*, 1755-1766.
- (109) Babior, B. M.; Krouwer, J. S. *CRC Critical Reviews in Biochemistry* **1979**, *6*, 35-102.
- (110) Baudot, A.; Alger, L.; Boutron, P. *Cryobiology* **2000**, *40*, 151-158.
- (111) Fahy, G. M.; Lilley, T. H.; Linsdell, H.; Douglas, M. S.; Meryman, H. T. *Cryobiology* **1990**, *27*, 247-268.
- (112) Mehl, P. M. *Cryobiology* **1993**, *30*, 509-518.
- (113) Corporation, G. C. *Dimethyl Sulfoxide (DMSO) Physical Properties*, 2005.
- (114) Schichma, Sa; Amey, R. L. *Journal of Physical Chemistry* **1971**, *75*, 98-&.
- (115) Travers, F.; Douzou, P.; Pederson, T.; Gunsalus, I. C. *Biochimie* **1975**, *57*, 43-48.
- (116) Maurel, P.; Huibonhoa, G.; Douzou, P. *Journal of Biological Chemistry* **1975**, *250*, 1376-1382.
- (117) Shedlovsky, T.; Kay, R. L. *Journal of Physical Chemistry* **1956**, *60*, 151-155.
- (118) Sabatinni, D. D.; Barnett, R. J.; Bensch, K. G. *Anatomical Record* **1962**, *142*, 274.
- (119) Eaton, S. S.; More, K. M.; Sawant, B. M.; Boymel, P. M.; Eaton, G. R. **1983**, *52*, 435-449.
- (120) Carr, S. G.; Smith, T. D.; Pilbrow, J. R. *J. Chem. Soc. Faraday Trans. 2* **1974**, 497-511.
- (121) Bandarian, V.; Reed, G. H. *Biochemistry* **2002**, *41*, 8580-8588.
- (122) Lukoyanov, D.; Barney, B. M.; Dean, D. R.; Seefeldt, L. C.; Hoffman, B. M. *Proc. Natl. Acad. Sci.* **2007**, *104*, 1451-1455.
- (123) Wallis, O. C.; Bray, R. C.; Gutteridge, S.; Hollaway, M. R. *Eur. J. Biochem.* **1982**, *125*, 299-303.
- (124) Hay, B. P.; Finke, R. G. *J. Am. Chem. Soc.* **1986**, *108*, 4820-4829.
- (125) McMillen, D. F.; Golden, D. M. *Ann. Rev. Phys. Chem.* **1982**, *33*, 493-532.
- (126) Berkowitz, J.; Ellison, G. B.; Gutman, D. *J. Phys. Chem.* **1994**, *98*, 2744-2765.
- (127) Wetmore, S. D.; Smith, D. M.; Bennett, J. T.; Radom, L. *J. Am. Chem. Soc.* **2002**, *124*, 14054-14065.

- (128) Sandala, G. M.; Smith, D. M.; Radom, L. *J. Am. Chem. Soc.* **2005**, *127*, 8856-8864.
- (129) Semialjac, M.; Schwarz, H. *Chem. Eur. J.* **2004**, *10*, 2781-2788.
- (130) Halpern, J.; Kim, S.-H.; Leung, T. W. *J. Am. Chem. Soc.* **1984**, *106*, 8317-8319.
- (131) Finke, R. G.; Hay, B. P. *Inorganic Chemistry* **1984**, *23*, 3041-3043.
- (132) Warncke, K.; Utada, A. S. *J. Am. Chem. Soc.* **2001**, *123*, 8564-8572.
- (133) Weisblat, D. A.; Babior, B. M. *Journal of Biological Chemistry* **1971**, *246*, 6064-&.
- (134) Kohen, A.; Klinman, J. P. *Accounts of Chemical Research* **1998**, *31*, 397-404.
- (135) Kohen, A.; Klinman, J. P. *Chemistry & Biology* **1999**, *6*, R191-R198.
- (136) Moiseyev, N.; Rucker, J.; Glickman, M. H. *Journal of the American Chemical Society* **1997**, *119*, 3853-3860.
- (137) Kiefer, P. M.; Hynes, J. T. *Journal of Physical Chemistry A* **2003**, *107*, 9022-9039.
- (138) Leo, A.; Hansch, C.; Elkins, D. *Chemical Reviews* **1971**, *71*, 525-+.
- (139) Jaros, F.; Straka, T.; Dobesova, Z.; Pintrova, M.; Chalupsky, K.; Kunes, J.; Entlicher, G.; Zicha, J. *European Journal of Pharmacology* **2007**, *575*, 122-126.
- (140) Sharma, P. K.; Chu, Z. T.; Olsson, M. H. M.; Warshel, A. *Proceedings of the National Academy of Sciences of the United States of America* **2007**, *104*, 9661-9666.
- (141) Chothia, C.; Janin, J. *Nature* **1975**, *256*, 705-708.
- (142) Rand, R. P.; Fuller, N. L.; Butko, P.; Francis, G.; Nicholls, P. *Biochemistry* **1993**, *32*, 5925-5929.
- (143) Quiel, F. *Photogrammetric Engineering and Remote Sensing* **1975**, *41*, 341-346.
- (144) Brigaud, F.; Vasseur, G. *Geophysical Journal International* **1989**, *98*, 525-542.
- (145) Varshni, Y. P. *Physica* **1967**, *34*, 149-&.
- (146) Li, S.; Zhang, K.; Yang, J. M.; Lin, L. W.; Yang, H. *Nano Letters* **2007**, *7*, 3102-3105.
- (147) Joshi, A.; Narsingi, K. Y.; Manasreh, M. O.; Davis, E. A.; Weaver, B. D. *Applied Physics Letters* **2006**, *89*, 3.
- (148) Peng, X. G.; Manna, L.; Yang, W. D.; Wickham, J.; Scher, E.; Kadavanich, A.; Alivisatos, A. P. *Nature* **2000**, *404*, 59-61.
- (149) Donega, C. D.; Bode, M.; Meijerink, A. *Physical Review B* **2006**, *74*, 9.
- (150) Martin, B. D.; Finke, R. G. *Journal of the American Chemical Society* **1990**, *112*, 2419-2420.
- (151) Martin, B. D.; Finke, R. G. *Journal of the American Chemical Society* **1992**, *114*, 585-592.
- (152) Hung, R. R.; Grabowski, J. J. *Journal of the American Chemical Society* **1999**, *121*, 1359-1364.
- (153) Luo, L. B.; Li, G.; Chen, H. L.; Fu, S. W.; Zhang, S. Y. *Journal of the Chemical Society-Dalton Transactions* **1998**, 2103-2107.
- (154) Halpern, J. *Science* **1985**, *227*, 869-875.

- (155) Hill, H. A. O.; Pratt, J. M.; Williams, R. J. P. *Chemistry in Britain* **1969**, *5*, 156-+.
- (156) Mayer, I. *Chemical Physics Letters* **1983**, *97*, 270-274.
- (157) Mayer, I. *International Journal of Quantum Chemistry* **1984**, *26*, 151-154.
- (158) Mayer, I. *Theoretica Chimica Acta* **1985**, *67*, 315-322.
- (159) Brooks, A. J.; Vlasie, M.; Banerjee, R.; Brunold, T. C. *Journal of the American Chemical Society* **2004**, *126*, 8167-8180.
- (160) Mancina, F.; Keep, N. H.; Nakagawa, A.; Leadlay, P. F.; McSweeney, S.; Rasmussen, B.; Bosecke, P.; Diat, O.; Evans, P. R. *Structure* **1996**, *4*, 339-350.
- (161) Dong, S. L.; Padmakumar, R.; Banerjee, R.; Spiro, T. G. *Inorganica Chimica Acta* **1998**, *270*, 392-398.
- (162) Dong, S. L.; Padmakumar, R.; Banerjee, R.; Spiro, T. G. *Journal of the American Chemical Society* **1999**, *121*, 7063-7070.
- (163) Chagovetz, A. M.; Grissom, C. B. *Journal of the American Chemical Society* **1993**, *115*, 12152-12157.
- (164) Lott, W. B.; Chagovetz, A. M.; Grissom, C. B. *Journal of the American Chemical Society* **1995**, *117*, 12194-12201.
- (165) Kruppa, A. I.; Taraban, M. B.; Leshina, T. V.; Natarajan, E.; Grissom, C. B. *Inorganic Chemistry* **1997**, *36*, 758-&.
- (166) Ghanekar, V. D.; Coffman, R. E. *Journal of Organometallic Chemistry* **1980**, *198*, C15-C19.
- (167) Lowe, D. J.; Joblin, K. N.; Cardin, D. J. *Biochimica Et Biophysica Acta* **1978**, *539*, 398-401.
- (168) Endicott, J. F.; Netzel, T. L. *Journal of the American Chemical Society* **1979**, *101*, 4000-4002.
- (169) Chen, E.; Chance, M. R. *Biochemistry* **1993**, *32*, 1480-1487.
- (170) Chen, E. F.; Chance, M. R. *Abstracts of Papers of the American Chemical Society* **1990**, *200*, 196-INOR.
- (171) Sension, R. J.; Walker, L. A.; Shiang, J. J. *Abstracts of Papers of the American Chemical Society* **1998**, *216*, U684-U684.
- (172) Cole, A. G.; Anderson, N.; Shiang, J. J.; Sension, R. J. *Abstracts of Papers of the American Chemical Society* **2000**, *220*, U223-U223.
- (173) Yoder, L. M.; Cole, A. G.; Walker, L. A.; Sension, R. J. *Journal of Physical Chemistry B* **2001**, *105*, 12180-12188.
- (174) Sension, R. J.; Harris, D. A.; Cole, A. G. *Journal of Physical Chemistry B* **2005**, *109*, 21954-21962.
- (175) Muroski, A. R.; Booksh, K. S.; Myrick, M. L. *Analytical Chemistry* **1996**, *68*, 3534-3538.
- (176) Brown, K. L.; Zou, X. *Journal of Inorganic Biochemistry* **1999**, *77*, 185-195.
- (177) Magnusson, O. T.; Frey, P. A. *Journal of the American Chemical Society* **2000**, *122*, 8807-8813.
- (178) Buettner, G. R. *Free Radical Biology and Medicine* **1987**, *3*, 259-303.
- (179) Finkelstein, E.; Rosen, G. M.; Rauckman, E. J.; Paxton, J. *Molecular Pharmacology* **1979**, *16*, 676-685.

- (180) Rosen, G. M.; Pou, S.; Ramos, C. L.; Cohen, M. S.; Britigan, B. E. *Faseb Journal* **1995**, *9*, 200-209.
- (181) Thoma, N. H.; Evans, P. R.; Leadlay, P. F. *Biochemistry* **2000**, *39*, 9213-9221.